THE PRODUCTION OF PULSED NOZZLE FLOWS IN A SHOCK TUBE

by

Neil Robert Mudford

A thesis submitted for the
degree of Doctor of Philosophy
at the Australian National University
Canberra

September 1976

The contents of this thesis, except as described in the Acknowledgements and where credit is indicated by reference, is entirely my own work

N.R. Mudford.

(Neil Robert Mudford)

ACKNOWLEDGEMENTS.

Firstly, I would like to thank my supervisor, Dr. R. J. Stalker, for the invaluable help and guidance which he has given me during the time that we have worked together. I am also indebted to him for the design of the hardware for the modification to the shock tunnel and for the original concept for the modification. I would also like to thank Dr. Hans Hornung and Dr. John Sandeman for their generous assistance, given on innumerable occasions.

There are many other people to whom I am indebted: to Mr. Roland French, Mr. Vic Adams and Mr. Gavin Spackman for their help in performing the experiments, maintaining the equipment and running the tunnel and shock tube safely and efficiently; to Mr. Ken Smith for his photographic work and the helpful advice he has given in this field; to Mr. Len Batt and Mr. David King for repair and maintenance of the electronic equipment; to the workshop staff of the Physics Department for the production of several pieces of apparatus all of which have been of high quality.

My thanks go also to my fellow post-graduate students, notably Doug Kewley, Nizar Ebrahim, Graham Caldersmith, John Baird and Mike Daffey, for the many stimulating and helpful discussions we have had.

I extend my thanks to Ms. Julie Faux, not only for typing this thesis, but for going, with me, through all the traumas of its compilation.

Finally, I wish to express my appreciation to the Australian Government for their provision of a Commonwealth Scholarship and to the Australian Research Grants Committee for the funding of the research.

ABSTRACT

A theoretical and experimental study has been made of short duration nozzle flows in a high enthalpy non-reflected shock tunnel.

A reduction in initial nozzle density, necessary for minimisation of the loss of steady test flow time due to starting processes in the nozzle, was achieved by creating a steady supersonic flow in the nozzle prior to the arrival of the primary shock. A model of the nozzle starting processes in a non-reflected shock tunnel was developed from a model, due to Smith (1966), for these processes in a reflected shock tunnel. On the basis of this model a method of characteristics calculation and an analytic calculation were made. These calculations yielded predictions for the paths, in the x-t plane, of the principal disturbances due to the nozzle starting processes.

A contoured nozzle was designed to produce a uniform, parallel, steady test flow in the test section, with minimum test flow time losses.

An experimental programme was undertaken to observe both the shock tube and test section flows in the shock tunnel. This programme yielded information about the primary shock speed in the shock tube, the duration of test flow in the shock tube, the paths in the x-t plane of the unsteady flow features in the nozzle flow, the steadiness, integrated refractivity and duration of the steady test section flow and the species present as impurities in the flows.

The test gases used in the experiments were air, as a representative dissociating gas, and argon, as a representative ionising gas. Usable test flows of 10 μsec duration were produced with stagnation enthalpies of 60 MJ/kg in air and 35 MJ/kg in argon.

TABLE OF CONTENTS.

CHAPTER 1. INTRODUCTION.

Studies in high velocity, hypersonic gas dynamics, have, for many years, been carried out with the aid of the reflected shock tunnel (e.g. Hertzberg et al (1961) Holder and Schultz (1961)). The shock tube, from which the reflected shock tunnel is derived, is capable of producing hypersonic flows with higher stagnation enthalpies and higher densities than can be realised in the reflected shock tunnel. If hypersonic flows with higher stagnation enthalpies and densities could be produced, several important phenomena, such as the effects of chemical reactions, radiation or electron thermal conductivity on a flowfield, could be studied more fully.

In the reflected shock tunnel, the primary shock in the shock tube is reflected at the end of the tube. The resulting high pressure reservoir of gas then passes into the hypersonic nozzle through a small hole in the end wall. The limitations of the reflected shock tunnel arise almost entirely from the process of shock reflection.

By developing a non-reflected shock tunnel as a derivative of the shock tube, the limitations associated with shock reflection can be circumvented (Oertel (1969)). The primary shock in the non-reflected shock tunnel passes directly from the shock tube into the hypersonic nozzle. Part of the flow which follows the shock is expanded through the nozzle in a steady expansion to produce a steady, hypersonic flow in the test section.

The non-reflected mode of operation has three advantages over the reflected mode:

1. High densities. High test section densities are produced by high nozzle reservoir pressures. Because of the fact that the non-reflected tunnel avoids the entropy rise across a reflected shock, the nozzle reservoir pressure should be higher for the non-reflected tunnel than for the reflected tunnel. A comparison of this pressure for the reflected (P_{RR}) and non-reflected (P_{RM}) tunnels is shown in Fig. 1.1 as a function of nozzle flow stagnation enthalpy for an initial shock tube pressure of 10 torr. It will be noted that the ratio (P_{RM}/P_{RR}) is always greater than 1 and increases with stagnation enthalpy. This graph was drawn from curves given by Lewis and Burgess (1964).

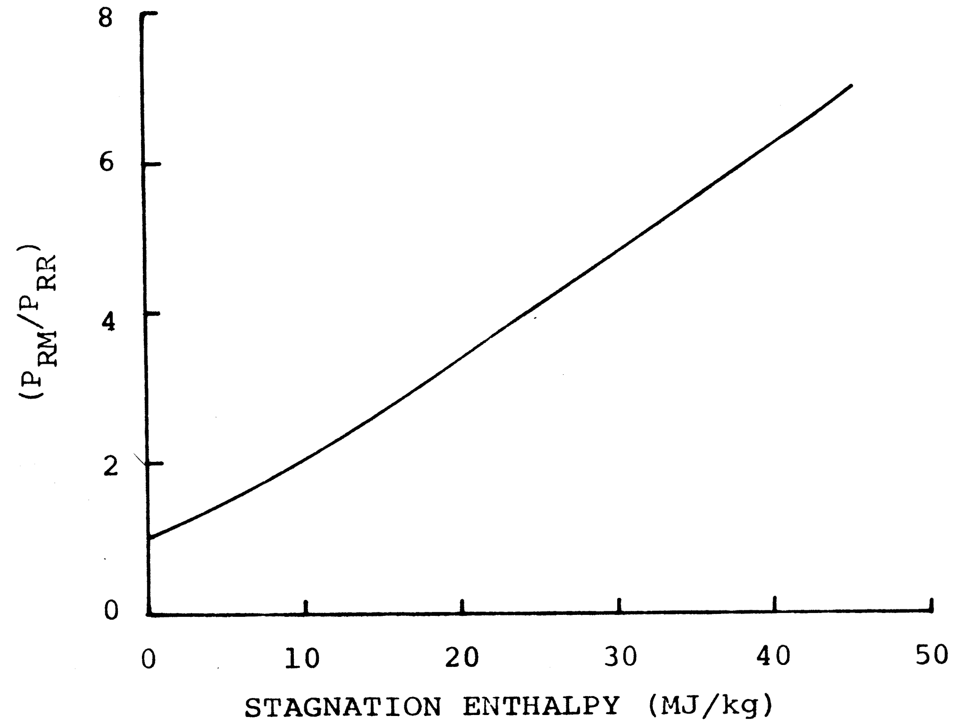

Fig. 1.1. The ratio of the nozzle reservoir pressure for the non-reflected (P_{RM}) and reflected (P_{RR}) shock tunnel as a function of stagnation enthalpy.

It was assumed in the calculations which produced the graph in Fig. 1.1 that the nozzle pressure in the reflected tunnel was the reflected shock pressure i.e. that the tunnel was run at the tailored interface condition. However, for high enthalpy operation, the reflected tunnel must be run below the tailored interface condition to avoid contamination of the test gas by the driver gas. This implies that the nozzle reservoir pressure is less than P_{RR} in the reflected mode.

Stalker and Hornung (1969) have reported that the plateau pressure, measured in the stagnation region of a high enthalpy reflected shock tunnel, was substantially below the calculated value.

In practice, therefore, the ratio of the nozzle pressure in the non-reflected mode to that in the reflected mode will be higher than that shown in Fig. 1.1.

A high test section density leads to a reduction in the relaxation length for chemical reactions. A number of studies of flows in which non-equilibrium chemistry in a body flow causes significant changes in the flow density, over the dimensions of the body, have been carried out at the A.N.U. (Hornung and Sandeman (1974), Kewley and Hornung (1974), Ebrahim and Hornung (1975)). A reduction in the chemical relaxation length will allow the performance of a wider range of experiments of this type. As well as this, the higher densities in the non-reflected tunnel will aid the production of flows with high Reynolds Number.

2. High stagnation enthalpies. Studies by Logan (1972) have shown that substantial enthalpy losses occur, through radiation in the stagnation region, in the reflected tunnel at high stagnation enthalpies. For example, Logan showed that for a 5.7km/sec. primary shock into 2"Hg of argon, losses of up to 65% of the enthalpy occur in the stagnation region of a reflected tunnel. This loss is in addition to radiative energy losses from the gas behind the primary shock. Hornung and Sandeman (1974) confirmed Logan's results and concluded that the test section flow speed appeared to be limited by the losses to 6km/sec. in argon in a reflected tunnel.

Between 40 and 45% of the stagnation enthalpy of the gas behind the primary shock in the tube is in the form of kinetic energy. This sets an upper limit for the radiative energy losses from flows in a non-reflected shock tunnel. The elimination of the shock reflection process in the shock tunnel therefore leads to a retention of a far greater proportion of the stagnation enthalpy of the test gas. The only losses through radiation are those occuring behind the primary shock.

3. Test gas purity. The interaction of a reflected shock wave and the boundary layer on the shock tube walls leads to mixing of the boundary layer gas with the test gas. Impurities from the shock tube walls are thereby introduced into the test flow. By contrast, the flow in the test section of the non-reflected shock tunnel should be spectroscopically pure if the flow behind the primary shock in the tube is spectroscopically pure.

Another source of contamination of the test gas flow in a reflected shock tunnel is the flow of He driver gas along the shock tube walls after shock reflection. Davies and Wilson (1969) proposed this mechanism to explain the fact that He appeared in the test section flow a good deal earlier than would occur had the contact surface been leak-free. Shock tube studies at the A.N.U. have shown that if the contact surface is stable there is only a small amount of mixing of the test and driver gases across the contact surface in the tube. It is therefore reasonable to expect that there will be little He contamination in the test section flows in the non-reflected shock tunnel.

The only disadvantage of the non-reflected shock tunnel is the short duration of steady flow in the test section. An upper limit for the steady test section flow time is imposed by the flow time in the shock tube which, for the shock conditions presented in this thesis, can be as low as 20 μsec. In fact the steady test section flow time is reduced below the tube flow time by nonsteady starting and finishing processes occuring in the nozzle flow. To minimise test time losses due to nonsteady starting processes in a non-reflected shock tunnel, Oertel (1969) placed a thin diaphragm at the end of the shock tube and evacuated the nozzle and test section. The shock tube flows in the facility at the A.N.U. are of higher stagnation enthalpy and shorter duration than those of Oertel. The short test times are not sufficient to allow successful removal of such a diaphragm.

Studies on a small, non-reflected shock tunnel (Stalker and Mudford (1973)) showed that the establishment of a steady, supersonic flow in the nozzle test section, prior to the arrival of the primary shock, increased the test flow time in the tunnel.This flow, which will be referred to throughout this thesis as the Prior Steady Flow, is established by opening a valve between the test section, in which the initial gas conditions are those of the shock tube, and an evacuated dump tank downstream of the test section. In this thesis the technique is applied to flows in a large shock tunnel (see Stalker and Hornung (1969) for details of the shock tube from which the tunnel is derived). It will be shown in the thesis that the reduction in density in the nozzle, due to the presence of the prior steady flow, is sufficient to ensure that the test time losses, due to the nonsteady starting processes, are minimized.

In Chapter 2, the nonsteady starting and finishing processes in the nozzle flow will be discussed. An analytic model which may be used to calculate the trajectories of the features of interest in the nonsteady flow will be presented in this chapter.

The method used to design a nozzle which must be short, in order to ensure rapid starting of the nozzle flow, and yet produce a steady, uniform, hypersonic test section flow, is presented in Chapter 3.

In Chapter 4, the details of the experiments performed to observe the flows in the non-reflected shock tunnel are given.

The results of the experiments and discussion of the results are contained in Chapter 5.

Finally, in Chapter 6, the conclusion and summary of the thesis are presented.

CHAPTER 2. STARTING PROCESSES IN THE NOZZLE.

2.1. INTRODUCTION.

A one dimensional shock wave propogating along a shock tube will travel at constant speed if the cross-sectional area of the tube, the density (and pressure and composition) of the gas ahead of shock and the pressure of the driver gas at the contact surface all remain constant. The gain in momentum experienced by the initially quiescent test gas, as it passes through the shock wave, is balanced by the impulse of the driver gas at the contact surface. Under these circumstances, in the rest frame of the shock, there are no travelling pressure disturbances in the post shock gas.

However, if the shock wave passes into an expanding portion of the shock tube, such as a hypersonic nozzle, and the initial test gas density in the nozzle is the same as that in the upstream parts of the tube, then the shock will decelerate and a compressive pressure disturbance will propagate upstream relative to the primary shock. The reason for the deceleration of the primary shock is that an increase in the tube cross-sectional area leads to an increase in the test gas mass to be accelerated per unit distance travelled by the shock. As well as this, the post primary shock pressure impulse is reduced by the area increase, because the post shock flow is supersonic for the shocks of interest.

If, on the other hand, the density ahead of the primary shock is reduced, while the cross-sectional area remains constant, the primary shock will accelerate and an upstream facing expansion wave will propagate into the post primary shock gas.

The shock acceleration is due to the decrease in the mass to be accelerated by the shock per unit distance travelled by the shock coupled with the constancy of the post primary shock gas pressure upstream of the head of the expansion wave.

The above phenomena are relevant to the problem of loss of steady nozzle flow time due to nonsteady flow processes occuring at the beginning of the test gas flow. As pointed out in the introduction, it is important that steps be taken to minimise such test time losses because of the short test flow times available in the shock tube at high stagnation enthalpies.

C.E. Smith (I966) has made a study of the nonsteady processes which precede the establishment of a steady, or a near steady, flow in the nozzle of a shock tunnel operated in the reflected mode. By placing a diaphragm at the nozzle entrance, Smith was able to set the initial density in the nozzle to any desired value. He showed that, up to a point, the time for the nozzle flow to become steady, at a particular station, is reduced by a reduction in the initial pressure (density) in the nozzle.

It is not possible to place a diaphragm at the nozzle entrance of the non-reflected shock tunnel because the test flow is not of sufficient duration to successsfully rupture a diaphragm and remove the diaphragm material from the flow. (see Chapter 5, section 5.2 for the test flow durations). However, it will be shown in this thesis, that the loss of steady test flow time, due to the nonsteady starting processes, can be minimised by the establishment of a steady, supersonic flow in the nozzle prior to the arrival of the primary shock. I shall refer to this pre-primary shock flow as the "prior steady flow".

The establishment of the prior steady flow is initiated by opening a valve between the downstream end of the test section and the evacuated dump tank further downstream (see Chapter 4, section 4.I). Gas in the test section flows into the dump tank and an expansion wave travels upstream into the test section and the nozzle. After a time the flow becomes steady and is supersonic downstream of the nozzle entrance, where the flow is sonic.

The valve is opened by the recoil of the shock tube mechanism which occurs when the free piston moves forward off its launcher and begins to move down the compression tube. In Appendix A it is shown that there is sufficient time, between the valve opening and the arrival of the primary shock at the nozzle, for the prior flow to become steady. It is also shown, in the same appendix, that the shock tube pressure is not significantly reduced by the existence of the prior steady flow.

The frame of reference from which the system is viewed changes a number of times throughout this discussion. In order to avoid the confusion that would arise from the use of the conventional definitions of "upstream" and "downstream", the following definitions are adopted.

"Upstream" will mean the direction from the dump tank to the free piston and "downstream" will mean the opposite direction in all frames of reference.

2.2. THE MODEL.

The model of the nonsteady starting flow field proposed by Smith, and supported by his experiments, needs only slight modification to be made applicable to the nozzle flow in the non-reflected shock tunnel. There are three important differences between the operation of the reflected and non reflected shock tunnels, with regard to the nozzle flows. In the reflected mode the final steady flow at the nozzle entrance is sonic; there is, initially, a diaphragm at the nozzle entrance and the test gas flow does not encounter the reduced initial density field in the nozzle until downstream of the nozzle entrance. In the non reflected mode the final, steady flow at the nozzle entrance is supersonic; there is no diaphragm at the nozzle entrance and the drop in initial gas density, due to the prior steady flow, begins upstream of the nozzle entrance.

The modified form of Smith's model is as follows (see Fig. 2.I). Consider, first, the case where a prior steady flow does exist in the nozzle. The primary shock travels at constant speed in the tube until it encounters the subsonic portion of the prior steady flow, upstream of the nozzle entrance. The reduced density in this region causes the primary shock to accelerate and causes a nonsteady expansion wave to propagate back into the post primary shock gas. The head of this expansion wave travels upstream in the frame of reference of the primary shock, but travels downstream in the laboratory frame, because the post primary shock flow is supersonic in the laboratory frame. The primary shock continues to accelerate until it reaches a point, a short distance downstream of the nozzle entrance, where the influence of the growing nozzle cross-sectional area exceeds the influence of the decreasing density field. The primary shock then begins to decelerate and a compression wave is sent back into the post primary shock gas. The continuing deceleration of the primary shock, after this point, causes the compression wave to steepen, and, eventually, it forms into an upstream facing shock wave.

The minimum test time lost due to the starting processes will occur when the secondary shock is so weak that it does not move upstream of the head of the nonsteady expan-

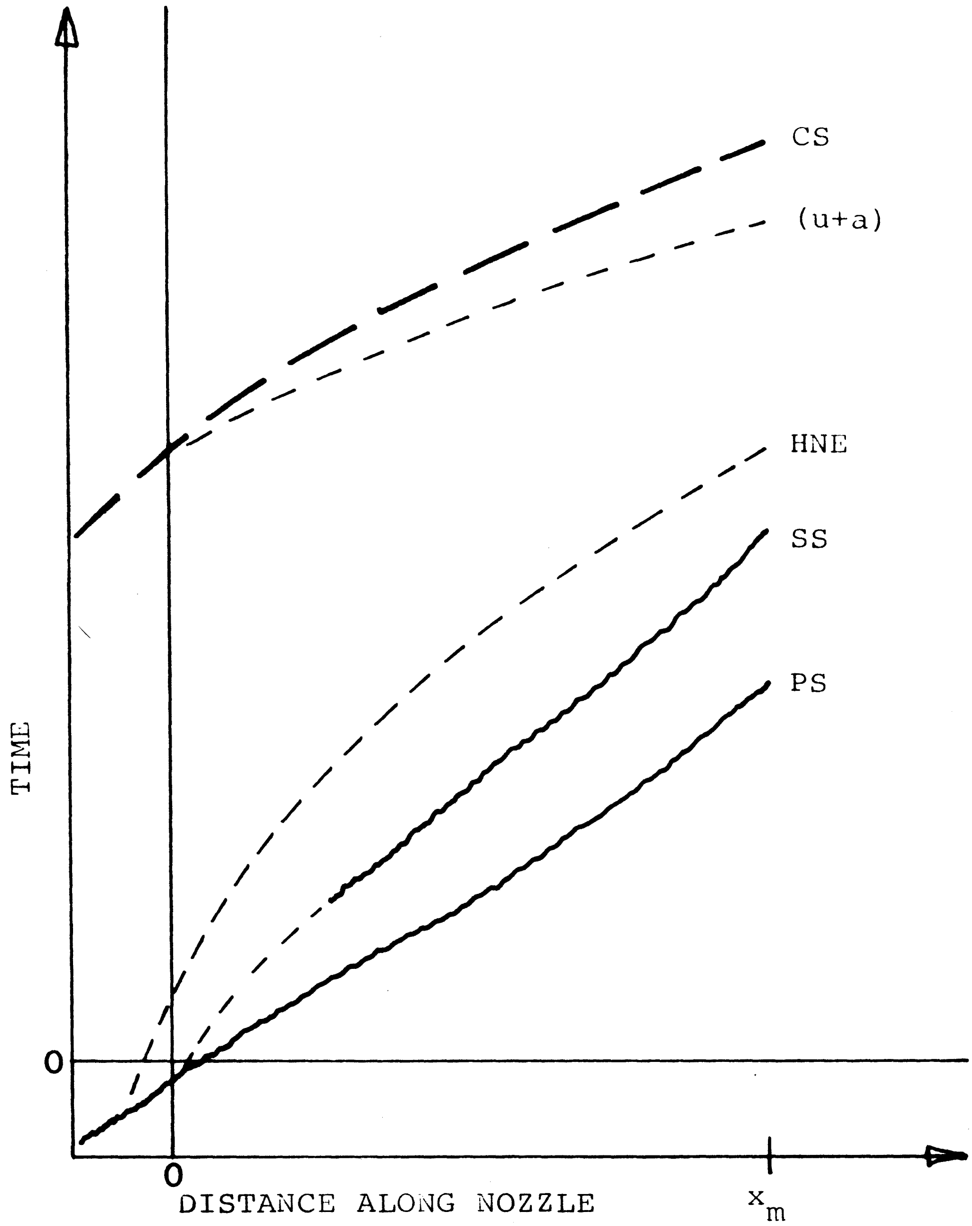

Fig. 2.1. Important nonsteady flow features in the nozzle flow (shown for a flow with a prior steady flow).

PS - primary shock, SS - secondary shock

HNE - head of the nonsteady expansion

(u+a) - disturbance from contact surface entry

CS - contact surface.

x_m - model station; steady test flow at this station exists between arrival of HNE and (u+a) waves.

sion wave. The head of the expansion wave is, in these circumstances, the upstream limit of the nonsteady flow field. After it has passed downstream of a particular station, steady test flow conditions will exist at that station.

If there is no prior flow in the nozzle, then the primary shock maintains its initial, constant speed until it encounters the expanding section of the nozzle and begins to decelerate. Once again, a secondary shock wave forms in the manner described above. In this case, due to the absence of the upstream facing expansion wave, the secondary shock is the upstream limit of the nonsteady starting flow field.

2.3. THE FLOW FIELD CALCULATIONS.

Calculations have been made of the trajectories of the starting shocks and the other flow features present in the nonsteady starting flowfield. From the results of these calculations, the effect of the presence of a prior steady flow in the nozzle can be assessed, and estimates made of the loss, if any, of the steady test flow time due to the presence of the secondary shock.

Two calculation methods were used to solve the problem of the nonsteady flowfield. The first method was a method of characteristics calculation, using perfect gas equations and a constant ratio of specific heats throughout. This calculation yielded estimates for the separation distance between the primary and secondary shocks in the nozzle and the variation of gas flow properties over the whole nonsteady flowfield. However, it could not, in its modelling of the flow, take account of the presence of real gas effects, such as chemical dissociation, ionisation and energy losses due to radiation.

The second method calculated, only, the trajectory of the centre of mass of the gas entrained between the primary and secondary shocks. It could not allow for gas property variations between the head of the nonsteady expansion and the secondary starting shock, or between the primary and secondary shocks. However, it did take some account of the presence of the real gas effects mentioned above. The system of the primary and secondary shocks will, from this point on, be referred to as the "shock system". The instantaneous centre of mass of the gas entrained between the two shocks

The characteristic relations given by Rudinger and specialised for a multi-isentropic flow (i.e. $DS/Dt = 0$, except when gas particle crosses a shock) with channel area varying with x but not t, no body forces and no mass removal through the walls are the following:

For the shock free flow regions:

The characteristic directions are given by

$$\frac{d\xi}{dt} = U + A \qquad \text{right-running bicharacteristic}$$

$$\frac{d\xi}{dt} = U - A \qquad \text{left-running bicharacteristic}$$

$$\frac{d\xi}{dt} = U \qquad \text{particle path}$$

Along a right running bicharacteristic the compatibility relation is:

$$\frac{\delta_+ P}{\delta t} = -AU\frac{\partial \ln A}{\partial \xi} + A\frac{\delta_+ S}{\delta t}$$

Along a left-running bicharacteristic the compatibility relation is

$$\frac{\delta_- Q}{\delta t} = -AU\frac{\partial \ln A}{\partial \xi} + A\frac{\delta_- S}{\delta t}$$

Along a particle path

$$\frac{DS}{Dt} = 0$$

where ξ = normalised distance = $\frac{x}{a_o\, t_o}$

t = normalised time = $\frac{t}{t_o}$

a_o, t_o = reference sound speed and reference time.

P and Q are the Riemann variables

$$P \equiv \frac{2}{(\gamma-1)} A + U$$

$$Q \equiv \frac{2}{(\gamma-1)} A - U$$

A = normalised sound speed = $\frac{a}{a_o}$

U = normalised flow speed = $\frac{u}{a_o}$

γ = ratio of specific heats

A = channel cross-sectional area

S = normalised entropy = $\frac{s}{\gamma R}$ (using rationalised units)

R = gas constant.

where the flow passes through a shock the shock jump relations must be employed. These were taken from Leipmann and Roshko (1957) and expressed in terms of the non-dimensional variables of Rudinger as:

$$S - S_\infty = \frac{1}{\gamma(\gamma-1)} \ln \left[\left(\frac{2\gamma}{(\gamma+1)} M_s^2 - \left(\frac{\gamma-1}{\gamma+1}\right) \right) \left(\frac{1 + \frac{\gamma-1}{2} M_s^2}{\frac{\gamma+1}{2} M_s^2} \right)^\gamma \right]$$

$$\frac{A}{A_\infty} = \left[1 + \frac{2(\gamma-1)}{(\gamma+1)^2} \frac{\gamma M_s^2 + 1}{M_s^2} (M_s^2 - 1) \right]^{\frac{1}{2}}$$

$$\frac{U_3 - U_s}{U_\infty - U_s} = \frac{(\gamma-1) M_s^2 + 2}{(\gamma+1) M_s^2}$$

where subscript ∞ = ahead of shock, 3 = behind shock, δ = shoc

The numerical approximations to the compatibility relations were the simple form suggested by Rudinger. For example, along a right-running bicharacteristic from point 1 to point 3 the numerical form of compatibility relation was

$$\Delta_+ P = - \left(AU \frac{\partial \ln A}{\partial \xi}\right)_{1,3} \Delta_+ t + (A)_{1,3} \Delta_+ S$$

where Δ_+ denotes the difference between the quantity value at point 3 and that at point 1. Subscript 1,3 denotes the arithmetic mean between the quantity value at points 1 and 3.

will be called "the centre of mass of the shock system".

2.3.1. METHOD OF CHARACTERISTICS.

The method of characteristics calculation (MOC) is a one dimensional, nonsteady calculation. The interferogrammes taken of the flow (see Chapter 5, section 5.5.4) showed that, to a good approximation, the nozzle flow is one dimensional. The spatial dimension x, is the distance downstream of the nozzle entrance. Time, t, is the time after the projected time of entry of the primary shock into the nozzle, had there been no acceleration of the shock. The choice of flow variables, and the corresponding relations which hold along the bicharacteristic directions and stream trajectories, were taken from G. Rudinger, (1955).

The two state parameters chosen for the calculation are the speed of sound and the specific entropy of the gas. The third independent flow variable, needed to completely solve the problem, is the flow velocity.

The boundary conditions for the problem are specified in a number of ways. The steady gas conditions ahead of the primary shock are input to the computer as a function of distance, x. The restriction on the velocity of propogation of the primary shock is, then, that the post primary shock conditions have to satisfy the compatibility relation along the right running bicharacteristic intersecting the shock from behind (see Fig. 2.2a). The other boundary condition for the flow is the steady flow conditions existing upstream of the nonsteady flowfield. In general, these conditions are specified along a steady, left running bicharacteristic originating at the point where the primary shock first encounters a change in the density ahead of it, or a change in the channel cross-sectional area, whichever is further upstream. This bicharacteristic is the trajectory for the head of the upstream facing nonsteady expansion or compression wave generated by the initial acceleration or deceleration of the primary shock. If the secondary shock moves upstream of this bicharacteristic curve, then the steady test flow conditions become the gas conditions upstream of ~~free stream for~~ the shock. The subsequent shock trajectory and post shock conditions are solved for in the same way as are those of the primary shock except that the secondary shock is intersected from behind by

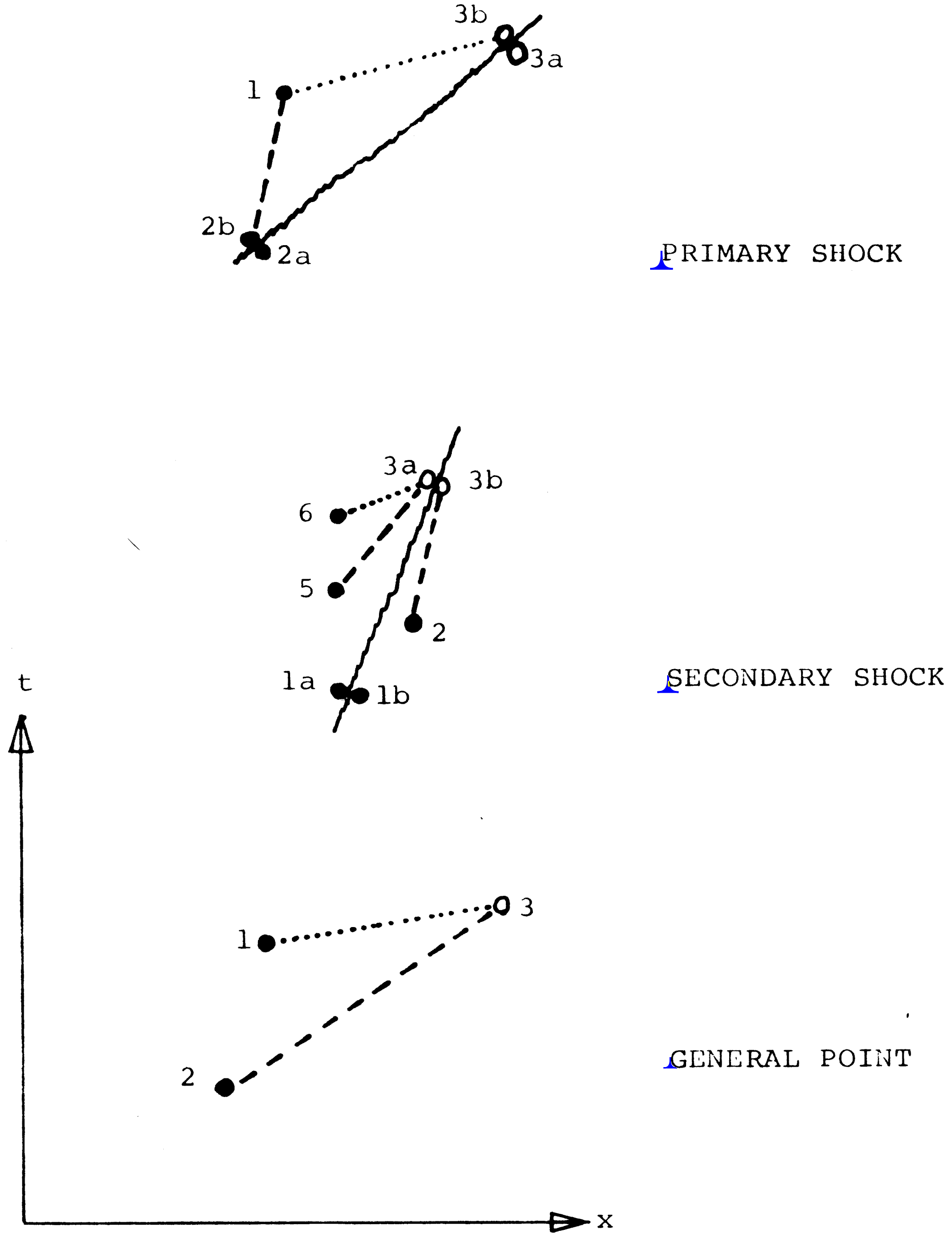

Fig. 2.2. The problem types in the nonsteady MOC programme for nozzle starting processes.

● known point, o point to be calculated.

...... right running bicharacteristic

– – – left running bicharacteristic

~~~~ shock.
~~~~

a left running bicharacteristic.

There are, in general, two types of problem to be solved in the flow field between the two boundaries described above. The most common problem is what is known as the general point problem (see Fig. 2.2c). In this problem, the left running bicharacteristic from one point and a right running bi-characteristic from another point yield the position of a third point in the (x,t,) plane. The compatibility relations along the two bicharacteristics are then solved simultaneously. A stream trajectory is then interpolated back from the third point to the line between the first two points and the relation holding along this trajectory is used to complete the current guess for the flow properties at the third point. This procedure is repeated from the beginning using the current guess for the properties at the third point to improve the values for the property gradients along the characteristic directions. The calculation stops when the series of guesses for the third point position and properties converges sufficiently.

The second type of internal problem is that of finding the trajectory of the second shock, when it is still moving into the nonsteady expansion (see Fig. 2.2b). A general point problem has to be solved to find the gas conditions upstream of the shock. The two initial points necessary for this are interpolated between two known points in the non-steady expansion. The new guess for the shock Mach Number is then found by requiring, as usual, that the post shock conditions satisfy the compatibility relations along the left running bicharacteristic intersecting the shock from behind.

It should be noted here that the nonsteady flow is multi-isentropic. Both shocks in the system accelerate and the conditions ahead of them are, in general, not constant over their paths in the (x,t,) plane.

As well as this, the secondary shock processes gas which has already passed through the primary shock. The result is that adjacent stream trajectories may have different entropies, although the entropy along a stream trajectory remains constant except where it passes across a shock.

The primary shock speeds for the nonsteady M.O.C. calculation are 0.71 cm/μsec for $\gamma = 1.4$ and 0.66 cm/μsec for $\gamma = \frac{5}{3}$ prior to the entry of the shock into the nozzle.

3.2 RESULTS OF M.O.C.

Method of characteristics calculations were carried out for two ratios of specific heats, γ=I.4 and γ=5/3. The primary shock speeds for these two cases were those for an initial shock tube pressure of I"Hg of air and of argon respectively. For each γ, two calculations were made, one with a prior steady flow and one without.

From the results of these calculations, graphs have been drawn, on the (x,t,) plane, of the trajectories of the primary shock, the secondary shock, and the head of the nonsteady expansion and the left running bicharacteristics which intersect to form the secondary shock. These are shown in Fig. 2.3.

It can be clearly seen, from the graphs, that the secondary shock is substantially weakened by the presence of the prior steady flow and remains downstream of the head of the nonsteady expansion until some distance downstream of the test section. When there is no prior steady flow, the secondary shock forms early, on the steady (u-a) bicharacteristic originating at the nozzle throat, and then moves upstream, relative to that bicharacteristic curve, and travels far into the steady flow.

The effect of the change in γ shows up most strongly in the thickness of the starting shock system. The density ratio across both shocks decreases with γ and so the rate of growth of the shock system thickness increases with γ.

3.3 THE ANALYTIC MODEL.

The analytic model was developed before the M.O.C. programme. A simple version of it was used in conjunction with the early experiments on a nonreflected shock tunnel reported in R. Stalker and N. Mudford (I973).

If, by a simple method, we can find the trajectory of the double shock system and also that of the nonsteady expansion wave (if any), then we will have a fairly complete picture of the nonsteady flow field, without resort to the time consuming M.O.C. programme.

In order to write down a reasonably simple equation of motion for the starting shock system, three assumptions were made:

Fig. 2.3. Method of characteristics calculation of the trajectories of the main features in the nonsteady starting flowfield. Time is measured from the (projected) time of arrival of an undisturbed primary shock at the nozzle entrance. The trajectory of the head of the nonsteady expansion wave is shown on both PSF and NO PSF graphs to facilitate comparison of the two cases, although the HNE only occurs in the PSF case.

Codes on the graphs:

PS - primary shock, SS - secondary shock,

HNE - head of the nonsteady expansion wave,

PSF - a prior steady flow exists ahead of the primary shock.

NO PSF - there is no prior steady flow ahead of the primary shock; the gas conditions ahead of the shock are the initial shock tube conditions.

The value of the ratio of specific heats is shown with each graph.

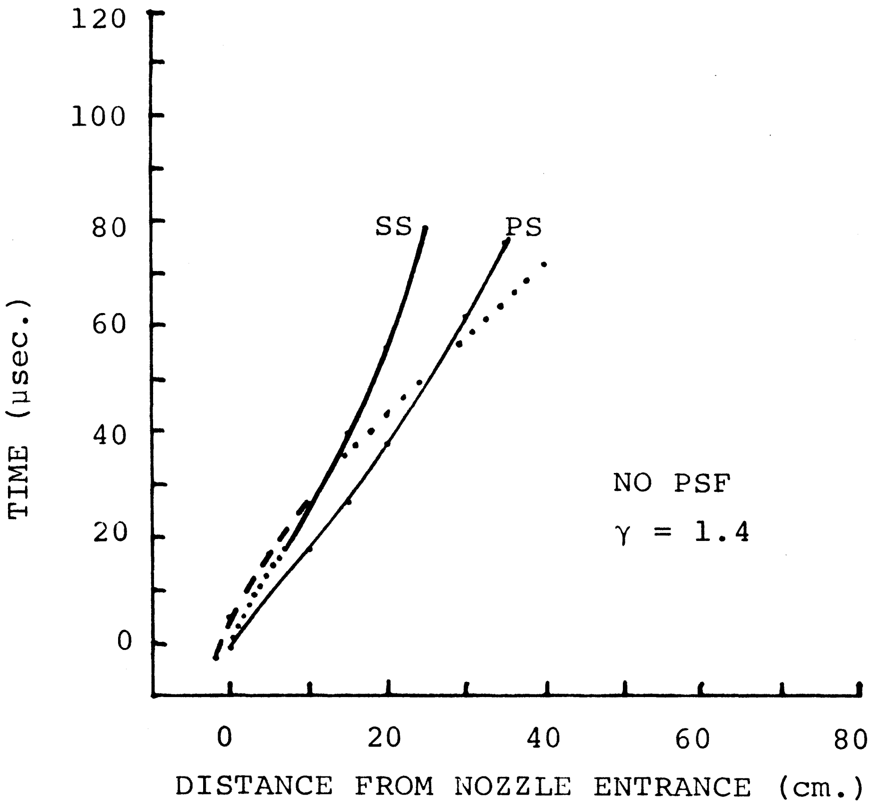

TIME (µsec.)
120
100
80
60
40
20
0
SS
PS
NO PSF
γ = 1.4
0
20
40
60
80
DISTANCE FROM NOZZLE ENTRANCE (cm.)

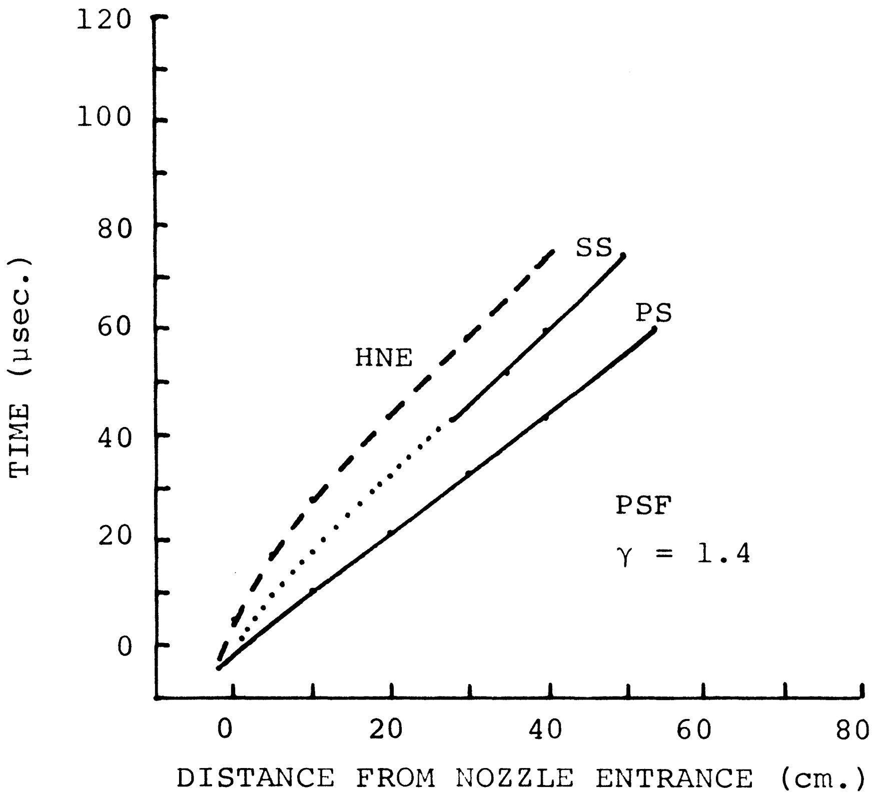

TIME (µsec.)
120
100
80
60
40
20
0
SS
PS
HNE
PSF
γ = 1.4
0
20
40
60
80
DISTANCE FROM NOZZLE ENTRANCE (cm.)

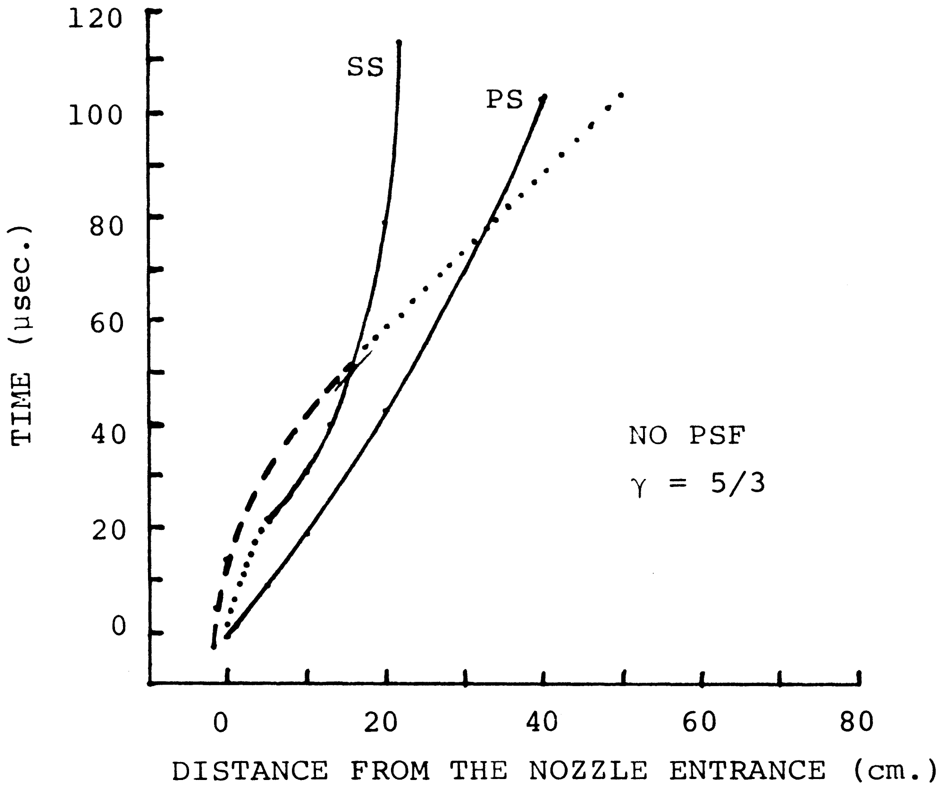

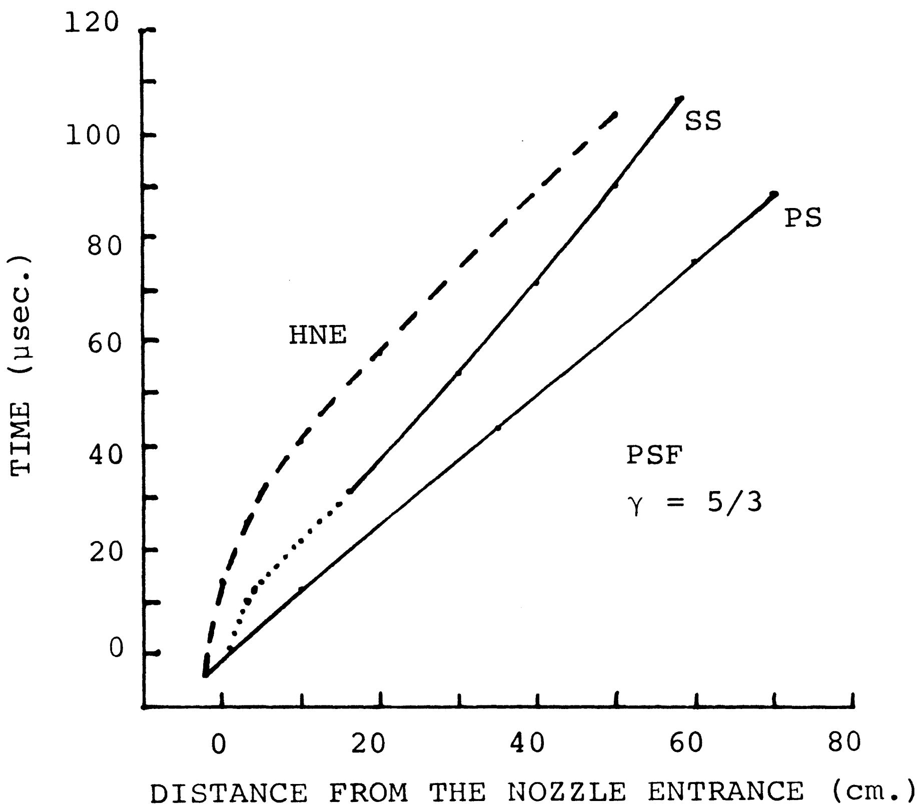

Fig. 2.3. Trajectories of the features in the nonsteady flowfield from MOC. (see previous page for details)

ASSUMPTION 1: The flow is approximately one-dimensional. This is the same assumption as made in the MOC calculation and is justified in the same way.

ASSUMPTION 2: The separation distance betwen the primary and secondary shocks is small compared to the distance over which the nozzle cross-sectional area ratio changes significantly.

This second assumption allows us to assign, to the double shock system, a single point, only, in the (x,t) plane at any one time. The primary and secondary shocks then reside at the same nozzle area ratio and the gas conditions upstream and downstream of the shock system are those appropriate to that one area ratio. The assumption has the effect that the trajectory calculated is that of the centre of mass of the shock system.

The shock system width has been measured from the interferogrammes (see Chapter 5) for shots with a PSF. The largest nozzle area ratio change over a typical shock system width is that from $A/A_t=7$ to 10. This will not represent a large change in the gas properties on either side of the shock system compared with those, say, at $A/A_t=8.5$. At other stations in the nozzle, the A/A_t gradient with x is much smaller.

ASSUMPTION 3: The gas ahead of the primary shock has negligible momentum compared to that imparted to it by the primary shock.

The speed of a section of gas in the PSF is, roughly, 10% of the post primary shock flow speed. The inclusion of this assumption means that the arrival time of the shock system, at a station, will tend to be overestimated for the cases where a prior steady flow exists.

We now write down the integrated momentum equation for the shock system centre of mass:

$$\int_0^t u\,dm + \int_0^t \Delta p.A\,dt - m\,\frac{dz}{dt} - \frac{dz}{dt}\int_0^z \rho_3 A\,dx = 0 \qquad \ldots(2.3\text{-}1)$$

(z,t) = coordinates of the shock system, on the (x,t) plane, at time t.

u = gas speed immediately upstream of the secondary shock.

$m = \int_0^t dm$ = mass which has passed through secondary shock up until time t.

Δp = static pressure difference across shock system.
= (upstream pressure - downstream pressure)

A = nozzle cross-sectional area at x.

$\rho_3 = \rho_3(x)$ = gas density ahead of primary shock.

The initial conditions, implicit in the above equation, are (z,t,) = (0,0) and that initially, there is no mass in the shock system. The initial shock system speed was taken to be the steady flow speed at the nozzle throat.

In speaking of initial conditions, it is appropriate to point out that, although the secondary shock does not form until some distance down the nozzle (see M.O.C. results in Fig.2.3), the equation above is valid for the mass of gas entrained between the primary shock and the bicharacteristics which eventually intersect to form the secondary shock. These bicharacteristics originate not far downstream of the throat.

The first term in equation (2.3.I) above, represents the momentum addition to the shock system due to the passage of gas across the secondary shock. The second term represents the integral of the impulse of the pressure differential across the shock system. The remaining terms represent the current momentum of the system (i.e. at time t).

A further assumption is required to find solutions to this equation of motion:

ASSUMPTION 4: The gas flow conditions upstream of the secondary shock wave can be taken to be those for the steady test gas flow.

Steady test flow conditions will exist upstream of the secondary shock when there is no prior steady flow. However, when prior steady flow exists, there will, in general, be a nonsteady expansion between the secondary shock and the steady flow. The assertion made in Assumption 4. is that, although the gas conditions at the tail of the nonsteady expansion may be significantly different from those of the steady flow at the same station, their overall effect on the shock system trajectory will be quite similar.

It should be noted here that, because of this last assumption, the shock system speed must be less than, or equal to, the steady flow speed at each station, x. This restriction often had to be applied near the nozzle throat in the cases where a prior steady flow was present. The static pressure impulse, acting on the small amount of gas entrained in the shock system in this region, predicted a higher than steady flow speed for the system. The application of this restriction would tend to lead to an overestimation of the time of arrival of the shock system at any station.

The simplest way to check Assumption 4, and the analytic model in general, is to compare the trajectories of the centre of mass of the shock system, given by this model, with those predicted by the M.O.C. calculation. The integrals in the equation of motion were evaluated numerically on a Hewlett Packard HP9830a computer, using Simpson's rule. The graphs of the resulting trajectories are shown in Fig. 2.4.

It can be seen from the graphs that, in all cases, there is good agreement between the methods of calculation. In all cases the time of arrival of the shock system at a station is, as expected, overestimated by the analytic model.

2.4 THEORY AND EXPERIMENT

A comparison was made of the shock trajectories predicted by the analytic model and the arrival times of the primary and secondary shocks at a particular nozzle station, in the test section, as measured from the interferogrammes (see Chapter 4, section 4.3.6 for the details of how the interferogrammes were obtained and Chapter 5, section 5.3. for discussion of the measurement of the pressure disturbance trajectories).

The steady flow upstream of the shock system was calculated, for input to the analytic model, by the computer programmes ESTC and NFAPC (see Appendices B and C). Chemical dissociation, ionisation, electronic exitation and, in the case of the argon shots, enthalpy loss through radiation in the shock tube, were taken into account in these programmes. For a discussion of the implementation of these programmes, in solving the equations for steady flow, see Chapter 5.

The results of the calculations are shown, with the experimentally measured shock arrival times, in Fig. 5.8. In all cases there is reasonable agreement between theory and experiment as regards the starting shock system behaviour.

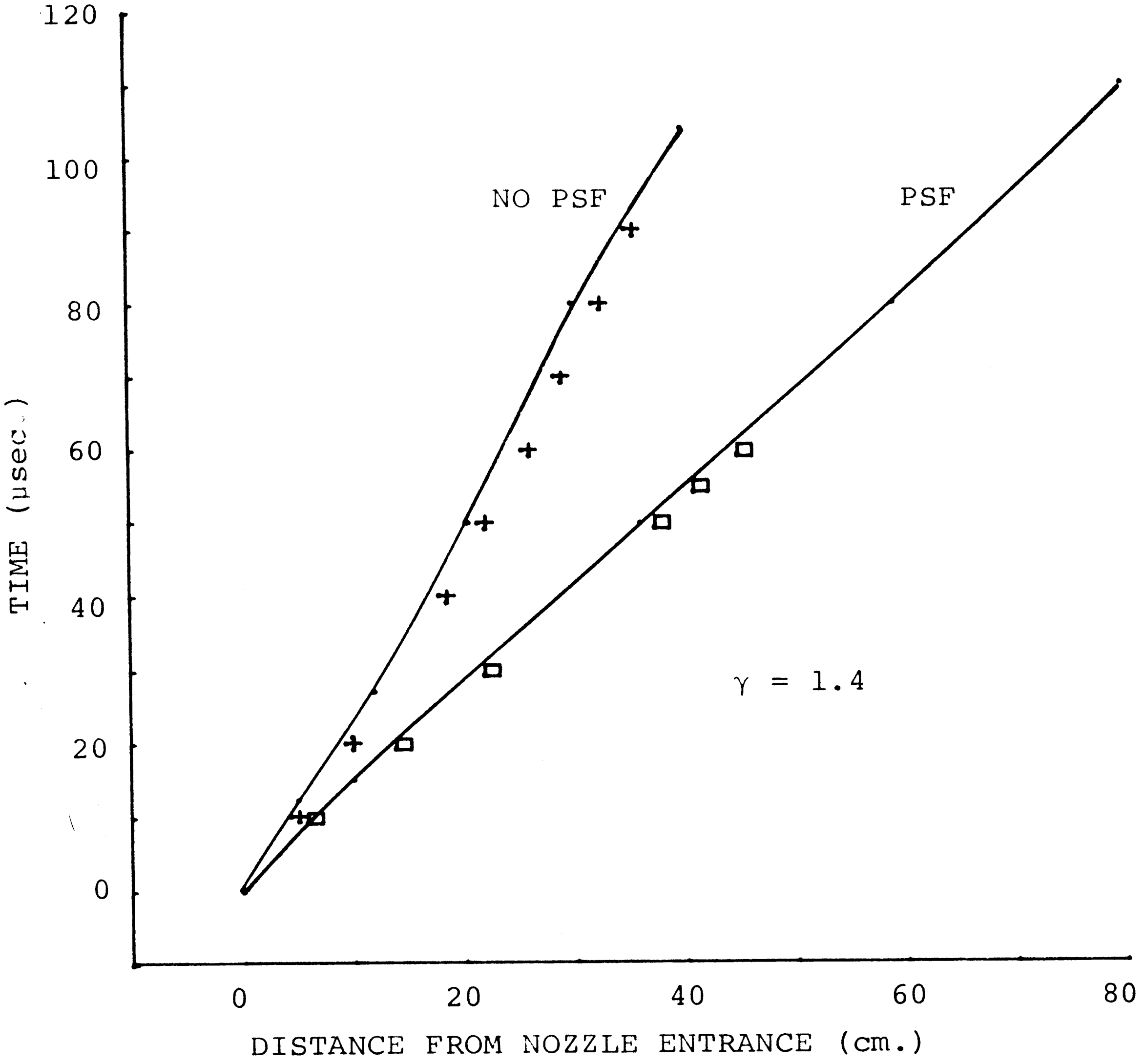

Fig. 2.4. Comparison of the Method of Characteristics and the Analytic Model for the nonsteady flowfield. Shown are the trajectories for the instantaneous centre of mass* for the case of a PSF and the case of NO PSF as calculated by the two methods for γ=1.4

□ , + - Method of Characteristics PSF and NO PSF cases respectively.

——— - Analytic Model (PSF and NO PSF marked on the curves)

*of the starting shock system.

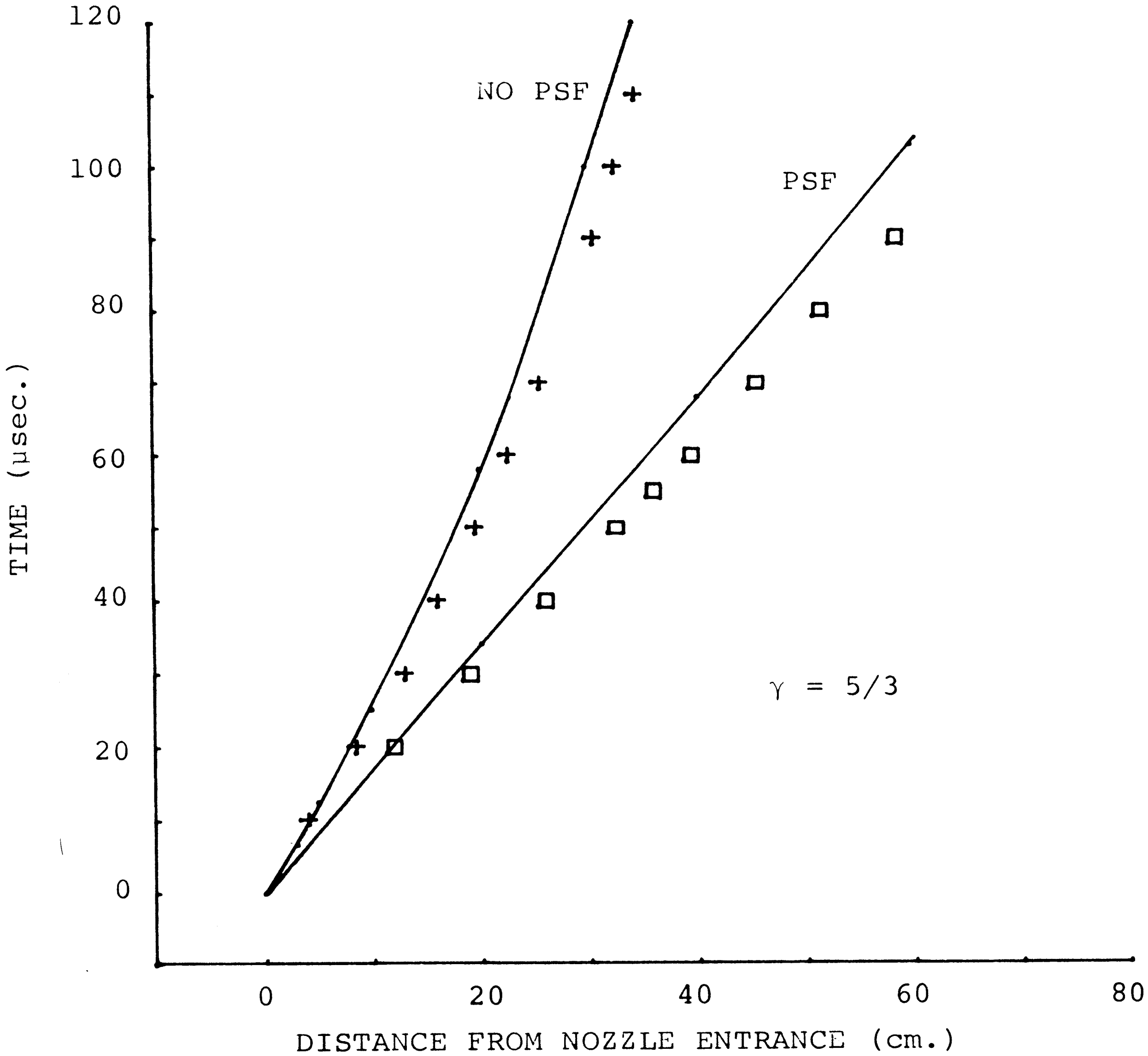

Fig. 2.4.(Cont.) See notes previous page. $\gamma = 5/3$.

The analyses presented in the following two sections are due to R. Stalker (1976).

2.5. CONTACT SURFACE MATCHING.

While the contact surface is in the shock tube, the driver and test gas pressure and velocity are matched across it. When the contact surface passes into the expanding nozzle this matching will not, in general, continue. The test gas flow Mach Number in the shock tube lies between 2 and 4 (see Figs. 5.18 and 5.25). The driver gas Mach Number, on the other hand depends on the shock speed. At the high shock speeds, the driver gas Mach Number is high. The driver gas then expands to a lower velocity than the test gas and a rarefaction wave travels into both gases. At the lower shock speeds, the driver gas Mach Number is lower. In this case, the driver gas expands to a higher velocity and lower pressure than the test gas. The compression wave which subsequently appears in the driver gas is treated as a normal shock for the purposes of performing calculations for this second, more interesting, case.

The normal shock stays close to the contact surface because the mismatch only becomes serious after the driver gas has expanded to a higher Mach Number (>3) in the nozzle. A calculation made for a shock Mach Number of 19 into 10 torr of air with He as driver gas, showed that the pressure remained matched across the contact surface for a driver gas Mach Number of 1.5 in the shock tube. For a driver gas Mach Number of 1.0, the post shock pressure in the driver gas was higher than the test gas pressure and a compression wave propogated into the test gas. A driver gas Mach Number of 2.25 produced a lower pressure than the test gas at the contact surface and a rarefaction wave propogated into the test gas.

Calculations made using the experimental gas conditions showed that, for the 2" Hg and 1" Hg shots, no pressure disturbances should propagate into the test gas. Shots with higher initial pressures, where a strong compression travelling into the test gas might be expected, were not performed. The rarefaction wave, expected in the test gas at lower initial pressures will travel along the steady (u+a) bicharacteristic originating at the nozzle entrance at the time of entry of the contact surface. This bicharacteristic represents the minimum pentration of a disturbance from the contact surface mismatch.

The fact that the calculations show that the matched condition is inside the range of experimental shock conditions indicates that the disturbance in the test gas will not be a strong disturbance. The interferogrammes, taken on the flow in the test section, (see Chapter 5) show, in fact, that the contact surface mismatch disturbance is very small indeed. In many cases, no fringe shift can be detected across the region of the contact surface.

2.6. MINIMUM NOZZLE LENGTH.

The perfect gas nozzle design programme, described in Chapter 3, was used to calculate the minimum nozzle lengths for a large range of γ and test gas conditions. The results of these calculations showed that the minimum total nozzle length, X, could be expressed approximately as

$$X \simeq 1.3\ M_T\ R_T \qquad \text{...(2.7-1).}$$

where M_T and R_T are the nozzle exit Mach Number and radius.

Neglecting the presence of the starting shock system, the steady flow test time lost due to the presence of the nonsteady expansion wave, is equal to the difference between the arrival times of a steady flow particle trajectory originating at the nozzle throat at t = 0 and the steady (u-a) bicharacteristic originating at the same point:

$$\Delta t = \int_0^X \frac{a}{u(u-a)}\, dx = \int_0^X \frac{1}{M-1}\frac{dx}{u} \qquad \text{...(2.7-2)}$$

In Fig. 5.8. the trajectories of the steady (u-a) bi-characteristics originating at the nozzle throat at the time of primary shock entry are shown with the trajectories of the other important nonsteady flow features for the range of shock conditions.

Δt can be approximated by

$$\Delta t - \Delta t_s \simeq \frac{1}{M_T\sqrt{2}\,U}\int_0^X dx = \frac{X}{M_T\sqrt{2}\,U} \simeq \frac{R_T}{U} \qquad \ldots(2.7\text{-}3)$$

where Δt_s is the test time lost due to the fact that the flow is supersonic and not hypersonic in the upstream sections of the nozzle. U is the flow speed behind the normal shock $\simeq$(test section flow speed)/ $\sqrt{2}$.

The test slug length in the tube is limited to a few shock tube diameters in a high enthalpy shock tube. Equation (2.7-3) shows that the nozzle exit radius is thereby limited to a few shock tube radii. A further restriction on the nozzle dimensions is that the nozzle inlet radius must be of the order of the shock tube radius in order to preserve the high mass flows in the tunnel. The combination of these restrictions means that the nozzle area ratio must be small in a non-reflected shock tunnel.

CHAPTER 3. NOZZLE DESIGN.

3.1. INTRODUCTION.

The requirements and restraints placed on the design of a hypersonic nozzle for the nonreflected shock tunnel are the following:

(i) The nozzle must be axisymmetric.

(ii) The nozzle must be as short as possible.

(iii) The steady flow produced by the nozzle must be both hypersonic (defined as Mach Number $\geq$ 5) and uniform.

The requirement that the nozzle be axisymmetric is made so that the strong boundary layer crossflow effects found in two-dimensional nozzles are avoided. The requirement is consistent with requirements (ii) and (iii) because an axisymmetric nozzle achieves a large area ratio in a short distance without requiring a large flow divergence angle anywhere in the flow.

The second requirement arises from the fact that the test time losses due to nonsteady starting and finishing processes increase with increasing nozzle length. Later in this chapter, the minimum possible nozzle lengths will be discussed.

The subject of the third requirement is the desired properties of the steady test section flow. This flow is produced by a steady expansion from the flow behind the primary shock in the tube. The Mach Number of the tube flow lies between 2 and 4 and depends on the composition of the test gas and the primary shock speed. Steady nozzle flow calculations made with computer programme NFAPC (see appendix C) showed that a nozzle area ratio of at least 16 was needed to produce a test section flow with a Mach Number of 5 or more, for all gas conditions.

Having established that the nozzle must be short, axisymmetric, and have an area ratio of 16, we must then decide what the distribution of area ratio along the nozzle axis direction should be so that a uniform test section flow is produced. The choice of this area distribution is the most critical part of the nozzle design. In an axisymmetric nozzle, the strength of an expansion originating at the nozzle wall increases as the axis of symmetry is approached. If the rate of change of area ratio with distance along the

In chapter 5 it is shown that the length of the test gas slug in the apparatus is between 50% and 100% of the nozzle length over the range of gas conditions. In view of this fact it is appropriate to give further consideration to the steadiness or otherwise of the region of the flow between the head of the non-steady expansion (HNE) and the disturbance arising from the entry of the contact surface into the nozzle.

In all the flows considered here the post primary shock flow in the tube is supersonic and a steady expansion of this flow will also, therefore, be supersonic. In the absence of shock waves, a portion of a supersonic flow is affected only by conditions upstream of itself. Consider the test gas flow a short time after the entry of the head of the HNE into the nozzle. The section of flow between the HNE and the shock tube flow must be steady by virtue of the fact that the flow directly upstream of it is steady and that the only change in environment it has encountered since entering the nozzle is an expansion of the channel walls. By applying this argument to later times in the flow development we may conclude that the flow upstream of the HNE will be steady until the arrival of the disturbance caused by the entry of the contact surface into the nozzle.

The computer programme NFAPC which solves the problem of the expansion of a steady, one-dimensional gas flow with chemical reactions may therefore be used to calculate the flow properties of the region of flow between these two non-steady disturbances. If the ratio of the test gas slug length to nozzle length is such that these two disturbances meet prior to arriving in the test section, then NFAPC may still be the most reliable available method of predicting the flow properties between the secondary shock and the contact surface because of the importance of chemical reactions in the flow. The ideal tool for the analysis of the nozzle flows would be a computer programme to solve the problem of a one, or even two, dimensional non-steady flow with chemical reactions. Unfortunately, no such programme is yet available at the A.N.U.

nozzle is too high, then the streamtubes close to the axis will be forced to diverge to a much greater extent than those near the nozzle wall. The inner and outer streamtubes then come together further downstream and shock waves may form in the flow. Such a flow is said to be overexpanded. A conical nozzle, cannot, therefore, be used with the non-reflected tunnel because the expansion from the lip of the entrance to a conical nozzle produces an overexpanded flow.

The approach adopted in designing the nozzle was to make a calculation of a flowfield having the desired properties and, then, to take a streamsurface of the flow as the nozzle shape.

3.2. THE NOZZLE DESIGN COMPUTER PROGRAMME.

3.2.1. The perfect gas programme.

A computer programme was written by I. Shields* to design a suitable nozzle by the method just described. The Method of Characteristics (MOC) for a perfect, inviscid gas with a constant γ was used to perform the necessary nozzle flowfield calculations.

The differential equations governing a steady, supersonic, isentropic axisymmetric flow of a perfect gas are given by Shapiro (1953) in cylindrical coordinates, as:

$$\left(\frac{dr}{dx}\right)_{r,l} = \tan\left(\theta \mp \alpha\right)$$ BICHARACTERISTIC DIRECTIONS (3.2-1)

$$\frac{1}{u}\left[\frac{du}{d\theta}\right]_{r,l} = \mp \tan\alpha + \frac{\sin\alpha \quad \tan\alpha \quad \sin\theta}{\sin\left(\theta \pm \alpha\right)} \; \frac{1}{r}\left(\frac{dr}{d\theta}\right)_{r,l}$$

COMPATIBILITY RELATIONS ALONG BICHARACTERISTIC DIRECTIONS. (3.2-2)

$$\frac{dr}{dx} = \tan\theta$$ STREAMLINE DIRECTION (3.2-3)

$$h_t = \frac{a^2}{(\gamma-1)} + \frac{u^2}{2}$$ INTEGRATED ENERGY EQUATION (3.2-4)

$$S = \text{constant}$$ INTEGRATED ENTROPY EQUATION (3.2-5)

Equations (3.2-4) and (3.2-5) apply along the streamline direction.

---

* internal report, Physics Department, S.G.S., A.N.U.

The subscripts r and l refer to the right and left running bicharacteristics respectively.

(x,r) = coordinates of a point in the physical plane

= (distance along symmetry axis, radius from symmetry axis)

θ = flow angle w.r.t. symmetry axis

α = Mach angle $= \sin^{-1}(1/M)$, where M = Mach No.= u/a

u = flow speed

a = sound speed in the gas $= (\partial p/\partial \rho)_S^{\frac{1}{2}}$

γ = ratio of specific heats

h_t = specific stagnation enthalpy on a streamline

S = specific entropy (constant along a streamline from eqn (3.2.5).

The equations (3.2-1) to (3.2-5) are solved, by the MOC, for the unknown quantities (x,r,u,θ,a,S). The problem is simplified by the fact that, because all the streamlines originate in a uniform region, the specific stagnation enthalpy and specific entropy of the gas are the same for all streamlines.

The unit cell for the numerical approximation to the bicharacteristic network is shown in Fig. 3.1. The numerical approximation to the differential equations (3.2-1) and (3.2-2) used by Shields are:

$$r_3 - r_1 = (x_3-x_1)\ (\tan(\theta-\alpha))_{1,3} \qquad (3.2\text{-}6a)$$

$$r_3 - r_2 = (x_3-x_2)\ (\tan(\theta+\alpha))_{2,3} \qquad (3.2\text{-}6b)$$

$$\theta_3 - \theta_1 + \left[\frac{\cot\alpha}{u}\right]_{1,3} (u_3 - u_1) - \left[\frac{\sin\theta\ \sin\alpha}{r\sin(\theta-\alpha)}\right]_{1,3} (r_3 - r_1) = 0$$

...(3.2-7a)

$$\theta_3 - \theta_2 - \left[\frac{\cot\alpha}{u}\right]_{2,3} (u_3 - u_2) + \left[\frac{\sin\theta\ \sin\alpha}{r\sin(\theta+\alpha)}\right]_{2,3} (r_3 - r_2) = 0$$

...(3.2-7b)

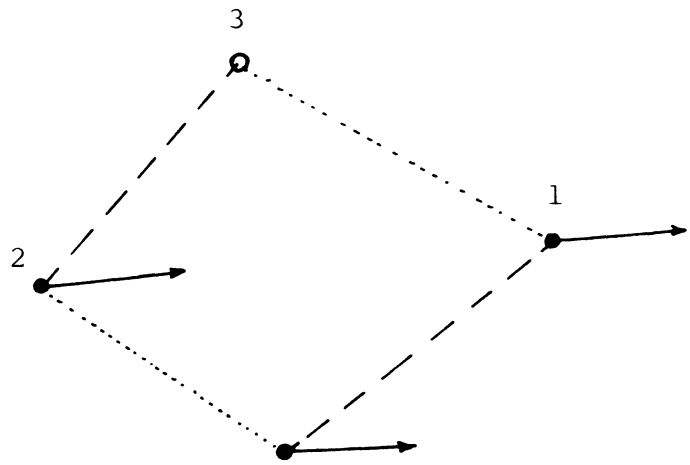

Fig. 3.1. Unit cell for the MOC nozzle design programme.

.... right running bicharacteristic

– – – – left running bicharacteristic

——— streamline

● known point   o point to be calculated

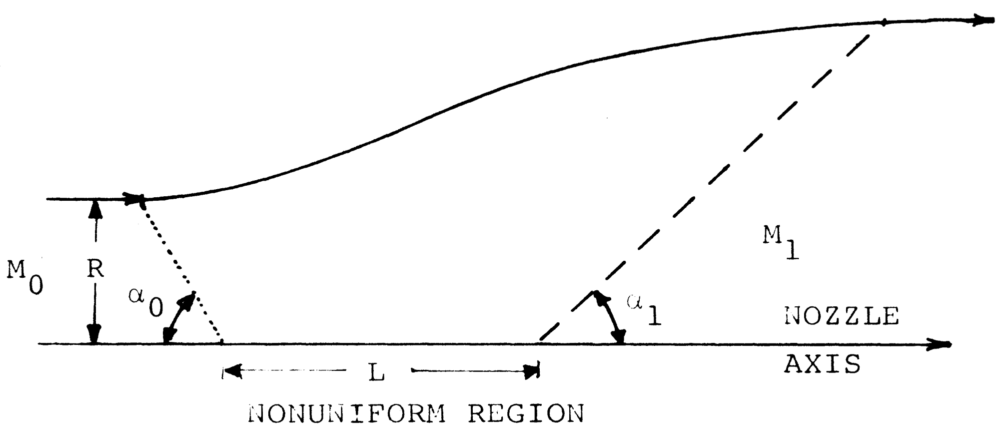

Fig. 3.2. Curves along which the boundary conditions are specified for the nozzle design programme.

.... right running bicharacteristic from the lip of the nozzle entrance.

_ _ _ left running bicharacteristic from the end of the nonuniform region on the nozzle axis.

——— Streamline forming final contour of nozzle.

The single subscripts refer to the numbered points in the unit cell diagram (Fig. 3.1). The double subscripts signify the arithmetic mean of the quantity between the two points referenced in the subscript. Equations (3.2-6) and (3.2-7) were taken from Shapiro (1953) with a slight modification to the method of obtaining a mean value for the trigonometric functions appearing in the equations. Shields uses the mean of the function values from the two points rather than the function of the mean value of the function arguments at the two points.

In certain circumstances, the coefficients of the last terms in equations (3.2-7) become unstable or indeterminate. For example, if point 1. lies near the symmetry axis where θ and r are small, then the expression $\frac{\sin\theta\sin\alpha}{r\sin(\theta-\alpha)}$ in eqn. (3.2-7a) becomes unstable. When this happens, Shields uses a stable, limiting form of the expression, namely

$$\lim_{\substack{r\to 0\\ \theta\to 0\\ \text{along line}\\ 1-3}} \frac{\sin\theta\,\sin\alpha}{r\,\sin(\theta-\alpha)} \simeq \lim_{\substack{r\to 0\\ \theta\to 0\\ \text{along line}\\ 1-3}} \frac{-\theta}{r} \simeq \frac{-\theta_3}{r_3}$$

The other instability allowed for by Shields is that which occurs when a bicaracteristic is nearly parallel to the x axis. For example, if the bicharacteristic between points 1 and 3 in Fig. 3.1 is nearly parallel to the x axis, then $\sin(\theta-\alpha)$ and (r_3-r_1) are small and the last term in equation (3.2-7a) becomes unstable. The following limit is then used in place of this term:

$$\frac{(r_3-r_1)}{\sin(\theta-\alpha)} \simeq \frac{(x_3-x_1)}{\cos(\theta-\alpha)}$$

The replacement expression used if/when the corresponding instabilities occur in eqn. (3.2-7b) are $\frac{\theta_3}{r_3}$ and $\frac{(x_3-x_2)}{\cos(\theta+\alpha)}$ respectively. A Mach Number of 20 would be required before the two types of instability occured simultaneously, so the possibility of this occuring in the nozzle flow can be neglected.

The curves in the (x,r) plane along which the boundary conditions are specified are shown in Fig.3.2 The first curve is the right running bicharacteristic from the lip of

N.B. "curve" is used here in the mathematical sense, i.e. straight lines are included in the definition of a curve.

---

l = distance along nozzle axis from the point of intersection of the right running bicharacteristic originating at the lip of the nozzle throat with the nozzle axis.

the nozzle entrance to the x axis. Along this curve the specified gas conditions are those existing behind the primary shock in the tube. The second curve is the nozzle axis of symmetry between the two regions of uniform flow. Along this curve a smooth distribution of Mach Angle is specified. The distribution used is the following:

$$\alpha = ((\alpha_0 + \alpha_1) + (\alpha_0 + \alpha_1)\cos(\pi(y^3 - 2y^2 + 2y)))/2 \quad \ldots(3.2\text{-}8)$$

where $y=l/L$, L=length of the nonuniform region on the x axis (see Fig.3.2), $0 \leqslant l \leqslant L$, α_0, α_1=nozzle entrance and exit Mach angles.

The distribution produced the shortest nozzles of a number of "smooth" distributions tried by Shields.

The final boundary curve is the left running bi-characteristic originating on the nozzle axis at the end of the nonuniform region. Along this curve the Mach Number is constant and set equal to a chosen nozzle exit Mach Number. The flow angle is zero along this curve and the flow downstream of it is uniform.

After the characteristics network has been calculated, a stream surface, originating at a specified point along the first flow boundary, is interpolated through the network. This surface is then taken as the nozzle shape.

3.2.2 THE MODIFIED NOZZLE DESIGN PROGRAMME.

The computer programme described above assumed the gas to be a perfect gas with constant γ throughout. It is known, however, that strong real gas effects are present in the test gas flow produced in the shock tunnel apparatus. This knowledge led to concern that the presence of these effects might significantly affect the nozzle shape required to produce an acceptable test section flow.

R. Sedney (1970) has considered the full equations (eqn. nos. (3.2-10) to (3.2-15)) for axisymmetric flow with non-equilibrium chemistry and develops the equations necessary for the solution of the problem by the Method of Characteristics (MOC). However, a large and complex programme would be necessary to solve these equations. It was therefore decided that the perfect gas nozzle design programme should be modified to enable it to approximate a nozzle flow with chemical reactions. This would permit an assessment of the effects of the presence of the chemical reactions on the nozzle shape required to produce a test section flow with the desired properties.

The major change made to the perfect gas programme was to replace the perfect gas Mach Number in equations (3.2-1) to (3.2-8) with the Mach Number calculated by the nozzle flow programme NFAPC (see appendix C). NFAPC solves the problem of a steady one-dimensional nozzle flow, with non-equilibrium, frozen or equilibrium chemistry, passing through a given crosssectional area ratio distribution. The gas flow properties are calculated by NFAPC at discrete, closely spaced stations along the nozzle axis. The sound speed, on which NFAPC bases its Mach Number, is calculated by taking the pressure and density at adjacent nozzle stations and forming the following ratio:

$$a_N^{\;2} = \frac{p_2 - p_1}{\rho_2 - \rho_1} \qquad (3.2\text{-}9)$$

a_N is the NFAPC sound speed. Subscripts 1 and 2 refer to the two nozzle stations.

There are two well defined sound speeds for a flow with chemical nonequilibrium: the frozen and the equilibrium sound speeds. The frozen sound speed is defined by

$$a_f^{\;2} \equiv (\partial p / \partial \rho)_{S = \text{constant},\ c_i = \text{constant},\ i=1,\ldots,N}$$

The equilibrium sound speed is defined by

$$a_e^{\;2} \equiv (\partial p/\partial \rho)_{S = \text{constant},\ c_i = c_{ie},\ i=1,\ldots,N.}$$

where S = specific entropy, c_i = specific molar concentration of species i, (moles of i)/(gm. of mixture), c_{ie} = equilibrium c_i, N = number of species present in flow.

Clearly, the NFAPC sound speed is not an approximation to either of these sound speeds because, between nozzle stations 1 and 2, the specific entropy is allowed to vary and the flow chemistry is out of equilibrium but not frozen. The NFAPC "nonequilibrium sound speed", however, expresses the response of the nonequilibrium gas flow to a change in pressure. In this capacity, it was employed in the modified nozzle design programme in the form of the NFAPC "non-equilibrium Mach Number".

The first step in introducing the NFAPC Mach Number into the nozzle design programme was to run NFAPC with the initial gas conditions of interest through an area ratio distribution similar to that of the expected, final nozzle shape. The Mach Number at each station was then plotted against the flow speed over the desired exit to throat area ratio range and a polynomial, of up to 6th order, was fitted to the resulting curve. The polynomial was used by the nozzle design programme whenever it was necessary to obtain the Mach Number from the flow speed or vice versa. In the original perfect gas programme, the energy conservation equation, eqn. (3.2-4) was used for this purpose. The introduction of the M_n vs. u polynomial can therefore be looked upon as a way of varying the ratio of specific heats, γ, in order to approximate the real gas flow more closely than possible with the constant γ model.

Justification for the use of the NFAPC Mach Number is found from a consideration of the flow equations for axisymmetric flow with chemical nonequilibrium presented by Sedney (1970) written in the natural coordinates s,n= distance along streamline, distance normal to streamline:

$$\frac{1}{u}\frac{\partial u}{\partial s} + \frac{1}{\rho}\frac{\partial \rho}{\partial s} + \frac{\partial \theta}{\partial n} + \frac{\sin \theta}{r} = 0 \qquad \text{CONTINUITY (3.2-10)}$$

$$\rho u \frac{\partial u}{\partial s} + \frac{\partial p}{\partial s} = 0 \qquad \text{MOMENTUM IN s DIRECTION (3.2-13)}$$

$$\rho u^2 \frac{\partial \theta}{\partial s} + \frac{\partial p}{\partial n} = 0 \qquad \text{MOMENTUM IN n DIRECTION (3.2-12)}$$

$$h + \frac{u^2}{2} = h_t \qquad \text{INTEGRATED ENERGY EQUATION (3.2-13)}$$

$$\rho u \frac{\partial c_i}{\partial s} = \omega_i, \ i=1,\ldots,N \qquad \text{SPECIES PRODUCTION RATE (3.2-14)}$$

$$TdS = dh - \frac{1}{\rho} dp - \sum_{i=1}^{N} \mu_i W_i dc_i = 0 \qquad \text{GIBBS EQUATION (3.2-15)}$$

where ρ = mass density

p = pressure

u = flow speed

θ = flow angle

h = specific enthalpy

r = radius from axis of symmetry

c_i = (moles of species i)/(gm. of gas mixture), $i=1,..,N$

N = number of species present in the flow

ω_i = rate of production of species i

T = temperature

μ_i = chemical potential of species i

W_i = molecular weight of species i

The NFAPC speed of sound is introduced into the set of equations through the relation:

$$\frac{1}{\rho}\frac{\partial\rho}{\partial s} = \frac{1}{\rho}\left(\frac{dp}{d\rho}\right)_n^{-1}\frac{\partial p}{\partial s} = \frac{1}{\rho a_n^2}\frac{\partial p}{\partial s} \simeq \frac{1}{\rho a_N^2}\frac{\partial p}{\partial s} \qquad \text{...(3.2-16)}$$

This relation defines the "nonequilibrium speed of sound", a_n. The subscript n denotes that the derivative is taken allowing the chemical reactions to proceed at their non-equilibrium rates. Equation (3.2-9) shows that the NFAPC speed of sound is an approximation to the nonequilibrium speed of sound.

The corresponding expression used by Sedney is:

$$\frac{1}{\rho}\frac{\partial\rho}{\partial s} = \frac{-1}{\rho h_\rho}\left(\left(\frac{\rho h_p - 1}{\rho}\right)\frac{\partial p}{\partial s} + \sum_i h_{c_i}\frac{\partial c_i}{\partial s}\right) = \frac{1}{\rho}\left(\frac{1}{a_f^2}\frac{\partial p}{\partial s} - \frac{1}{h_\rho}\sum_i h_{c_i}\frac{\partial c_i}{\partial s}\right) \qquad (3.2\text{-}17)$$

where subscripts denote partial derivatives of $h = h(p,\rho,c_i)$ with respect to the variable mentioned in the subscript. Sedney's equation is obtained by taking the partial derivative of the integrated energy equation along the streamline direction.

Substituting equation (3.2-16) into equation (3.2-11) and then substituting the result into equation (3.2-10) we have

$$\frac{(M_n^2 - 1)}{u}\frac{\partial u}{\partial s} - \frac{\partial\theta}{\partial n} - \frac{\sin\theta}{r} = 0 \qquad \text{...(3.2-18)}$$

where M_n is the Mach Number based on the nonequilibrium speed of sound.

Substituting the differential form of the energy equation (3.2-13) into the Gibbs Equation (3.2-15) and then taking partial derivatives along the streamline direction and normal to the streamline direction, we have:

$$T \frac{\partial S}{\partial s} + \sum_i \mu_i \frac{\partial c_i}{\partial s} = 0 \qquad \ldots(3.2\text{-}19)$$

$$\frac{T}{u^2}\frac{\partial S}{\partial n} + \frac{1}{u}\frac{\partial u}{\partial n} - \frac{\partial \theta}{\partial s} + \frac{1}{u^2}\sum_i \mu_i \frac{\partial c_i}{\partial n} = 0 \qquad \ldots(3.2\text{-}20)$$

In obtaining these equations the fact that the stagnation enthalpy is constant along a streamline and the same for all streamlines has been used. Also equation (3.2-11) was used to eliminate the derivatives of u and p in equation (3.2-19) and equation (3.2-12) was used to eliminate the p derivatives for equation (3.2-20).

Now define the directional derivatives

$$\frac{\partial}{\partial \xi} \equiv \cos(\alpha_n)\frac{\partial}{\partial s} - \sin(\alpha_n)\frac{\partial}{\partial n} \qquad \ldots(3.2\text{-}21)$$

$$\frac{\partial}{\partial \eta} \equiv \cos(\alpha_n)\frac{\partial}{\partial s} + \sin(\alpha_n)\frac{\partial}{\partial n} \qquad \ldots(3.2\text{-}22)$$

where α_n is the Mach Angle based on the nonequilibrium speed of sound.

Equations (3.2-21) and (3.2-22) are the directional derivatives in directions $\pm\alpha_n$ to the streamline direction.

At this point we take the following linear combinations of the equations

$$\sin\alpha_n * (3.2\text{-}18) \mp \frac{\cos\alpha_n}{u^2} * (3.2\text{-}20) + \frac{\sin\alpha_n \cot^2\alpha_n}{u^2} * (3.2\text{-}19)$$

This gives the equations

$$\frac{\cot\alpha_n}{u}\frac{\partial u}{\partial \xi} + \frac{\partial \theta}{\partial \xi} - \frac{\sin\alpha_n \sin\theta}{r} + \frac{\cot\alpha_n}{u^2}\left[T\frac{\partial S}{\partial \xi} + \sum \mu_i \frac{\partial c_i}{\partial \xi}\right] = 0 \quad (3.2\text{-}23)$$

$$\frac{\cot\alpha_n}{u}\frac{\partial u}{\partial \eta} - \frac{\partial \theta}{\partial \eta} - \frac{\sin\alpha_n \sin\theta}{r} + \frac{\cot\alpha_n}{u^2}\left[T\frac{\partial S}{\partial \eta} + \sum_i \mu_i \frac{\partial c_i}{\partial \eta}\right] = 0 \quad (3.2\text{-}24)$$

The question now is whether the ξ and η directions, as defined in equations (3.2-21) and (3.2-22) above, can be considered to be characteristic directions for the flow equations and, therefore, whether equations (3.2-23) and (3.2-24) can be used as compatibility relations, along those directions, to solve the flow problem.

The definition of a "characteristic direction" used by Sedney is one taken from Courant and Hilbert (1962):

"Along a characteristic curve the differential equation (or for systems a linear combination of the equations) represents an interior differential equation".

With respect to a curve, an interior differential equation is one in which the directional derivatives are all taken along the curve direction. Alternatively, it is one in which the values of the derivatives of a function, f, on the curve, depend only on the values of f on the curve. The discovery of these curves along which the governing differential equations take a simple, easily integrable form is the basis of the MOC solution.

Comparison of equations (3.2-16) and (3.2-17) shows that the nonequilibrium sound speed can be written as

$$a_n^2 = \left(\frac{dp}{d\rho}\right)_n = -\left(\left(\frac{\rho h_p - 1}{h_\rho}\right) + \frac{1}{h_\rho\left(\frac{\partial p}{\partial s}\right)} \sum_i h_{c_i}\omega_i\right)^{-1} \qquad \ldots (3.2\text{-}25)$$

This equation shows that a_n has some dependence on the pressure gradient in the streamline direction. This dependence is, however, known to be extremely weak. The pressure gradient in the streamline direction in the one-dimensional flow calculated by NFAPC can be altered by increasing or decreasing the nozzle length while holding the nozzle area ratio constant. Runs of NFAPC with nozzles of various lengths show the nonequilibrium sound speed to be unaffected by a doubling or halving of the nozzle length.

The length and shape of the nozzle used for the nozzle design runs of NFAPC was similar to that of the final nozzle design. The pressure gradients in the flow calculated by NFAPC were therefore similar to those in the final nozzle. The nonequilibrium sound speed at a point can therefore be considered as a function of the flow properties at that point for the purposes of the nozzle design. The ξ and η directions are then bicharacteristic directions and the equations (3.2-23) and (3.2-24) are the compatibility relations for those directions.

The difference in form between equations (3.2-23) and (3.2-24) and the corresponding equations for a perfect gas is the existence of the final terms in equations (3.2-23) and (3.2-24). If the final term in each equation can be shown to be small compared to any other term in each equation, then the final term can be neglected and the perfect gas form of the equations can be used for the MOC calculations.

The procedure employed to assess the relative magnitude of the terms in equations (3.2-23) and (3.2-24) was as follows. Several runs of the modified nozzle design programme were made with the same (M_n,u) relation, the same length of the nonuniform region (L) but with different inlet radii. These runs produced the stream surfaces in the nozzle flow. The distribution of crossectional area ratio of the stream-tubes (annular in form) existing between adjacent stream-surfaces could then be found. These area distributions were input to NFAPC and the distributions of the gas properties. along the streamtubes were found. The nozzle throat conditions were the same ones which were used to produce the (M_n,u) relation above. Approximations to the gas property gradients appearing in equations (3.2-23) and (3.2-24) were then easily found from the gas property distributions along the adjacent stream tubes.

In all the cases examined, the final term in each equation was less than 10% of at least one other term in the equation. It was therefore concluded that the last term could be neglected and the perfect gas form of the equations used, with the NFAPC Mach Number in place of the perfect gas Mach Number.

The second modification made to the nozzle design programme was to specify a smooth flow speed distribution along the nozzle axis in place of the smooth Mach Angle distribution (eqn.3.2-8). The form of the flow speed distribution used was

$$u=((u_o + u_1) + (u_o - u_1)\cos(\pi(y^3 - 2y^2 + 2y)))/2 \qquad \ldots(3.2\text{-}26)$$

where u_o, u_1 = flow speed at the nozzle entrance and exit respectively. y is defined in the same way as for equation (3.2-8).

This change was made to ensure, more directly that the pressure distribution along the nozzle axis was smooth.

3.3. THE NOZZLE DESIGN PROCEEDURE:

The gas used in conjunction with the modified nozzle design programme was a mixture of 60% H_2 and 40% Ne by number. This mixture was to have been used for the tunnel flow experiments. Using the free piston shock tube, it is possible to fully dissociate the hydrogen behind the primary shock in the tube. The resulting simple gas, composed of H atoms, H^+ ions, Ne atoms and electrons, was considered to be ideal for the study of flows with energy loss through electromagnetic radiation. However, it was decided later that the tunnel flows should first be studied using the common gases air and argon. Air was chosen to represent a dissociating gas and argon was chosen to represent an ionising gas. This proved to be such a lengthy task that, in the end, there was insufficient time to perform and analyse the shots in H_2-Ne mixtures.

Nozzle design runs were carried out for the post primary shock gas conditions produced by the shocks shown in the table in Fig. 3.3.

The hydrogen molecules were completely dissociated for all the gas conditions. These shock speeds were produced during a series of shots with a small free piston shock tube known as DDT. The nonreflected shock tunnel was developed

			POST SHOCK CONDITIONS			
COMPUTER RUN CODE	SHOCK SPEED (cm/μsec)	INITIAL SHOCK TUBE PRESSURE ("Hg)	TEMPERATURE (^{o}K)	PRESSURE (atm)	IONISATION FRACTION $\left(\frac{N_e}{N_e + N_H}\right)$	STAGNATION ENTHALPY (MJ/Kg.)
NR	1.30	0.017	10600.	0.325	0.104	154
NS	1.25	0.028	10300.	0.477	0.067	140
NT	1.20	0.045	9904.	0.712	0.039	127
NU	1.15	0.075	9300.	1.069	0.018	116
NV	1.10	0.126	8600.	1.665	0.006	106
NW	1.05	0.197	7900.	2.440	0.002	100

Fig. 3.3. Table of shock conditions, in a 60% H_2: 40% Ne (by number) mixture, used to design the contoured nozzle with the modified nozzle design computer programme.

to produce higher enthalpy flows and this was the reason that high enthalpy gas conditions were considered in the nozzle design.

The nozzle flow programme NFAPC requires specification of the species present in the flow, the reactions which take place between the species and the rates at which reactions proceed. It was considered that the use of a fully comprehensive set of species and a complex reaction scheme was not justified, in view of the simplifications inherent in the modified nozzle design programme.

The species considered in the flow were e^-, H, Ne, H_2, H^+, and H_2^+. The singly ionised neon ion, Ne^+, was omitted from the list because its concentration behind the primary shock was shown, by ESTC, to be negligible compared to the concentration of any of the other species. The chemical reaction scheme and the reaction rate constants for the H_2-Ne mixture nozzle flows are shown in Fig. 3.4. Several of the reactions in the flow have similar rate constants for different third bodies. The rate constant assigned, is, in all cases, the largest for the range of third bodies. For the assessment of the effects on the nozzle shape of chemical reactions in the flow, it was felt that, if anything, an overestimation of the reaction rates was desirable.

The results of the NFAPC nozzle flow calculations show that the hydrogen atom recombination freezes in the nozzle at an area ratio of between 3 and 6. The deionisation of hydrogen ions does not freeze but stays in nonequilibrium for the full length of the nozzle.

Only one report could be found in the literature of an experimental verification of the ionisation reaction rates (Liebowitz (1973)). There is therefore some uncertainty associated with these rates. In order to assess the effects on the nozzle shape of an error in these ionisation rates, a series of design runs was made with the modified design programme using arbitrarily increased rates. The rate of reaction 3 (see table Fig. 3.4) was multiplied by a factor of 125 and the rate of reaction 4 was multiplied by a factor of 30.

In Fig. 3.5 the M_n vs. u curves for the nozzle flows with the standard reaction rates and the overestimated rates are shown for three of the shock conditions listed in the

REACTION	THIRD BODY M	REACTION RATE CONSTANT $cm^3\ mole^{-1}\ sec^{-1}$	REFERENCE
$H_2 + M \rightleftarrows 2H + M$	e^-, H, Ne, H_2, H^+	$8.34 \times 10^{19} T^{-1} \exp\left(\frac{-1.031 \times 10^5}{R_c T}\right)$	1.
$H + M \rightleftarrows H^+ + e^- + M$	H, He, H+	$4.94 \times 10^{11} T^{0.5} \exp\left(\frac{-2.305 \times 10^5}{R_c T}\right)$	2.
$H + e^- \rightleftarrows H^+ + 2e^-$	————	$2.81 \times 10^{13} T^{0.5} \exp\left(\frac{-2.305 \times 10^5}{R_c T}\right)$	3.
$H_2 + M \rightleftarrows H_2^+ + e^- + M$	e^-, H^+, Ne	$1.29 \times 10^{14} T^{0.5} \exp\left(\frac{-3.55 \times 10^5}{R_c T}\right)$	4.

1. Liebowitz (1973), Jacobs et al (1967), Patch (1962), Rink (1962), Bauer(1951).
2. Liebowitz (1973), Stier and Barnett (1956), Bauer(1951).
3. Liebowitz (1973), Goodyear and Von Engel, (1962), Fite and Brackman (1958 a and b).
4. Liebowitz (1973), Goodyear and Von Engel,(1962), Tate and Smith (1932), McClure (1964).

Fig. 3.4. The reaction scheme and rates for the nozzle flos of the H_2 : Ne gas mixtures used to design the contoured nozzle. The references cited in the last column in the table are those considered in chosing the reaction rate. In each case, the highest rate was chosen from the set of rates for the different third bodies. $R_c = 1.986$ cal/mole/^oK.

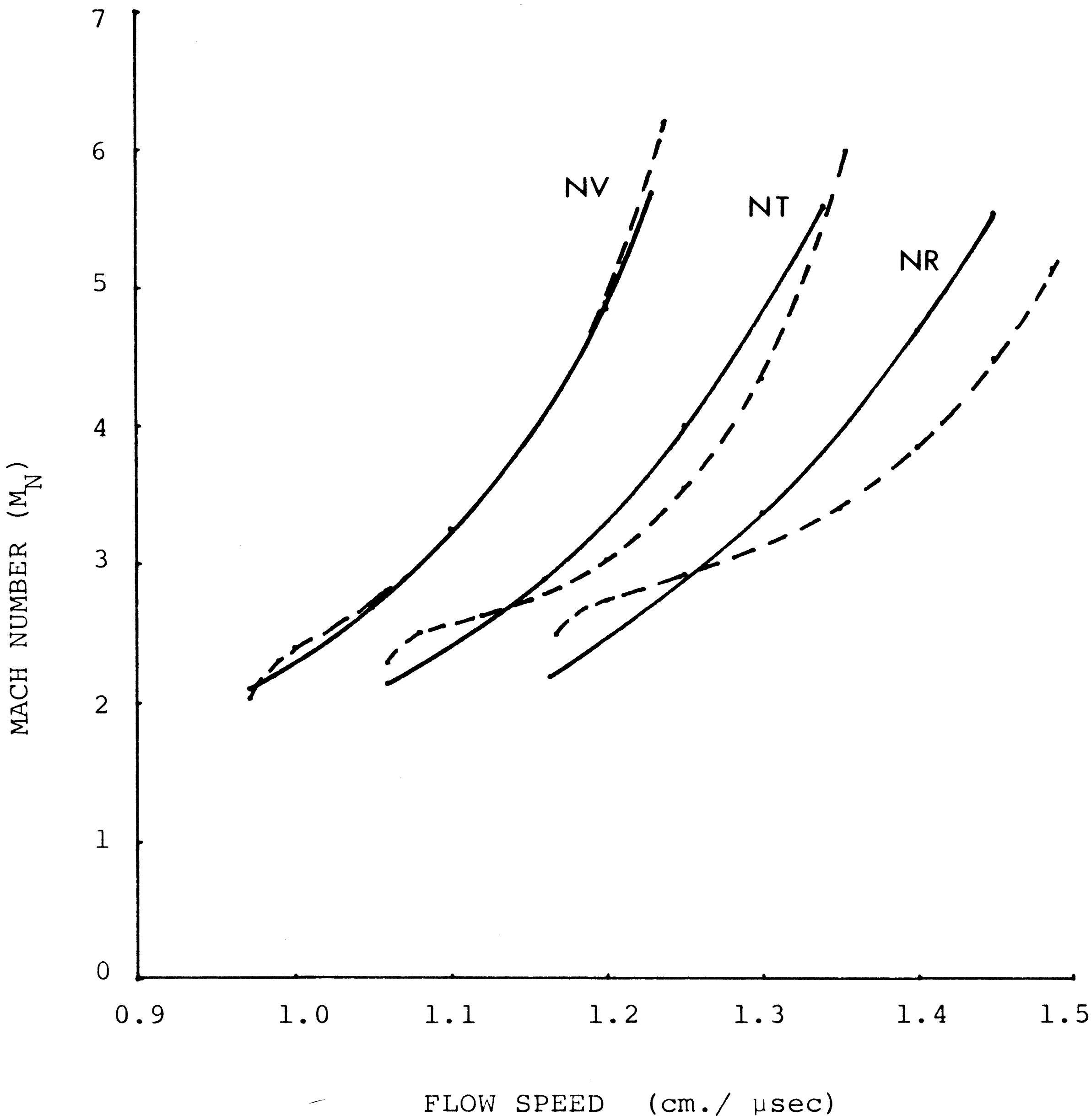

Fig. 3.5 Mach Number (M_N) vs. Flow Speed curves for shock conditions NR, NT, NV (see Fig. 3.3).

______ standard reaction rates

_ _ _ overestimated reaction rates.

table in Fig. 3.3. Not unexpectedly, the difference between the curves for the two sets of rates increases with the increase in the reservoir ionisation fraction.

The nozzle shapes which result from the M_n vs u curves in Fig. 3.5 are shown in Fig. 3.6. It will be noted that, although quite appreciable differences occur between the M_n vs. u curves for the various shock conditions and the two sets of reaction rates, the scatter in the range of nozzle shapes derived from the curves is quite small. The nozzle radius at any nozzle station does not differ from the mean of the radii at that station by more than ±0.05".

The nozzle shape chosen for use in the experiments was the curve closest to the nozzle axis in Fig. 3.6. This curve derives from the highest enthalpy shot (NR) and is calculated using the overestimated ionisation reaction rates. The curve closest to the axis was chosen so that the danger of overexpansion of the flow was minimised.

Shown in Fig. 3.7 is a comparison of the chosen nozzle shape with that produced for the same gas conditions and reaction rates but with a smooth Mach Angle distribution (eqn. (3.2-8)) specified on the nozzle axis in the modified nozzle design programme. Also shown in this figure is the corresponding nozzle shape given by the perfect gas nozzle design programme. The deviation of these shapes from the chosen nozzle shape is seen to be small (±0.05").

A diagram of the various regions and their boundaries in the contoured nozzle flow is shown in Fig. 3.8.
The region of uniform flow in the nozzle flow, as designed by the design programme, is the region downstream of the Mach cone originating on the point of the nozzle axis where the nonuniform flow ends.

As discussed at the beginning of this chapter, test time losses, due to the nonsteady starting and finishing processes, increase with increasing nozzle length.To reduce these losses. the nozzle was truncated at the nozzle axis station 13.2" downstream of the nozzle entrance. Because of the low test section pressures outside the nozzle flow in the test section, an expansion fan will exist downstream of the right running bicharacteristic surface originating around the rim of the nozzle exit. The final region of the uniform flow is, therefore, the biconical region between the beginning of the

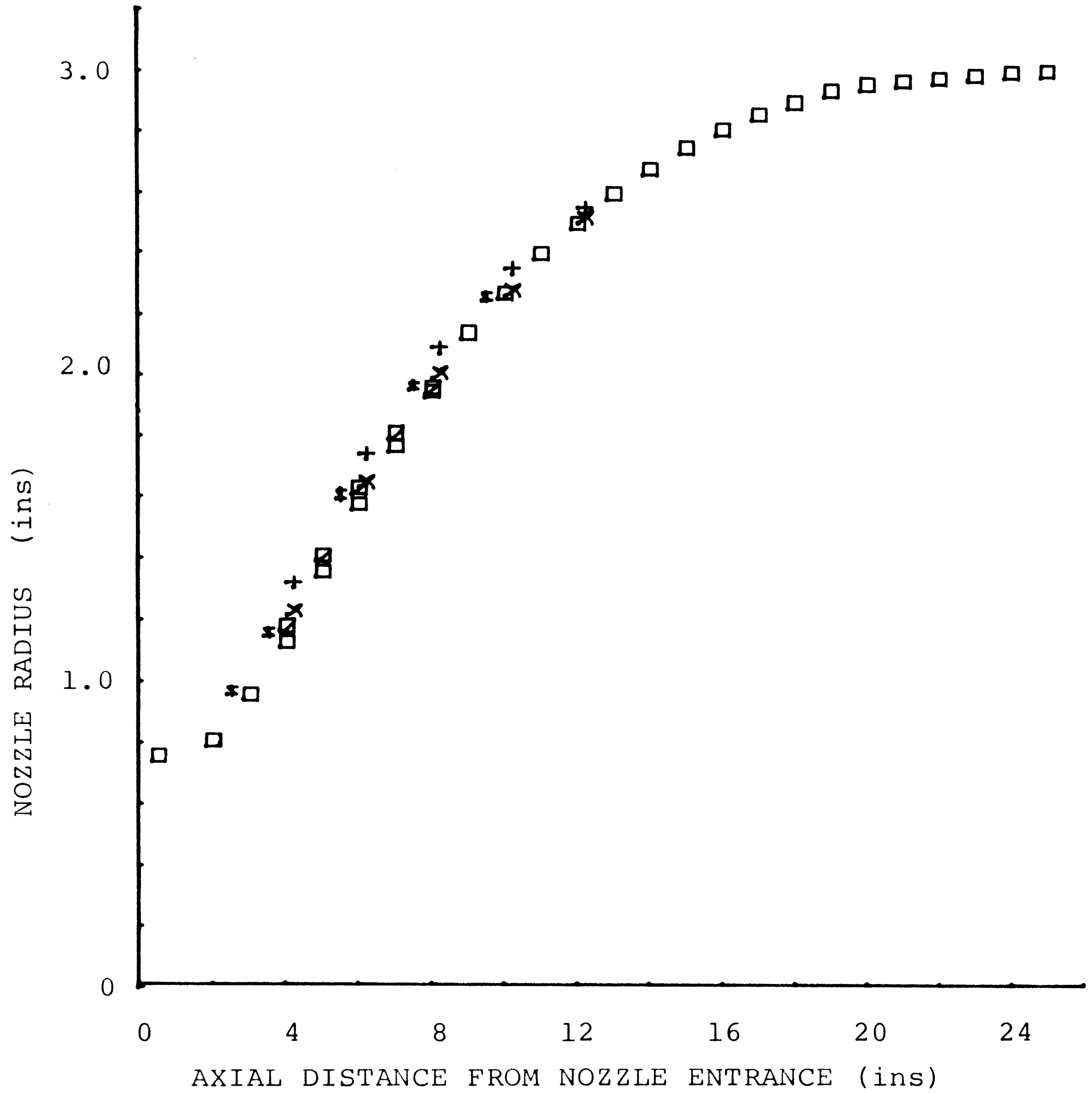

Fig. 3.6. Nozzle shapes for the M_N vs. u curves shown in Fig. 3.5.

	overestimated rates	standard rates
NR	□	⊠
NT	+	×
NV	*	SAME SHAPE AS FOR OVERESTIMATED RATES.

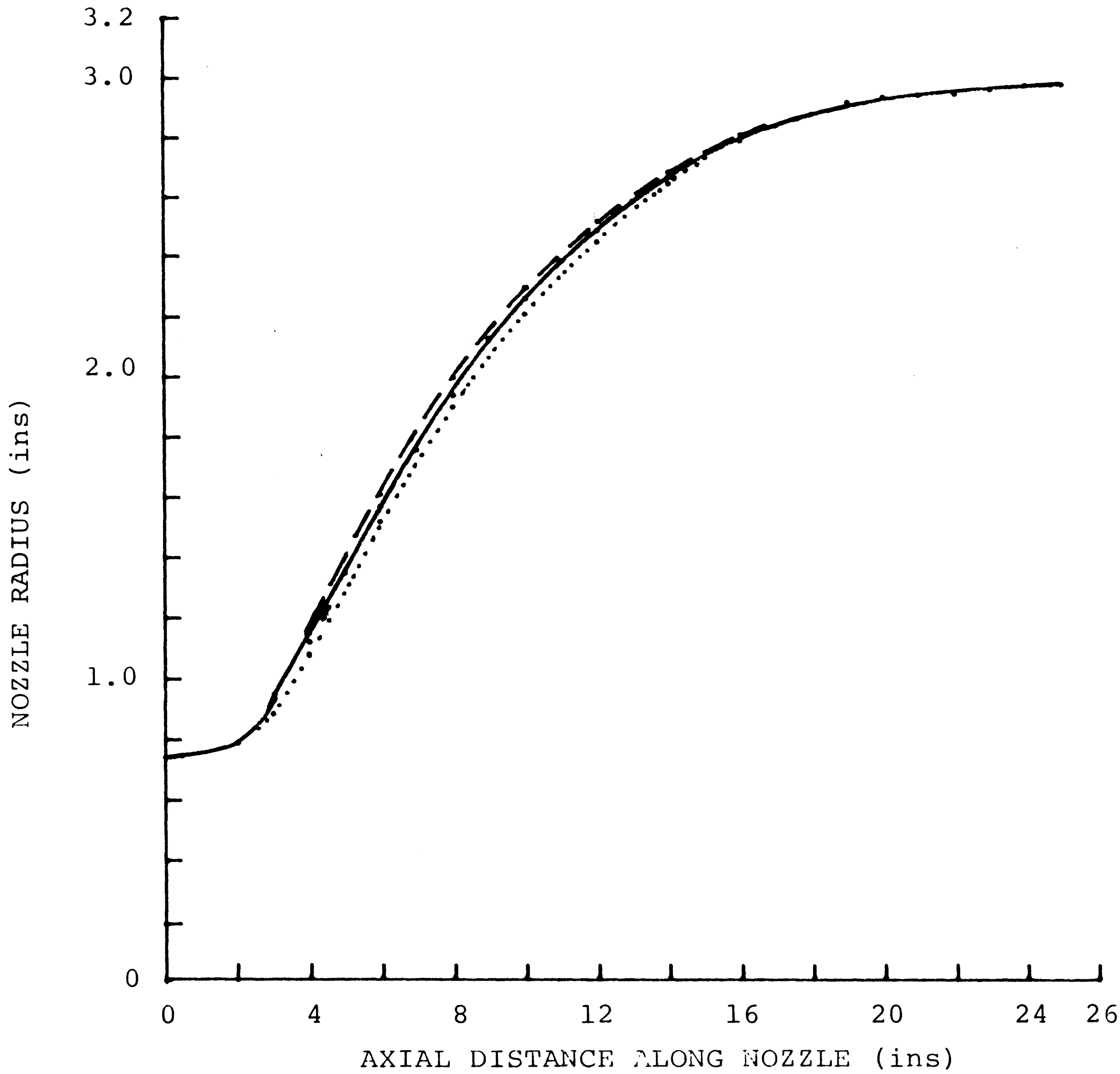

Fig. 3.7. Comparison of nozzle design methods.

______ modified programme with smooth flow speed distribution on axis.

_ _ _ modified programme with smooth Mach Number distribution on axis.

...... perfect gas programme.

All nozzle shapes are for gas conditions NR and the overestimated reaction rates. The full curve is the shape used in the experiments.

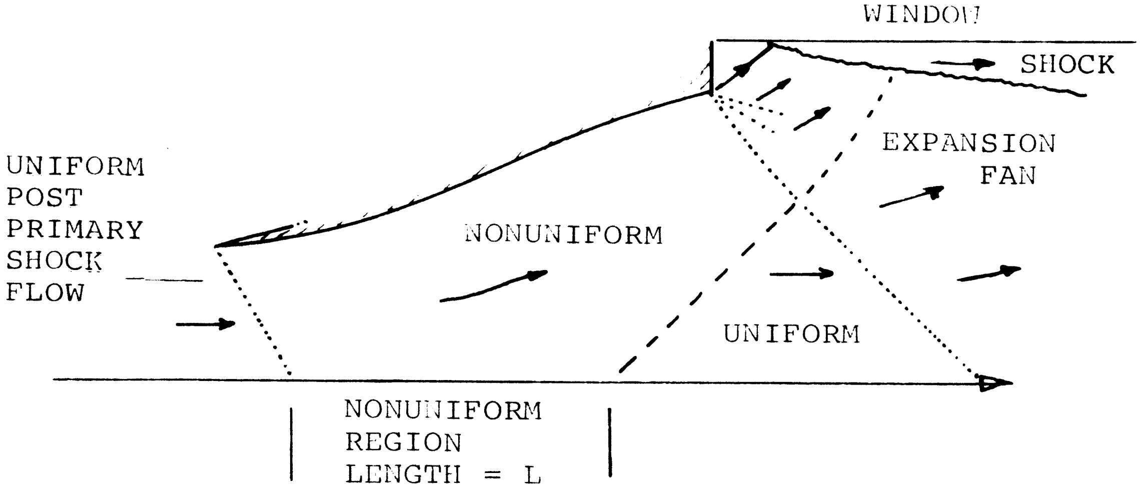

Fig. 3.8. Flow regions and features in the steady nozzle and test section flows. Length of uniform flow region on nozzle axis =8.95". Maximum diameter of the uniform region is 2". N.B. Diagram not to scale.

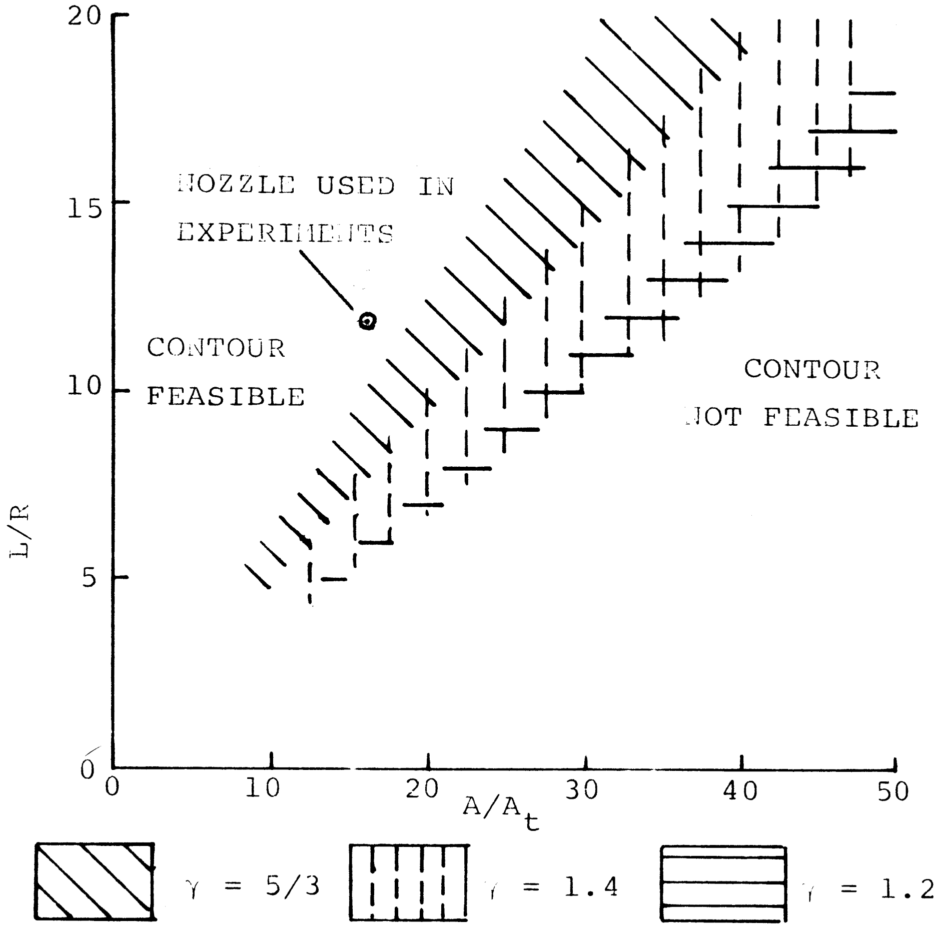

Fig. 3.9. Graph showing regions where nozzles are feasible on the (length of nonuniform region on the nozzle axis)/(inlet radius) vs. (nozzle area ratio) plane. Shaded regions indicate where nozzles are feasible for each γ.

uniform region as designed and the beginning of the expansion fan caused by the truncation of the nozzle.

3.4. SURVEY OF MINIMUM NOZZLE LENGTHS.

A survey was taken over a large range of input parameters to determine the minimum length of a nozzle shape for given inlet radius and given area ratio. The perfect gas nozzle design computer programme written by I. Shields was used for this survey. At each step in the calculation of the nozzle flow field, the programme checked whether the bicharacteristics had crossed. The crossing of two bicharacteristics in a flowfield calculation indicates the formation of a shock. The dimensions for a nozzle were to be taken to be feasible if and only if there were no crossings of bicharacteristics anywhere in the flow, i.e. only nozzles with shock-free flows were deemed to be acceptable. Fig. 3.9 shows the regions where nozzle shapes exist and where they do not exist on a graph of (length of nonuniform region on the nozzle axis)/(nozzle inlet radius) vs. (nozzle exit to throat area ratio) for three different values of the ratio of specific heats. The point representing the contoured nozzle used in the experiments is also shown in the graph and is well inside the region of feasible nozzle dimensions.

CONCLUSION.

The modified nozzle design programme has shown that the shape of the contoured nozzle required to produce a uniform test section flow is not significantly affected by the presence of chemical reactions in the flow. The small scatter of the nozzle shapes for the different shock speeds and the shock tube initial pressures indicates that a single nozzle shape will probably produce an acceptable test section flow for a range of shock conditions. The general insensitivity of nozzle shape to chemical reactions and to shock conditions may be taken to infer that the nozzle will produce a parallel shock free test section flow with the gases (air and argon) used in the nozzle flow experiments. When the experimental results are presented in Chapter 5, it will be shown that quite acceptable test section air and argon flows are produced by the nozzle.

CHAPTER 4: THE EXPERIMENTAL CONFIGURATIONS.

4.I. THE TUNNEL.

The free piston shock tube is the basic mechanism used in the Physics Department at the A.N.U. to produce high enthalpy gas flows. A diagram of the shock tube apparatus is shown in Fig. 4.1. Its principal of operation is that the driver gas, for the shock tube, is compressed and heated by a moving piston driven by high pressure air. Near the end of the piston compression stroke, a diaphragm, separating the driver gas in the comression tube from the test gas in the shock tube, bursts under the pressure of the driver gas. The driver gas then flows into the shock tube, pushing the test gas before it. The resulting strong compression wave in the test gas forms quickly into a shock wave which travels down the shock tube at nearly constant speed. The test gas processed by this shock then has well defined velocity and thermodynamic conditions. This shock wave is called the "primary shock wave" and the interface between the driver and test gases is known as the "contact surface". For a more detailed description of the free piston shock tube, and the operation of a reflected shock tunnel based on it, see Stalker (I966 and I967) and Stalker and Hornung (I97I).

As indicated earlier in this thesis, it is proposed that a hypersonic flow be produced by passing the post primary shock gas directly into a hypersonic nozzle placed at the downstream end of the shock tube. To facilitate the rapid attainment of a steady test gas flow in the nozzle, a prior steady flow (see Chapter 2, section 2.2) is established in the nozzle by the opening of a valve between the test section and an evacuated dump tank downstream of the test section. The valve is operated by the recoil of the reservoir compression tube and shock tube apparatus occasioned by the forward motion of the free piston. The valve, nozzle, etc., are shown in Fig. 4.2.

The test section-dump tank valve is a slide valve. Details of its design and operation are shown in Fig. 4.2.

The nozzle feed tank shown in Fig. 4.2. is designed to prevent significant reduction of the shock tube initial pressure due to the presence of the prior flow.

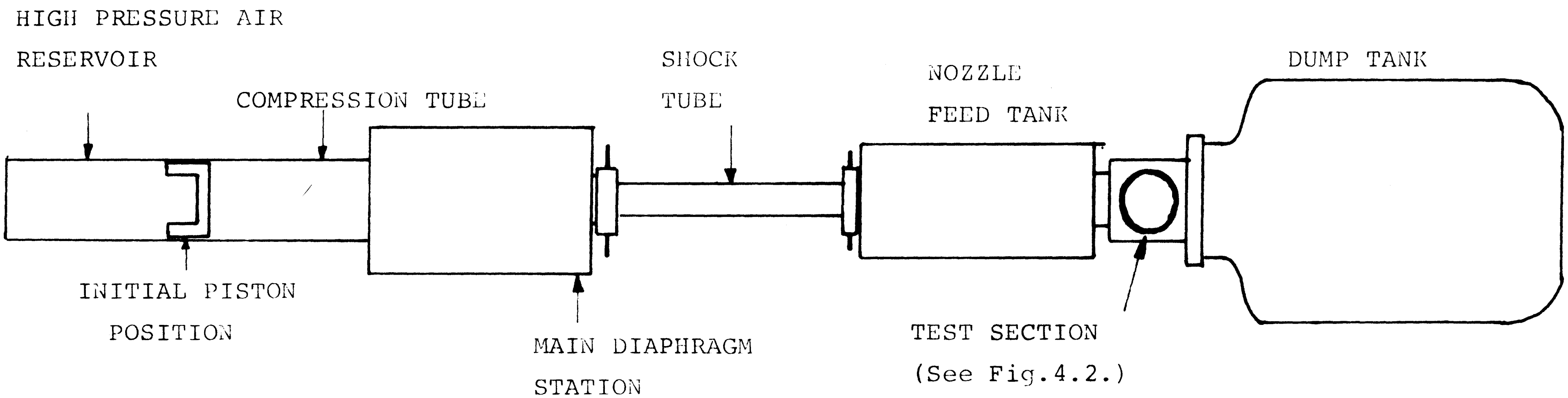

Fig.4.1. The complete shock tunnel apparatus
(not shown to scale).

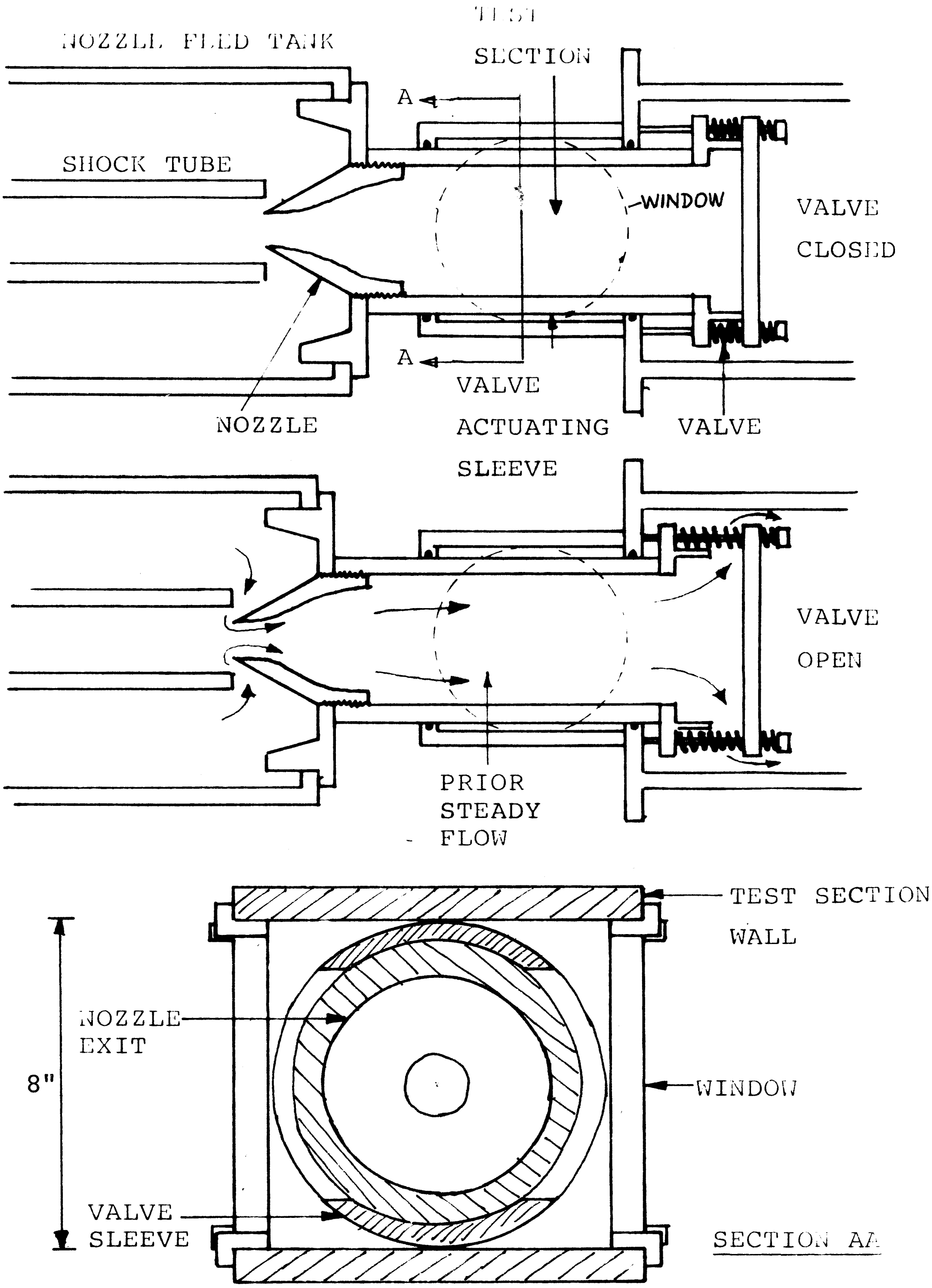

Fig.4.2. Operation of the valve producing the prior steady flow; the cross-section of the test section.

N.B. Diagram not to scale.

The hypersonic nozzle is axisymmetric and the leading edge of the nozzle is sharp. At its upstream end, the inner surface of the nozzle is parallel to the axis of symmetry of the nozzle (see Chapter 3. on the design of the nozzle). The outer and inner surfaces of the nozzle subtend an angle of 20° along the flow direction, at the nozzle leading edge. H.W. Liepmann and A. Roshko (I957) derive an expression which connects the angle of a two dimensional shock on a flat wedge with the angle of the wedge relative to the free stream flow, for a given Mach Number and ratio of specific heats, γ. If the wedge angle is increased from zero the shock remains attached to the wedge until a certain value of the wedge angle where it detaches from the wedge. The Mach Number behind the primary shock is approximately 3.5 for the air shots. For the argon shots it is generally greater than this. Liepmann and Roshko's equations show that, for a γ of I.4, the shock detachment angle is 37°. For a γ of 5/3 the detachment angle is 30°. The angle subtended in the flow by the nozzle entrance lip is therefore at least $I0^{\circ}$ too low to cause detachment of the oblique shock on the outside of the nozzle entrance. The presence of real gas effects and the fact that the nozzle entrance is axisymmetric, both lead to an increase in the body angle necessary to cause detachment. The detachment body angle is only a weak function of the free stream Mach Number. It can therefore be concluded that the shock on the outer surface of the nozzle entrance will be attached and, consequently, the flow internal to the nozzle will not be affected by the flow external to the nozzle.

4.2. GASES.

Air and argon were chosen as test gases for the evaluation of the shock tunnel performance. Interest in high stagnation enthalpy flows centres around body flows in which strong real gas effects are present (Hornung (I972), Hornung and Sandeman (I974). Air was chosen as a representative dissociating gas and argon was chosen as a representative ionising gas.

The observations made of the flows in the apparatus fall into two categories: flows in the tube and flows in the test section downstream of the nozzle.

4.3 SHOCK TUBE FLOWS

Measurements were made of the primary shock arrival time at several stations in the tube. At the first seven stations, the measurements were made with ionisation probes. These consisted of two wire electrodes with a potential difference between them. When the hot, dense post shock gas occupied the space between the electrodes, electrical breakdown occured in the gas and a current flowed between the electrodes. The rise of the current in the circuit containing the ionisation probe was monitored on an oscilloscope (CRO). The speed of the primary shock in this first section of the tube could then be calculated by measuring the probe positions in the tube and the times at which the current began to flow between the ionisation probe electrodes.

At the sixth and seventh stations, which were located in the final section of the tube, two Hewlett-Packard PIN photodiodes were used to monitor the luminosity coming from the flow. The circuit containing the photodiode and a diagram of the photodiode holder are shown in Fig. 4.3. The variations of current in these circuits were displayed on a CRO. Light coming from the gas in the tube was collimated by the diode holder so that the diameter of the base of the cone of acceptance of the diode was no more than 0.5cm. at the opposite side of the tube. This gave the system of the diode and associated circuitry a time resolution of approximately I μsec, with regard to primary shock arrival time.

The output from the two photodiodes was used for shock speed calculations between stations 6. and 7. It was found that the time difference between the rise of the ionisation probe at station 5. and the rise of the photodiode at station 6. was consistent with the time differences between the rises of like timing devices.

As well as being used for shock timing , the photodiodes provided a time history, at the photodiode stations, of the light output from the post primary shock gas, in a plane normal to the direction of travel of the shock. In general, the test gas temperature and ionisation levels are both a

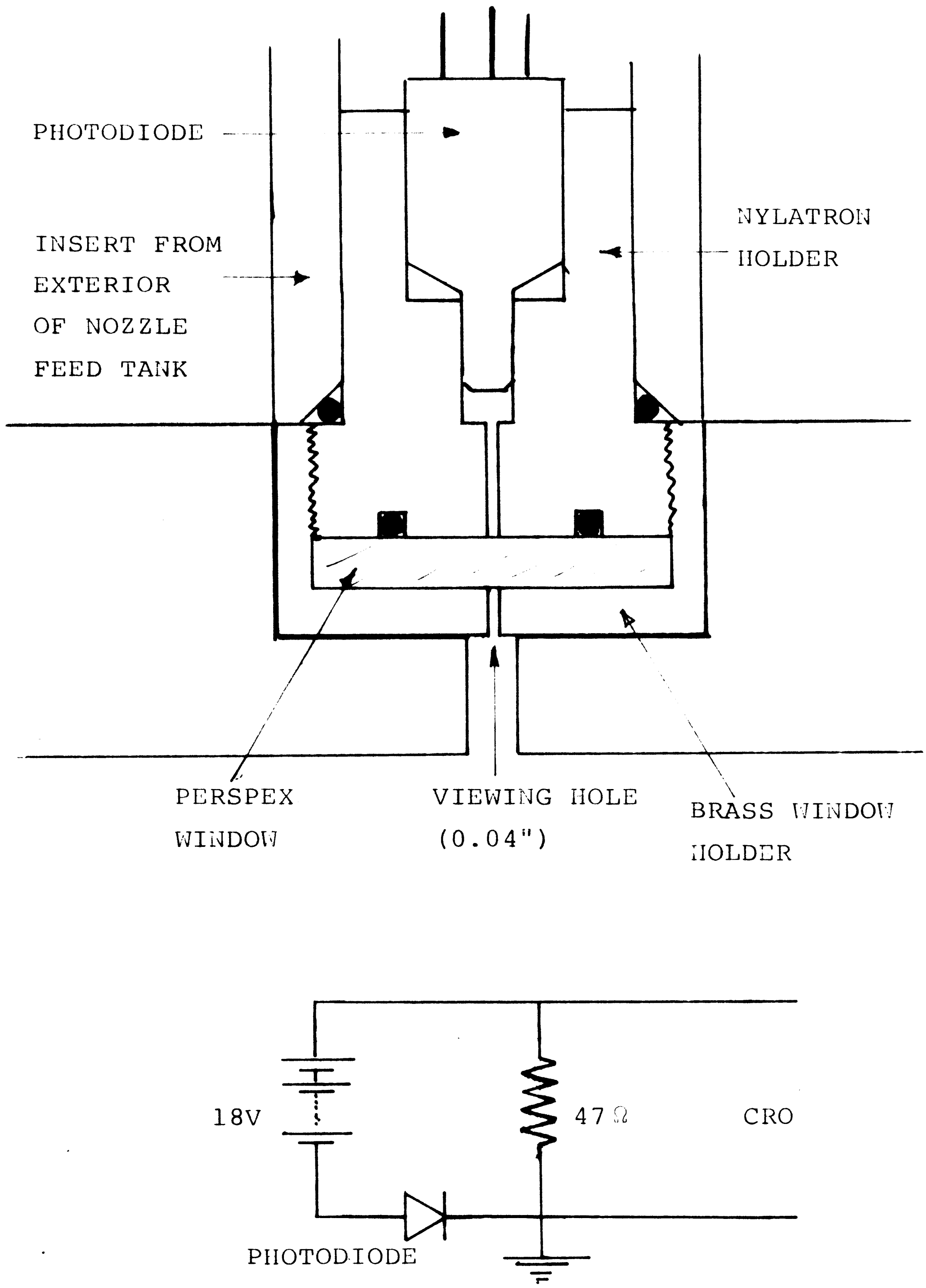

Fig. 4.3. Holder and circuitry for the photodiodes installed in the two final shock tube stations (24cm. and 116cm. from nozzle entrance).

The Image Converter Camera consists of an evacuated glass tube which has a photo-sensitive electron emitting screen at the up beam end and an electron sensitive photo-emitting screen at the down beam end. The second screen is identical to that used on a Cathode Ray Oscilloscope. The object image is focussed onto the photo-sensitive screen. The resulting electrons are focussed by a set of electron focussing grids inside the tube onto the electron-sensitive screen. The resulting light is then focussed onto the film. The image can thus be electronically shuttered and swept across the film by applying suitable electrical signals to the electron focussing grids. The Image Converter Camera used here was a TRW model 1D from TRW Instruments, 139 Illinois Street, El Segundo, California, U.S.A. and STL Products a division of Space Technology Laboratories Inc.

good deal higher than those of the driver gas. A consequence of this is that the test gas is more luminous than the driver gas which follows it. The luminosity history given by the photodiodes was, therefore, used to indicate the length of the test gas slug in the tube.

4.4. TEST SECTION FLOWS.

The Image Converter Camera (ICC) and the exploding wire light source are used in several different types of experiment. It is therefore worth discussing their operation separately from the descriptions of the experimental arrangements.

4.4.I. THE IMAGE CONVERTER CAMERA.

There are two common modes of operation of the camera: In the "sweep" mode, the image is swept continuously over a distance of 5 cm. on the film. The sweep of the image can be commenced by sending a suitable electrical pulse to the Image Converter Camera Delay Unit. The sweep is begun after a delay (0 to I00 μsec.) which is preset on the delay unit by the user. The sweep rate is also chosen by the user. Sweep rates of 4, I0, 20 and 40 μsec./(cm. swept on the film) were used in the experiments. Used in this mode, the camera provides a continuous record of events at the object viewed.

The other operation mode is the "framing" mode. Here, the image is recorded on the film at three separate times at three non-over-lapping areas of the film, the image being held still on the film while the exposure is made. The exposure time and the time intervals between exposures are set by the user.

By observing the monitor signal from the shutter electrode of the camera, it was found that the camera shutter opening and closing times were calibrated with the relevant dial settings on the camera.

The magnification factors from the test section to the negative were found by placing an object of known size in the test section region and photographing it. This procedure was carried out regularly and it was found that the factor did not alter appreciably from shot to shot during a set of experiments of the one type.

4.4.2. THE EXPLODING WIRE LIGHT SOURCE.

The light source for the absorption spectra and interferogramme experiments consists of a large capacitor ~~capacitator~~ in series with a double stranded twist of 9Ω/yard copper wire I cm. long and an ignitron (high current, small close time) switch. The capacitor was charged to 4.5kV and, at the appropriate time, the ignitron switch was closed electronically. The large current which subsequently passes through the copper wire strands causes them to explode producing a plasma composed largely of copper ions and electrons. The coupling of the magnetic field of the plasma and the presence of the leads between the charging unit and the capacitor introduce an inductive element into the circuit of the capacitor and wire. The light output from the exploding wire rises and falls in a periodic manner with the resulting underdamped discharge of the capacitor through the plasma. The period of the oscillation of the light output is approximately 30 μsec., which implies that the period of oscillation of the currents is approximately 60 μsec. The light from the exploding wire takes about 5 μsec., from the time of the switching of the ignitron, to reach a level which is usable. The light intensity in the peaks of the oscillation drops below the usable level after about I50 μsec. This length of time is quite sufficient for our purposes.

4.4.3. EMISSION SPECTRA FROM THE SHOCK LAYER ON A CYLINDER.

The primary aim of ~~the~~ these experiments was to discover the time of arrival of the test gas and the time of arrival of the driver gas at a nozzle station by observing the appearance and disappearance of the emission spectra of these gases or gas mixtures at that station. A secondary aim was to discover what species (if any) were present in the flow as contaminants.

A cylinder I.25" diameter and length I.5" was placed in the test section on the flow centre line. The leading edge of the cylinder was I2.5 cm. downstream of the nozzle end (see Chapter 3. for nozzle dimensions) and was perpendicular to the flow direction. A spectrograph, shown in Fig. 4.4, was set up outside the test section to view the light emitted by the gas in the shock layer on the cylinder. The spectrograph viewed the shocked gas along a line parallel to the leading edge of the cylinder and approximately 0.05 cm. upstream of the leading edge. The column viewed was less than 0.I cm. in diameter. The spectrally resolved image of the gas column was recorded on Polaroid film (3000 ASA) by the

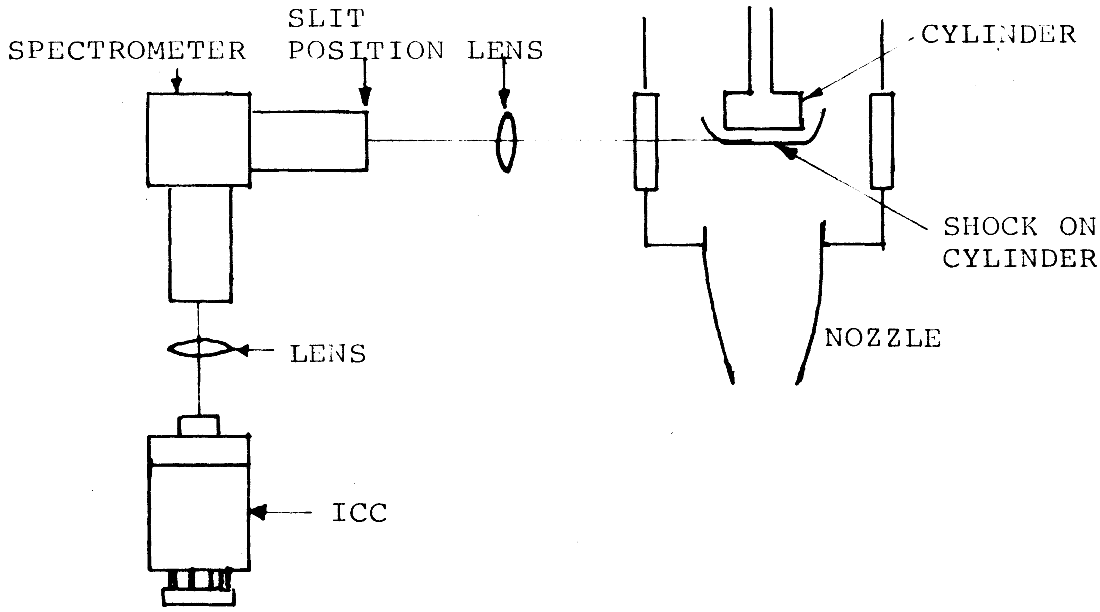

Fig.4.4. Spectrograph for emission and absorption experiments on gas in shock layer on cylinder (view from above).

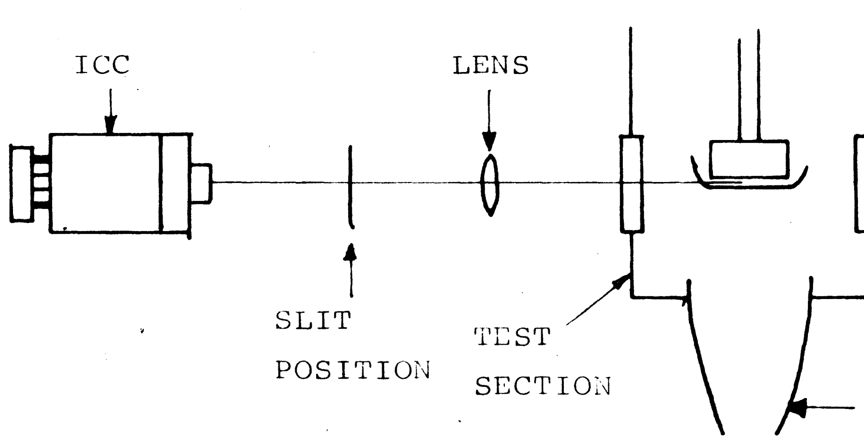

Fig. 4.5. Apparatus for cylinder shock layer luminosity streak photographs.

The distance over which the image was swept on the negative was, in general, 2 cm or more on the negative.

Image Converter Camera. The camera swept the image across the film (sweep mode), as the gas flow passed over the cylinder, producing a record of the emission spectrum as a function of time. The height of the image, in the direction of the time sweep, was only about 2% of the total (5 cm.) sweep distance on the film.

Correspondence of light wavelength with distance on the film, perpendicular to the distance of the sweep, was determined by the superposition of the image of the spectral lines from a Hg - Ca - Zn gas discharge lamp. The wavelength range observed by the camera was 4000 to 5800 Å.

The rise of the ionisation probe at station 5 triggered a CRO which sent a pulse to the Image Converter Camera Delay Unit after a time delay set on the CRO. The delay unit then opened the camera. The required time delay was too great to use the delay unit alone.

At the same time the camera recorded the spectrally resolved image of a portion of the shock layer gas, a Hewlett - Packard PIN photodiode with associated circuitry the same as those mounted in the shock tube (see Fig. 4.3), monitored the (integrated) luminosity of the gas from the opposite side of the test section. This monitoring was designed as a check on the primary shock and contact surface arrival times.

4.4.4. ABSORPTION SPECTRA FROM THE SHOCK LAYER ON A CYLINDER.

The atomic and molecular species detected in the flow by the experiments just described are those having a high proportion of their members in electronically excited states. In an attempt to sample the species with high proportions of their members in the electronic ground state, a set of absorption experiments was performed.

In these experiments, high intensity light from the exploding wire light source, was passed through the shock layer on the cylinder and the transmitted beam was detected by the spectrograph. The cylinder resided in the same place as for the last experiments. The spectrograph configuration was left unchanged except that the lens apertures on the camera were reduced and the Polaroid film was replaced with Ilford HP4 film. The final record on the film was, then, transmitted intensity at each wavelength vs. time.

The idea behind the performance of these experiments was that each species in the flow could then be identified by the presence of their characteristic absorption spectra. Otherwise, the aim of these experiments was the same as for the emission experiments.

4.4.5. STANDOFF DISTANCE OF FLOW ON A CYLINDER.

In these experiments, a record was made of the extent and luminosity distribution of the shock layer on the cylinder, described above, as a function of time. The aim of performing the experiments was to discover the arrival times of the primary shock and the contact surface at a station in the nozzle. It was hoped, also, that some assessment could be made of the steadiness of a blunt body flow in the tunnel.

The nozzle station and orientation of the cylinder remained unchanged from the previous experiments. A lens was placed to one side of the cylinder. The image of the cylinder and flow, thus formed, was masked off at the image plane, so that only a narrow, horizontal section of the body and flow could be seen by the Image Converter Camera on the other side of the image plane (see diagram Fig. 4.5). The section viewed was that including the stagnation streamlines in the shock layer, and extended approximately 0.05 cm. (in the test section) above and below these streamlines. The Image Converter Camera was operated in the streak mode and the light emitted from the shock layer was recorded on a diagram of (distance along the nozzle) vs. (time elapsed since the beginning of the streak).

4.4.6. INTERFEROMETRY - INTRODUCTION.

A Mach - Zehnder interferometer was used to obtain a quantitive measure of the changes in refractivity of the gas flow in the test section as the flow proceeded.

A diagram of the interferometer, the light source, the test section and Hasselblad camera, and the Image Converter Camera, is shown on Fig. 4.6. The optical filter between the interferometer and the Hasselblad camera passes only a narrow band of frequencies, specifically 5330 ± 40 Å. The presence of the filter allows observation of the higher order fringes which would be obscured by the overlap of the interference patterns of other frequencies, were all the frequencies to be passed.

A schematic diagram for the triggering circuitry used

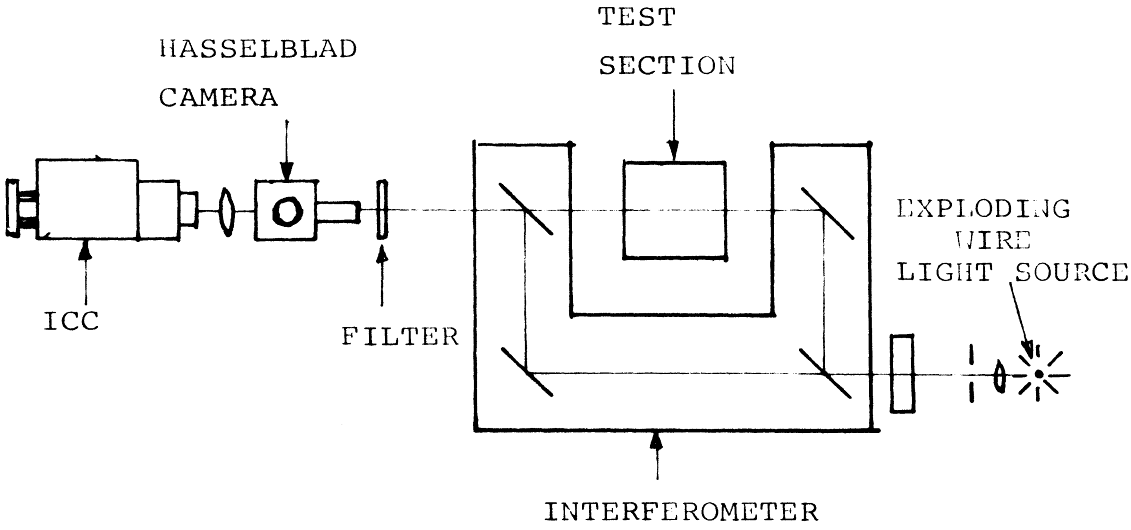

Fig. 4.6. Apparatus for interferometry experiments. The slit for the swept interferogrammes resides in the downbeam end of the Hasselblad camera.

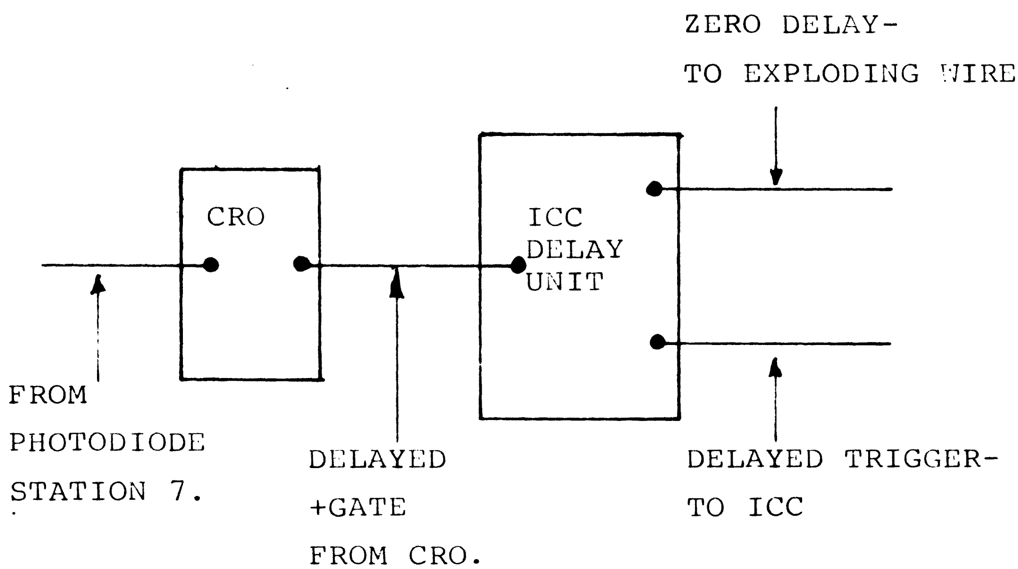

Fig. 4.7. Exploding wire and ICC triggering arrangements for the interferometer experiments.

in the interferometer experiments, for the image Converter Camera and the exploding wire is shown in Fig. 4.7. The rise of the photodiode at station 7. triggers a CRO which, after a preset delay, triggers the Image Converter Camera Delay Unit. The exploding wire was triggered off the "Zero Delay" +gate outlet on the delay unit. The camera itself was triggered off the "Delayed" +gate outlet. The delay from the firing of the exploding wire to the opening of the camera shutter was set on the Delay Unit and was, in general, of 7 μsec. duration to allow the light output from the wire explosion to rise to a usable level.

Three different types of interferogrammes were taken of the interference pattern produced by the apparatus:

4.4.7. HORIZONTAL SLIT INTERFEROGRAMMES:

For these experiments the cylinder was removed from the test section. The image of the interference pattern and test section, formed at the image plane of the Hasselblad camera, was masked so that only a narrow (0.5 cm. in the test section) horizontal section of the flow was visible to the Image Converter Camera . This section included the axis of symmetry of the nozzle and extended from 7 to 23 cm. downstream of the nozzle end. These limits were imposed by the upstream edge of the test section window and the width of the interferometer beam. The interferometer was adjusted so that the interference fringes were vertical and distributed across the field of view. The Image Converter Camera, in the sweep mode, recorded the time evolution of the interference pattern as the primary shock, secondary shock, steady test flow and the contact surface passed through the test section. The direction of the sweep on the film was perpendicular to the image of the slit on the flim.

Analysis of the interferogrammes thus produced, yielded the trajectories of the pressure (density) disturbances and (in some cases) the trajectory of the contact surface in the test section. The steadiness and divergence or convergence of the "steady" test gas nozzle flow could be assessed from the interferogrammes along with the magnitude of the refractivity changes between the gas ahead of the primary shock and that behind the primary shock.

4.4.8. VERTICAL SLIT INTERFEROGRAMMES.

Here, again, the image at the rear of the Hasselblad camera was partly masked and there were no models in the nozzle flow. This time, a narrow (0.5 cm. in the test section) vertical section of the test flow was viewed by the Image Converter Camera. The section viewed was 16.8 cm. downstream of the nozzle end and was of height I2 cm. The section included the lower half of the flow and approximately 1/3 of the upper half of the flow. The interferometer was adjusted so that the interference fringes were horizontal for this series of shots. The Image Converter Camera was, again, operated in the sweep mode. The sweep direction was perpendicular to the slit image on the film. The camera thus recorded the distribution of the interference fringes (and therefore refractivity), across the nozzle flow, as a function of time.

The object of taking the vertical slit interferorammes was to discover whether the flowfield was spatially one dimensional (i.e. whether the flow was uniform in properties in a plane perpendicular to the flow direction).

4.4.9. FRAMING PHOTOGRAPHS OF BODY FLOWS.

For these body flow experiments, all masking was removed from the rear of the Hasselblad camera. The Image Converter Camera was converted to operate in the framing mode. The flows photographed were those over a 35° half angle, 4" wide double wedge and, later, those over a sharp nosed flat plate at 5° incidence. These bodies were placed in the flow at the nozzle station which had been observed during the vertical slit experiments (16.8 cm. downstream of the nozzle end).

The idea of doing these experiments was to see if a steady flow could develop over a body such as a wedge, in the time for which the steady nozzle flow lasted. This was to be done by comparing "still" photographs of the body flows taken at different times during the nozzle flow. It had been shown, by the blunt body shock layer luminosity photographs, discussed above, that the flow on a cylinder, in most cases, did not have sufficient time to become steady. The steady flow establishment time on a wedge was expected to be a good deal shorter than that for a cylinder.

4.4.10. STAGNATION PRESSURE MEASUREMENT.

Bar gauges were employed to measure the stagnation pressure of the test gas flow. These gauges were developed and manufactured at the University of Wales by H. Edwards.* A diagram of the construction of the gauges is shown in Fig. 4.8. Basically, a bar gauge consists of a X-cut piezo-electric quartz crystal section sandwiched between an earthed front bar (usually duralium) and a massive backing bar (usually of lead).

The principal of operation of the gauge is that the history of the pressure on the front face of the gauge is translated into a longitudinal stress wave in the front bar. This wave travels along the front bar and through the piezo-electric crystal which sets up a corresponding potential difference between the front bar and the backing bar. By connecting a CRO betwen the backing bar and the gauge casing (earth) the trace of the potential difference can be recorded and the pressure history on the front face deduced. The signal from the gauge ceases to be useful when the stress wave, reflected off the rear of the backing bar, returns to the piezo-electric crystal.

The bar gauge has the following properties which make it most suitable for taking pressure measurements in the non-reflected shock tunnel flows:

(i) short rise time - approximately 1 μsec. for the gauges used here.

(ii) earthed front bar insulates the crystal from ionised flows.

(iii) good signal levels - in the range of 10 to 100mV at the flow conditions of interest.

(iv) the usable signal time of 150 μsec. from the first pulse is ample for the short flow durations in the nonreflected tunnel.

The signals from the gauges were fed straight into the input connection of a CRO. The CRO sweep was initiated, after a preset time delay, by the rise of the photodiode at station 7.

Calibration of the output signal vs. applied pressure was carried out (at least for pressures up to 1 atmosphere or so) on a small shock tube. The shock speeds in this tube were such that no real gas effects were present. Shock waves

*private communications. See Davies L. and Lippiatt J. (1964) for a description of a similar gauge and its use.

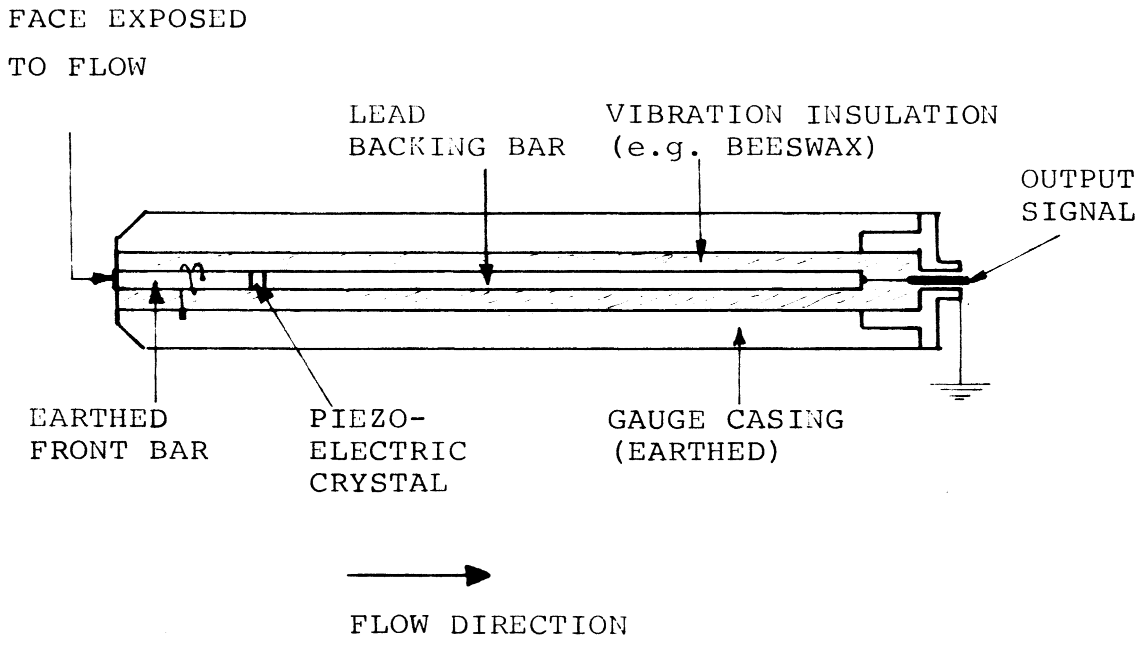

Fig. 4.8. Diagram of bar gauges (not to scale). Diameter of gauge is 1/2" .

were fired at the gauges and the pressures for reflected shock, and steady post shock flow over the gauge, were graphed against the signals from the gauges. The times for establishment of a steady flow over the gauges were calculated using the theory developed by L. Davies and J. Lippiatt (1964). Unfortunately, the bar gauges were found to be unreliable. In some cases, the calibration runs performed prior to the tunnel experiments failed to produce a unique, repeatable calibration curve. In all cases, the tunnel conditions proved to be too severe for the gauges and no gauge could be recalibrated. The output obtained from the bar gauges in the tunnel flows therefore had to be discarded. At the time of writing, a more robust generation of gauges, produced by H. Edwards and modified at the A.N.U., is being calibrated and tested in the tunnel flows by R.J.Stalker.

CHAPTER 5. RESULTS AND DISCUSSION.

5.1. SHOCK SPEEDS AND INITIAL PRESSURES.

The curves of shock speed vs. shock tube initial pressure for the two test gases, air and argon, over the five initial shock tube pressures, from 2"Hg to 1/8"Hg, are shown in Fig. 5.1. The driver conditions used to produce these shocks were, initially, 510 p.s.i. (gauge) of air in the reservoir and 14.9"Hg (abs.) of He in the compression tube. The diaphragm was of 10 G. mild steel and had a burst pressure of 6700 p.s.i. The resulting compression ratio (λ) in the compression tube was 60.

5.2. DURATION OF TUBE FLOW.

The time for which the test gas flow can exist in the test section of the nonreflected shock tunnel is limited by the time for which the test gas flow exists at the nozzle entrance. The test gas flow time in the shock tube was measured at a station 24 cm. upstream of the nozzle entrance by a Hewlett-Packard PIN photodiode. The photodiode and associated circuitry have been described in section 4.3 of Chapter 4.

A CRO trace of the signal which resulted from the passage of a test gas slug past the photodiode at station 7 is shown in Fig. 5.2. The sharp rise at the beginning of the signal is due to the arrival of the primary shock. The arrival of the He driver gas causes the decline in the trace height. The slow decline of the signal may be attributed to mixing at the contact surface and to the test gas in the boundary layer on the walls of the shock tube. The trace was not always steady in the section of the trace corresponding to the presence of the test gas opposite the photodiode. Argon shots produced a rough trace in a higher proportion of shots than did air shots. These fluctuations cannot be attributed to gross non-uniformities in the tube flows of test gas. Such non-uniformities would have been observed in the steady test section flows and were not (see section 5.5.3 in this chapter for presentation and discussion of test section density measurements). It is possible that they were due to a turbulence in the wall boundary layer or to flow effects in the hole through which the photodiode observed the flow.

The flow time for the test gas was taken to be the time

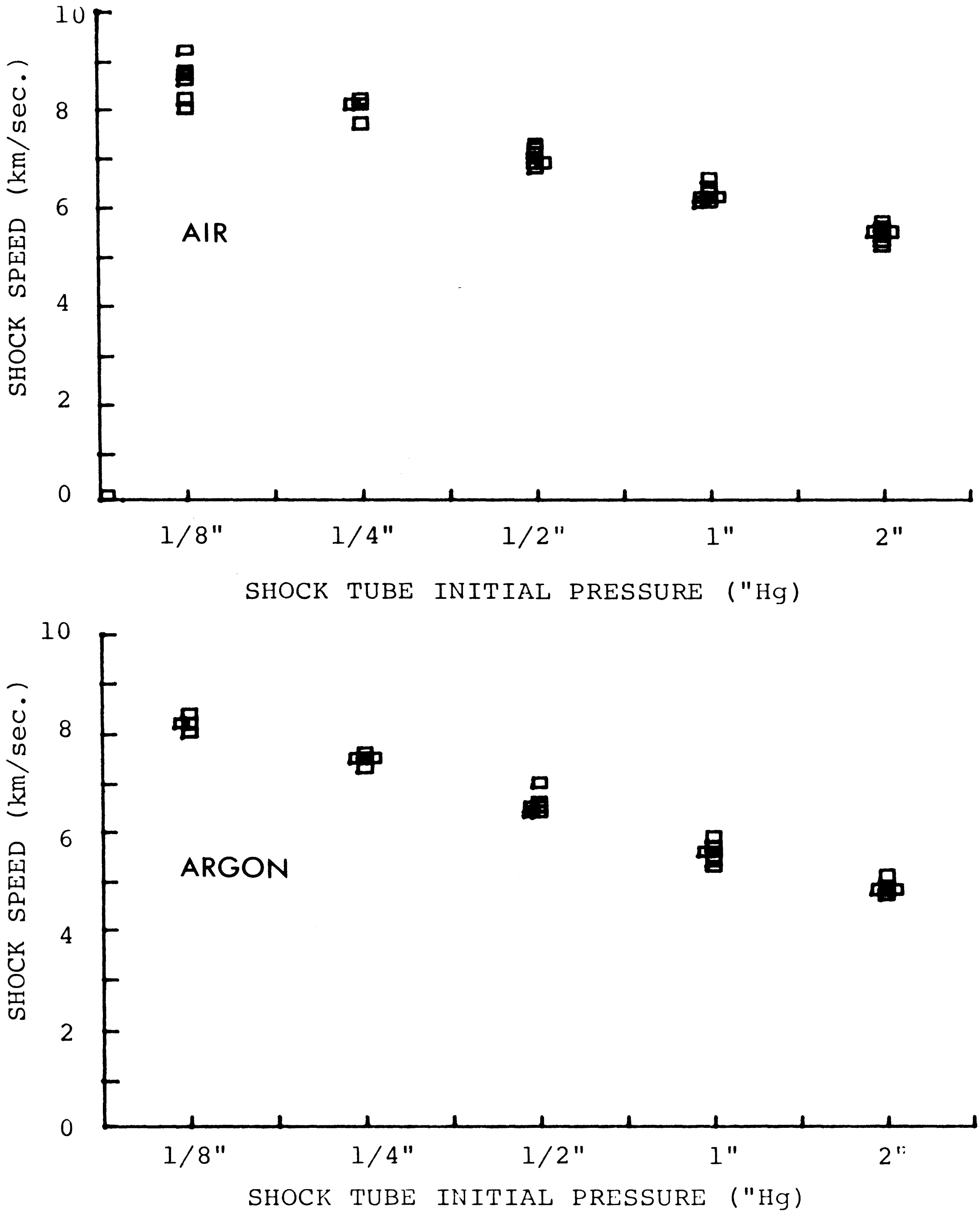

Fig. 5.1. Shock tube performance curves. Shock speed vs. initial shock tube pressure for air and argon as test gases.

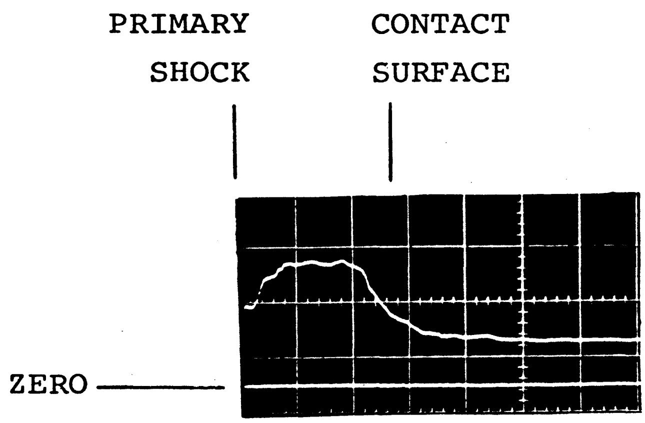

Fig. 5.2. CRO trace of the signal from a photodiode monitoring test gas luminosity in the shock tube.
Photodiode is in station 7.
The shot number is 2602. The interferogramme taken in the course of this shot is shown in Fig. 5.7. The shock conditions are 1/2"Hg. air initially in the shock tube and a shock speed of 0.723 cm/μsec.
Sweep speed on the trace is 10μsec/large division.
Sensitivity on the vertical scale is 0.005 V/large div.

between the rise of the signal from the photodiode and the time at which it fell to a level half way between its maximum value and the final plateau level. The results of these measurements for a large number of shots, in both air and argon, are shown in Figure 5.3.

The measured test flow times in the tube are very much less than those for an ideal shock tube, i.e. one in which the contact surface acts as a loss-free piston driving the test gas. If we take a mean density ratio of 10 across the shock, the test times, for an ideal shock tube, at a station 820 cm. from the main diaphragm (station 7), should be 100 μsec for the 1/8"Hg condition and 160 μsec for the 2"Hg condition, assuming the same shock speeds as experimentally observed.

H. Mirels (1963 and 1964) attributes the less than ideal test times in real shock tubes to a loss of mass from the test gas slug through the boundary layer on the shock tube walls. In his model of the growth of the test gas slug, a maximum slug length, l_m, is reached. This occurs when the mass flux across the shock equals the mass flux, in the boundary layer, passing the contact surface in shock fixed co-ordinates. The contact surface outside the boundary layer is, of course, stationary in shock fixed co-ordinates when the test gas slug has ceased to grow in length. By equating the two mass fluxes, Mirels derives an expression for l_m:

$$\left(\frac{p_{st}}{p_\infty}\right)^n \frac{l_m^{1-n}}{d} = \frac{1}{4\beta}\left(\frac{p_\infty}{p_{e,o}}\frac{W}{W-1}\right)^{1-n} M_s^n\left(\frac{\rho a}{\mu}\right)^n_{st} \qquad \ldots(5.2\text{-}1)$$

where p = pressure, d = shock tube diameter,
$W = u_w/u_{e,o}$, u = flow speed, M_s = shock Mach Number,
ρ = density, a = equals sound speed, μ = coefficient of viscosity.
n = 1/2 for laminar and 1/5 for turbulent boundary layer.
<u>subscripts</u>: st = a standard condition, w = condition at the wall
∞ = initial shock tube condition, e = post shock value in flow outside the boundary layer, o = immediately behind the shock before conditions are modified by the presence of the boundary layer (N.B. I have taken this immediately after the region of chemical non-equilibrium behind the shock, believing this to be more representative of the gas conditions in which the boundary layer grows than the frozen cond-

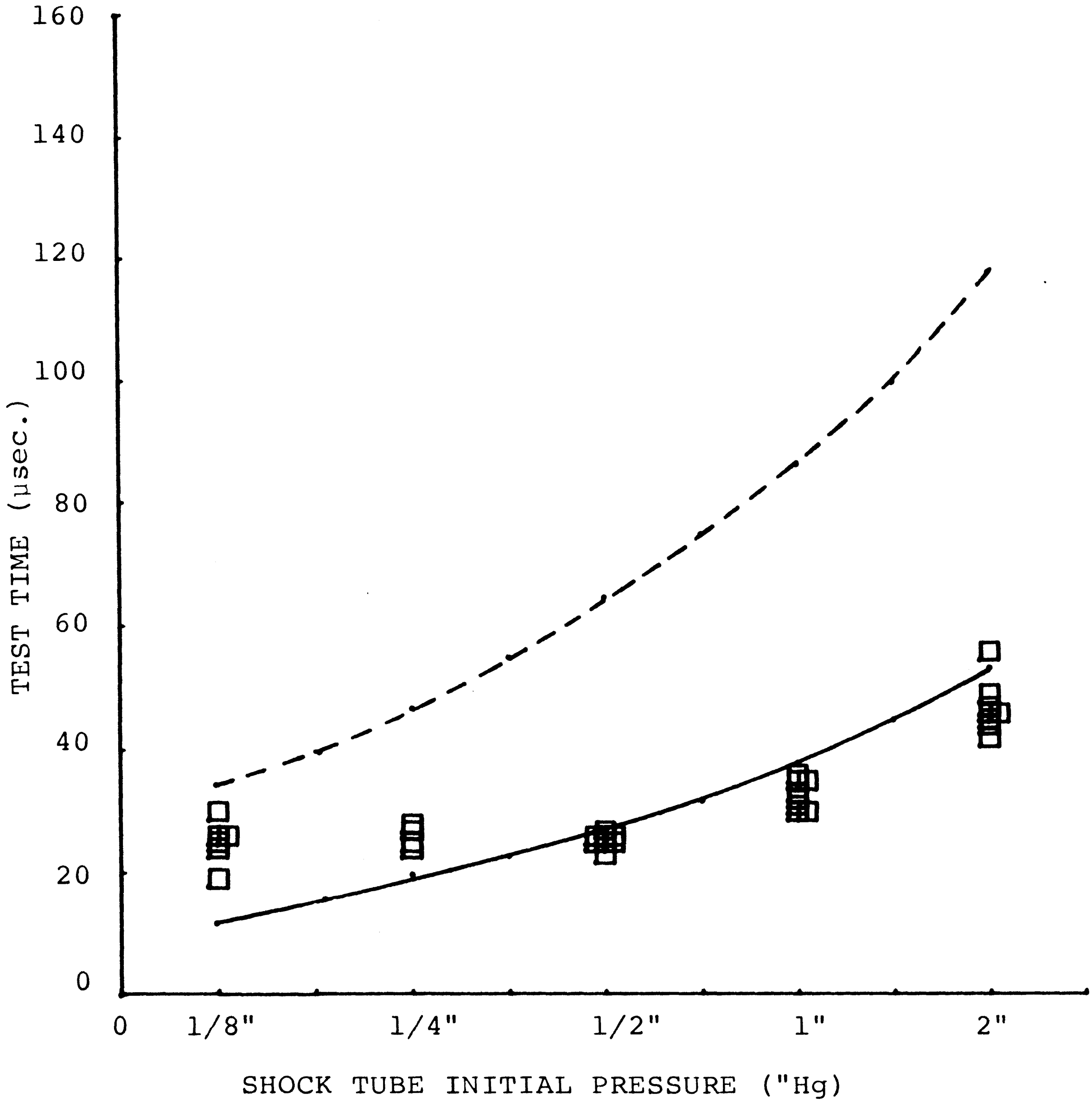

Fig. 5.3. Test times in the shock tube - AIR SHOTS.

______ Theory for turbulent boundary layer.

- - - Theory for laminar boundary layer.

□ Experiments

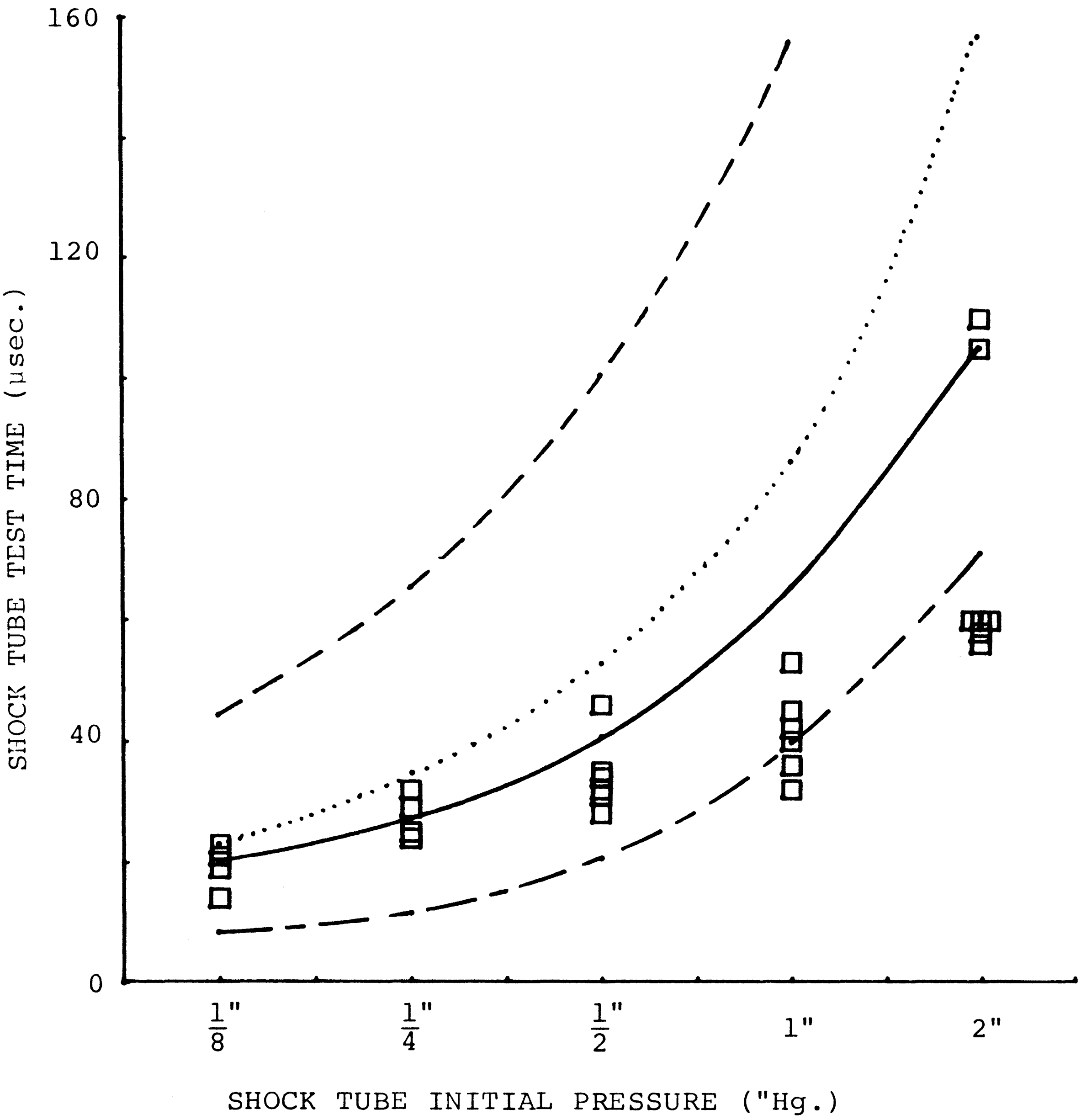

Fig. 5.3.(Cont.) Test times in the shock tube - ARGON SHOTS.

——— Theory for turbulent boundary layer with no plasma decay.

— – — Theory for turbulent boundary layer with decayed plasma.

– – – – Theory for laminar b.l. - no decay.

.... Theory for laminar b.l. - decayed plasma.

□ Experiments.

itions behind the shock). Mirels gives a set of standard conditions: $T_{st} = 522^{o}K$ $\rho_{st} = 1$ atm. $\left(\frac{\rho a}{\mu}\right)_{st} = 6.93\times10^{6}ft^{-1}$ for air and $7.39\times10^{6}ft^{-1}$ for argon.

The quantity β, appearing in equation (5.3-1), is found from consideration of the boundary layer growth rate and the difference between the mass fluxes mentioned above. A first approximation to β is found by assuming the free stream for the boundary layer (i.e. the post shock conditions) is uniform between the shock and the contact surface. The second approximation to β makes allowance for free stream variations due to the increase of the boundary layer mass flow with increasing distance from the shock. The expression for β is then simplified and approximated by combinations of polynomials in W. The results of these approximations are, for a turbulent boundary layer:

$$\beta \simeq \left(\frac{W^2 + 1.25W - 0.8}{W\ (W-1)}\right)^{4/5} \cdot \frac{p_\infty}{p_{e,o}} \frac{W}{(W-1)} \cdot K_o \quad ..(5.2\text{-}2)$$

$$\text{where } K_o = 0.0575 \frac{\delta^*/\delta}{1-W}\left[\frac{1-W}{\theta^*/\delta}\right]^{\frac{4}{5}}(W-1)^{\frac{9}{5}}\left(\frac{\mu_m\rho_w}{\mu_w\rho_{e,o}}\left(\frac{\rho_m}{\rho_{e,o}}\right)^3\right)^{\frac{1}{5}} \quad ...(5.2\text{-}3)$$

$$\frac{\delta^*/\delta}{1-W} = \begin{cases} 0.157 \text{ for air} \\ 0.176 \text{ for argon} \end{cases}$$

$$\frac{\theta^*/\delta}{1-W} = \begin{cases} \dfrac{W+7/3}{80/3} & \text{for air} \\ \dfrac{W+2}{24} & \text{for argon} \end{cases}$$

$$\left(\frac{\mu_m\rho_w}{\mu_w\rho_{e,o}}\left(\frac{\rho_w}{\rho_{e,o}}\right)^3\right)^{1/5} \simeq \left(\left(\frac{h_m}{h_{e,o}}\frac{T_{e,o}}{T_\infty}\right)^{0.76}\frac{T_{e,o}}{T_w}\left(\frac{h_{e,o}}{h_m}\right)^3\right)^{1/5}$$

h_m is a mean specific enthalpy defined by

$$\frac{h_m}{h_{e,o}} \equiv 0.5\left(\frac{h_r}{h_{e,o}} + 1\right) + 0.22\left(\frac{h_r}{h_{e,o}} - 1\right)$$

$$\simeq 0.5\left(\frac{T_w}{T_{e,o}} + 1\right) + 0.22\left(\frac{W-1}{W+1}\, r(o)\right)$$

h_r = recovery enthalpy, h_w = wall enthalpy
$r(o)$ = (Prandtl Number)$^{1/3}$ = 0.897 for $\gamma = 1.4$ and 0.875 for $\gamma = 5/3$.

For a laminar boundary layer :

$$\beta \simeq C_{e,o}^{0.37}\; 1.135 \left(\frac{2(W-1)}{1 + 1.022W}\right)^{1/2}\left(1 + \frac{1.328 + 0.890W}{ZW - 1}\right) \quad ..(5.2\text{-}4)$$

where $$C_{e,o}^{0.37} = \left(\frac{\rho_e \mu_e}{\rho_w \mu_w}\right) \simeq \frac{T_w}{T_{e,o}}\left(\frac{T_{e,o}}{T_w}\right)^{0.76}$$

The Power Law for viscosity, $\left(\frac{\mu}{\mu_{st}}\right) = \left(\frac{T}{T_{st}}\right)^{0.76}$, was used in the above equations. The Sutherland Viscosity Law was also tried but this made little difference to the final results.

The question now arises as to whether the boundary layer is turbulent or laminar for the conditions of interest. Mirels suggests that the nature of the boundary layer is determined by the Reynolds Number based on maximum test gas slug length, l_m:

$$R_{em} = u_{e,o}(W - 1)^2\, l_m / \nu_{e,o}$$

where ν = kinematic viscosity.

The value of this number is shown as a function of shock Mach Number for the experimental conditions in Fig 5.4.

Also shown on this graph is the region where, according to Mirels, transition between a turbulent and laminar boundary can be expected to occur, up to a shock Mach Number of 9. The Mach Numbers of the shocks of interest are all higher than 9, so the relevant transition Reynolds Number is uncertain. Calculations of slug length were therefore made for both turbulent and laminar boundary ~~areas~~ layers.

Calculations of l_m from the equations (5.2-1,2,3) requires the specification of the post shock test gas pressure, density and temperature. For the air shots, these quantities were obtained directly from the equilibrium normal shock computer programme, ESTC. After the region of chemical nonequilibrium behind a shock in air, the gas conditions should remain reasonably constant, except for those changes occuring due to the growing boundary layer. The argon post shock test gas, however, has strong gas property gradients due to enthalpy loss through radiation (see section 5.5.6 in this chapter, for a description of these losses and their effects). For each argon shot, several slug length calculations were made using a representative sample of the post shock test gas conditions as free streams for the wall boundary layer. It seems reasonable to expect that the actual slug length will lie somewhere inside the range of slug lengths produced by these calculations.

Having obtained the maximum slug length, l_m, the growth rate of the boundary layer must be considered in order to determine what percentage of l_m has been attained by the test gas slug at a particular nozzle station (e.g. station7). Mirels has carried out this analysis and presents graphs of both $\bar{\tau} = u_w \tau / l_m$ and $T = l/l_m$ vs. $X = x_s / W l_m$ where τ is the test time and l the slug length at station x_s, u_w is the shock speed or, in shock fixed coordinates, the wall speed.

The measured and calculated test times at photodiode station 7 are presented for the shocks in air and argon in Fig. 5.3. The inference drawn from this comparison of theory and experiment is that the wall boundary layer is turbulent for the conditions with high initial pressures, and that at low initial pressures there is a transition towards a laminar boundary layer. This is in accordance with the decrease occuring in Reynolds Number, R_{em}, with a decrease in shock tube initial pressure seen in Fig. 5.4. Mirels theories

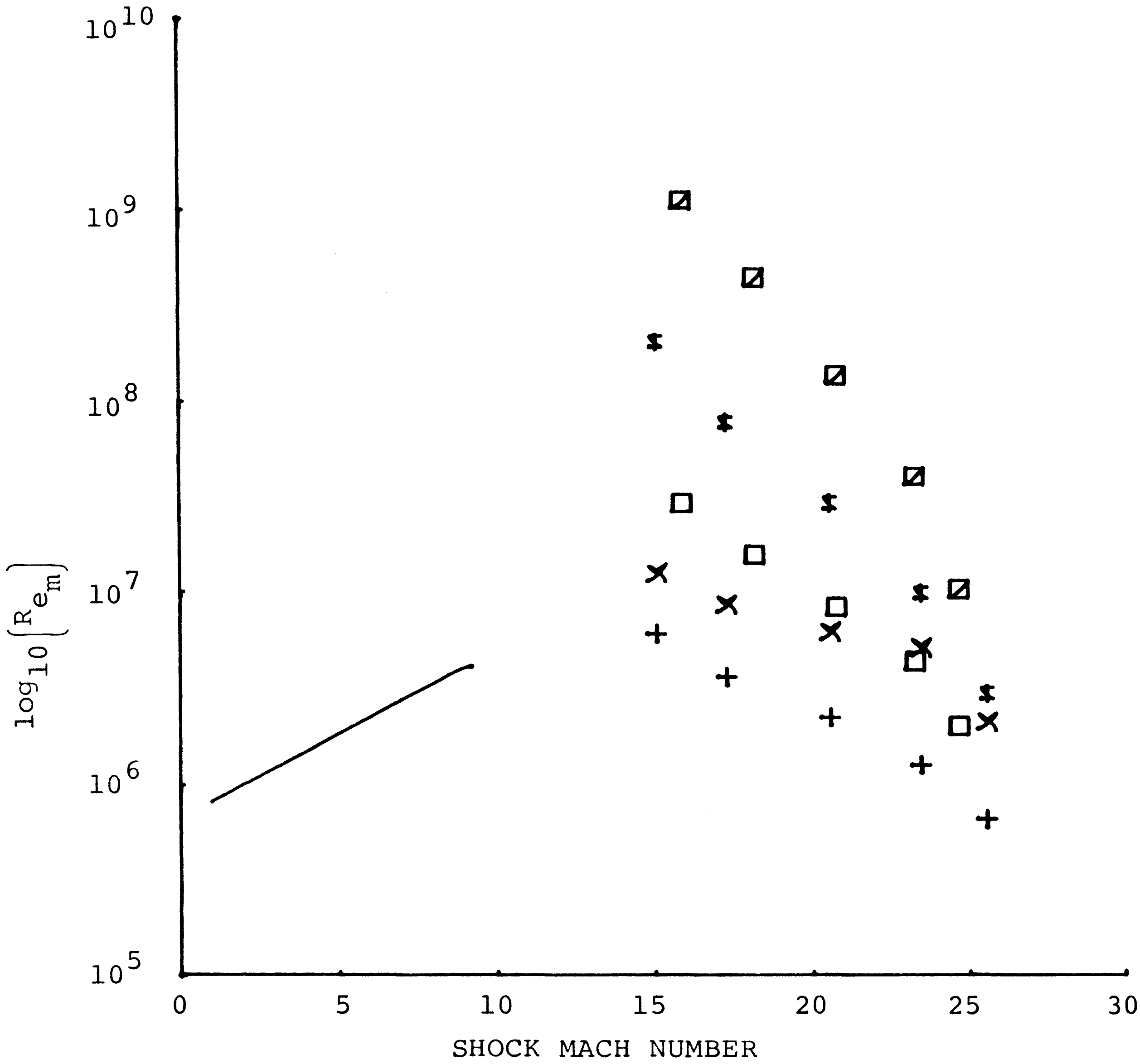

Fig. 5.4. Log_{10} of Reynolds Number based on the maximum test gas slug length vs. shock Mach Number.

□ Air (turbulent b.l.), ⊠ Air (laminar b.l.)

+ Argon (turbulent b.l. - no plasma decay)

× Argon (turbulent b.l. - decayed plasma)

⧗ Argon (laminar b.l. - no plasma decay)

——— Transition Reynolds Number .

Decayed plasmas are approximately half way between the primary shock and the contact surface taking the measured test times.

The papers of Hornung (1972) and Hornung and Sandeman (1974) provide a basis for estimates of the expected bow shock stand-off distance for the steady chemically reacting flow over a circular cylinder. For the purposes of the following approximate calculation air and argon will be assumed to behave like nitrogen with regard to bow shock stand-off distances.

Hornung (1972) presents a plot of the ratio of the density immediately behind a bow shock to the free stream density, ρ_s/ρ_∞, for a nitrogen flow in T3 in the reflected mode against the non-dimensional kinetic energy of the free stream, $\mu \equiv Wu_\infty^2/2R\theta_d$, where W = molecular weight of N_2, u_∞ = free stream flow speed, R = universal gas constant, θ_d = characteristic dissociation temperature for N_2. His measured values of ρ_s/ρ_∞ lie between 4 and 6 over a range of μ from 0.45 to 1.14. The values of μ for the air flows considered here lie within this range and, if W and θ_d are replaced by the molecular weight and characteristic ionisation temperature for argon, then the values of μ for argon also lie within this range. An average density ratio of 5 will therefore be used for the following calculations.

Hornung correlates for spheres and circular cylinders, the product of the normalised stand-off distance, and the density ratio across the shock, $\frac{1}{2}(\frac{\Delta}{a})(\frac{\rho_s}{\rho_\infty})$ with a reaction rate parameter, $\Omega \equiv (\frac{d\alpha}{dt_s})\frac{a}{u_\infty}$ where $\frac{d\alpha}{dt_s}$ = rate of change of the N_2 dissociation fraction immediately behind the shock, Δ = shock stand-off distance a = body radius. The values of $\frac{1}{2}(\frac{\Delta}{a})(\frac{\rho_s}{\rho_\infty})$ for a sphere and a circular cylinder at the limits of a frozen (Ω=0) and equilibrium (Ω=∞) flow are given in the following table with the corresponding values of $(\frac{\Delta}{a})$ for $\frac{\rho_s}{\rho_\infty} = 5$.

	CIRCULAR CYLINDER		SPHERE	
	$\frac{1}{2}(\frac{\Delta}{a})(\frac{\rho_s}{\rho_\infty})$	$(\frac{\Delta}{a})$	$\frac{1}{2}(\frac{\Delta}{a})(\frac{\rho_s}{\rho_\infty})$	$(\frac{\Delta}{a})$
FROZEN CHEMISTRY	1.16	0.46	0.39	0.16
EQUILIBRIUM CHEMISTRY	0.58	0.23	0.20	0.08

The stand-off distances are shown above the photographs in Fig. 5.5.

Hornung and Sandeman (1974) measured a stand-off distance of $\frac{\Delta}{a} = 0.4 \pm 0.03$ over a range of argon flows over long circular cylinders. The densities in their flows were, in general, an order of magnitude lower and the flow speeds 30% lower than those of the flows considered here. This stand-off distance is also shown above the argon flow photograph in Fig. 5.5.

It can be seen from Fig. 5.5 that for 20 μsec in the 1"Hg air shot and for 8 μsec in the ½" Hg argon shot before the contact surface arrival the bow shock stand-off distance remains reasonably steady. Also, the stand-off distances of the shocks lie within the range for flow over a sphere but outside the range for flow over a circular cylinder. This result is not surprising as the cylinder length (1.5") is only 20% greater than the cylinder diameter (1.25"). The flow behaviour would therefore be expected to be similar to that for a sphere having a similar diameter as gas loss at the cylinder ends would be significant.

In fact the luminosity seen on the photographs to the right of the cylinder leading edge would seem to be due to spillage of part of the shock layer at the cylinder ends. A consistent feature of the luminosity photographs of the bow shock is the sharp drop in luminosity

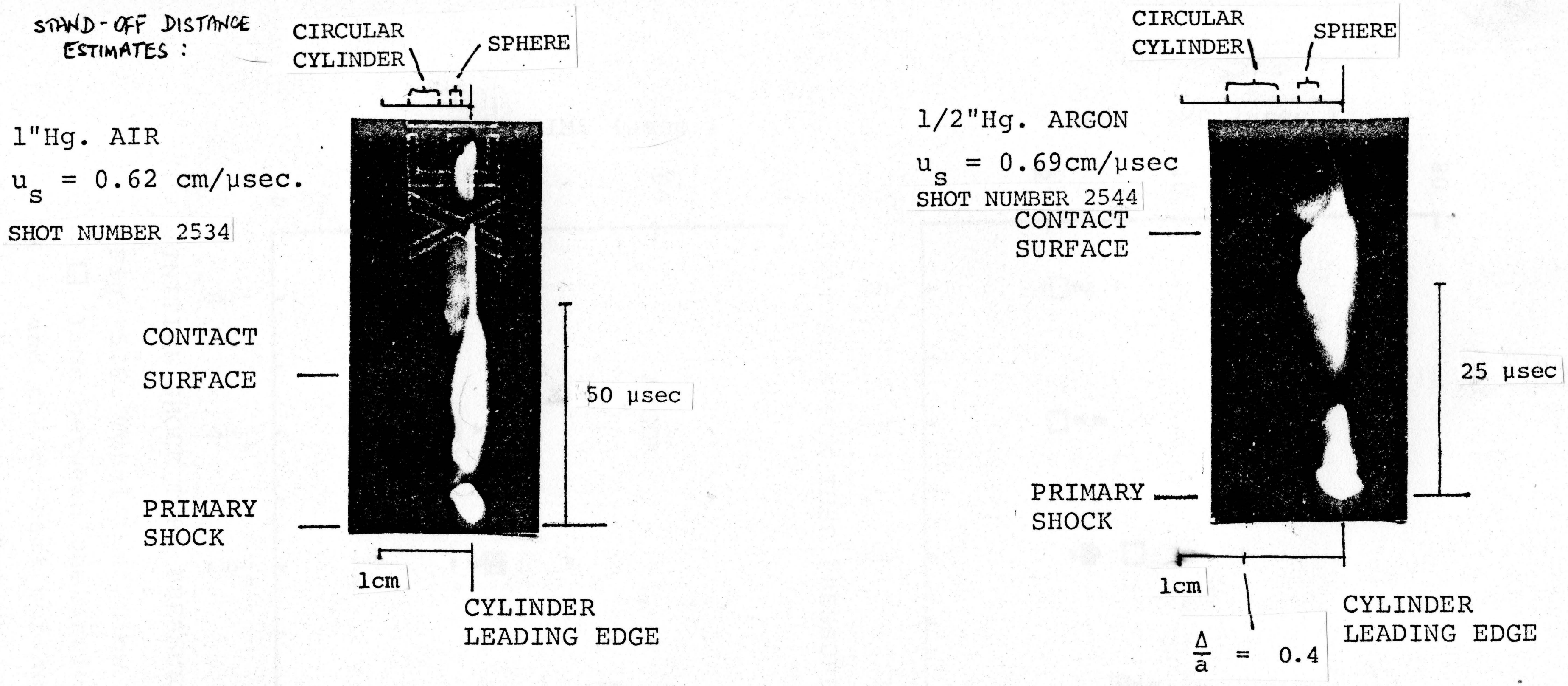

Fig. 5.5. Photographs of the shock layer on the cylinder. The image of the shock is swept in time in the vertical direction.

u_s is the primary shock speed in the tube. The flow direction is from left to right.

of the shock layer soon after the arrival of the primary shock and the rise of the luminosity a short time later. During this period of low shock layer luminosity, the bow shock cannot be seen on the positives. An examination of the negatives, where the shock is faintly visible, shows that the "dark spot" coincides with a rapid rise and fall in the shock stand-off distance. In all cases, the maximum stand-off distance achieved during this period is approximately twice that in the period immediately prior to the arrival of the contact surface, i.e. the "steady" period. Comparison of Figs. 5.5 and 5.8 shows that the increase in stand-off distance and the simultaneous drop in shock layer luminosity begin upon the arrival of the secondary shock at the cylinder.

A possible explanation for these phenomena is as follows. The primary and secondary shock speeds in the test section can be measured from the horizontal slit interferogrammes. The average of the two shock speeds can be taken as a measure of the flow speed of the gas contained between the two shocks. In all cases, there is little difference between this flow speed and the steady expansion flow speed predicted by NFAPC. The flow speed of the gas following the secondary shock can be expected to be slightly higher than the steady flow value as it has passed through a non-steady expansion. However, the density in the starting shock system is approximately three times that of the flow following the secondary shock (see Fig. 5.13). The value of ρu^2 between the shocks can therefore be expected to be two or three times that of the flow following the secondary shock.

The pressure established in the bow shock between the arrival of the primary and secondary shocks is therefore higher than the value appropriate for a steady bow shock flow with the gas following the secondary shock as free stream. The arrival of the secondary shock at the bow shock should therefore lead to a transient increase in the stand-off distance. Following this increase, the stand-off distance should decrease towards the steady value for the new free stream conditions.

The drop in the shock layer luminosity after the secondary shock arrival may then be largely attributed to the expansion of the gas already in the shock layer. However, at least during the time that the stand-off distance was increasing, one would expect that gas entering the shock would be as luminous as that in the "steady" flow prior to the contact surface arrival. The free stream conditions are approximately the same and the bow shock is strong in both cases. The reason that this gas does not produce a strong impression on the film may be that this new gas layer is thin and that the bow shock is not straight along the line of sight during the transient increase in stand-off distance. Consideration of the path taken by the contact surface through the shock layer indicates that, during this time, the newly shocked gas may occupy only 20 or 30% of the shock layer at the time of maximum stand-off. The negatives do indicate that the shock is probably not straight during this time.

appear to provide a satisfactory explanation of the observed test time in a shock tube up to a Mach Number of 25 in both air and argon test gases.

A parameter of interest, computed during the course of the test time calculations, is the percentage of the maximum test time realised in the tube. If the boundary layer is turbulent, (e.g. the 2"Hg and 1"Hg shots in both gases) then the test time is 80% or 90% of the maximum possible. On the other hand, where the boundary layer is laminar, (e.g. the 1/8"Hg condition), Mirels theories indicate that only half of the maximum possible test time has been achieved in the tube at station 7. Unfortunately, little or nothing can be done to improve this figure; doubling the shock tube length would only increase the test time for these low initial pressures by about 10%. A 50% increase in shock tube diameter would double the test time, but would reduce the performance of the shock tube apparatus.

5.3. PRESSURE DISTURBANCES IN THE TEST SECTION FLOWS.

In Chapter 2 the theories for the test gas nozzle flow starting and finishing processes were presented. The first task in examining the test section flows must be to check that these theories do, in fact, describe the nonsteady flow processes occuring in the nozzle. The checks made included identification of the contact surface and the various pressure disturbances in the flow, measurement of their trajectories in the test section and comparison of these trajectories with the theories. The main sources of information for the checks were the blunt body shock layer luminosity experiments, described in Chapter 4 (sections 4.4.7 and 4.4.8).

Records of the shock layer on the cylinder are shown in Fig. 5.5 with notes which point out the important features of the flow. The highly luminous flow on the cylinder was taken to be the test gas flow. The less luminous flow, which followed, was taken to be the driver gas flow.

On all photographs there was a sharply defined boundary, the contact surface, between the two flows. If variation of pressure between the shock and the stagnation point on the body is linear with distance, then a gas particle entering the shock will follow a parabolic trajectory in that region. The contact surface can be seen to follow such a trajectory after entering the shock.

The time difference between the arrival of the primary shock and the arrival of the contact surface at the cylinder station in the test section was measured from the cylinder flow records for shots where there was a prior steady flow. The results of these measurements are shown in Fig. 5.6. These results should be compared with the shock tube test times shown in Fig. 5.3. In most cases, the test section test flow time is approximately equal to the shock tube test flow time. It will be shown later (section 5.5.3 in this chapter) that approximately 45% of the test section test gas flow time is a usable test flow, the first 55% being the non-steady nozzle starting flow.

Horizontal and vertical slit interferogrammes were taken for air and argon shots with initial shock tube pressures between 2"Hg and 1/8"Hg with the prior steady flow valve operating (VO). Shots with the valve not operating (VNO) were taken for air with initial shock tube pressures of 1/4"Hg and 1/8"Hg. Shown in Fig. 5.7 are a horizon tal and a vertical slit interferogramme taken for flows where a prior steady flow (PSF) exists ahead of the primary shock. Also shown is a horizontal slit interferogramme for a flow where no PSF exists. The marked difference between test gas flows with and without a PSF is immediately evident from these photographs.

The flows where a PSF exists will be considered first in interpreting the flow features seen on the interferogrammes. The earliest disturbance, a compression, is, undoubtedly, the primary shock. Its time of arrival at the station where the cylinder resided for the cylinder flow shots, coincides with the times at which the test flows began on the cylinder.

Also, from the cylinder flow experiments, we have a measure of the time of arrival of the contact surface at the cylinder. These measurements indicate that the contact surface arrives in the test section well after the second clearly seen disturbance on the interferogrammes. The direction and size of the fringe shift across this second disturbance, and its position in relation to the primary shock and the contact surface, imply that it is the secondary shock.

In some of the interferogrammes a travelling disturbance in the fringe pattern could be seen where the contact surface

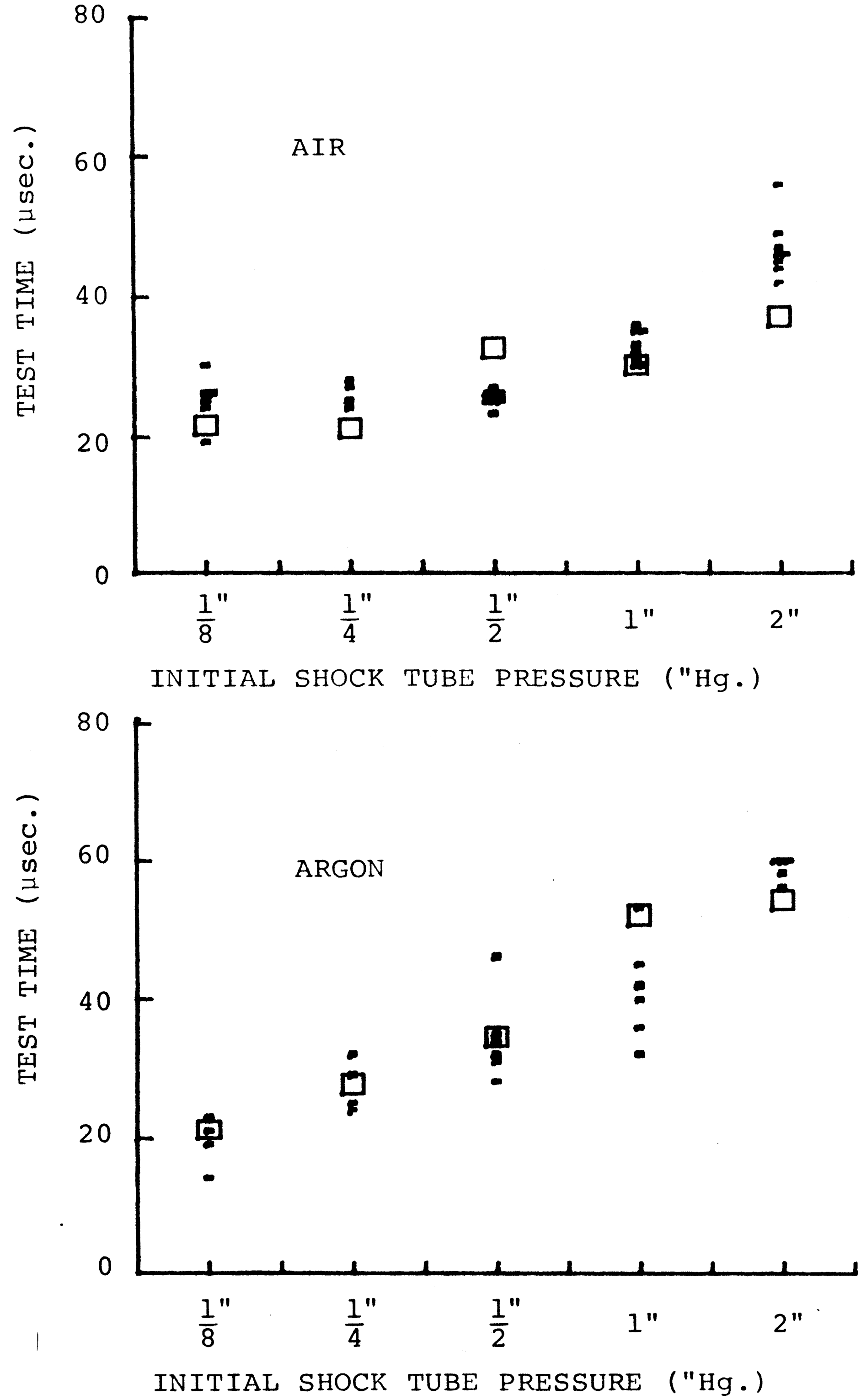

Fig. 5.6. Total test flow time in the test section.

□ Time between the arrival of the primary shock and the contact surface measured from the shock layer on a cylinder with prior steady flow.

▪ The test flow time in the shock tube.

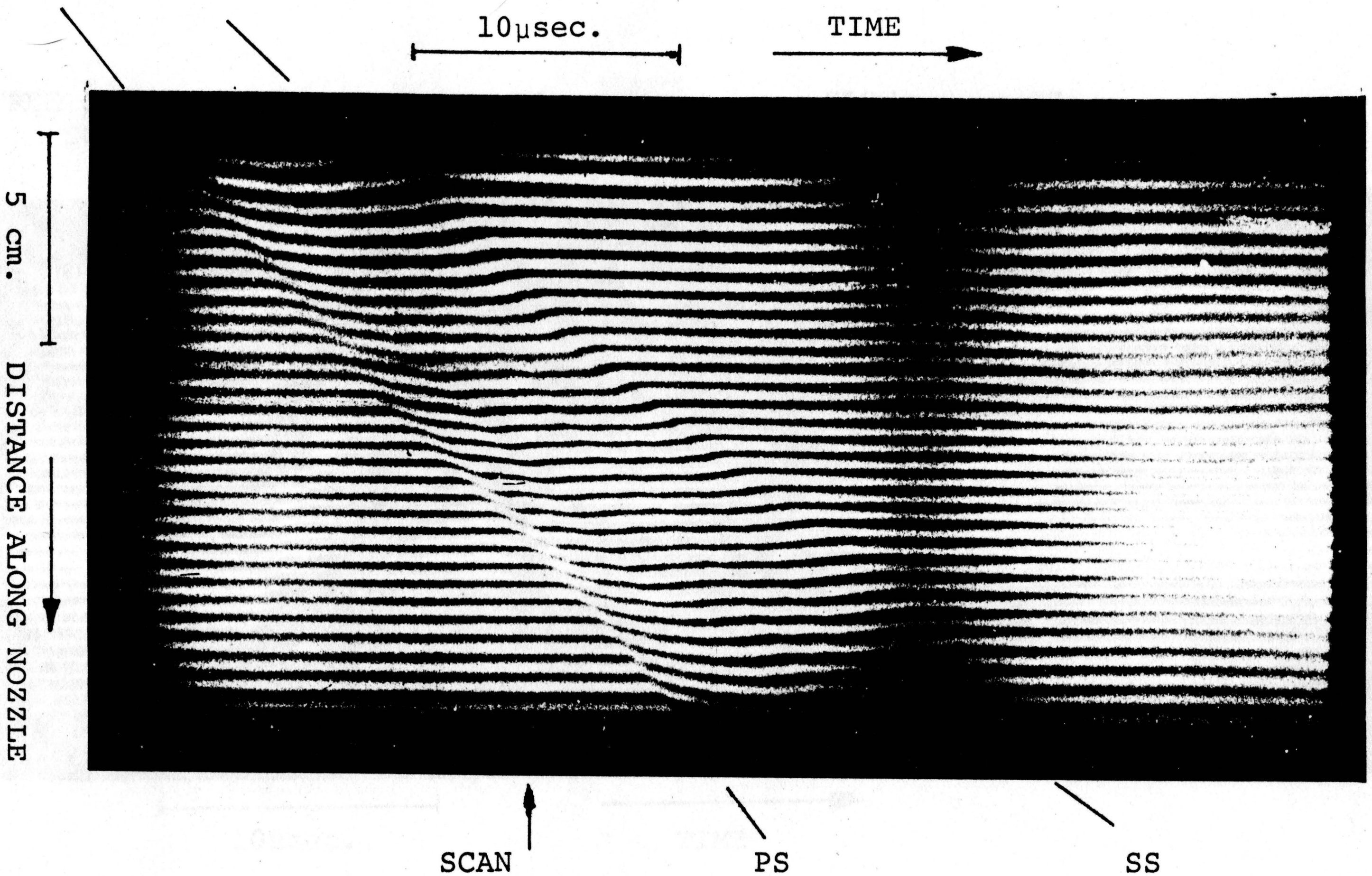

Fig. 5.7. A horizontal slit interferogramme. Initial shock tube pressure = 1/2"Hg.air Shock speed = 0.7 cm/μsec. Shot is with a prior steady flow. Primary shock (PS), Secondary shock (SS) and the position for the scan in Fig.5.12. are marked.

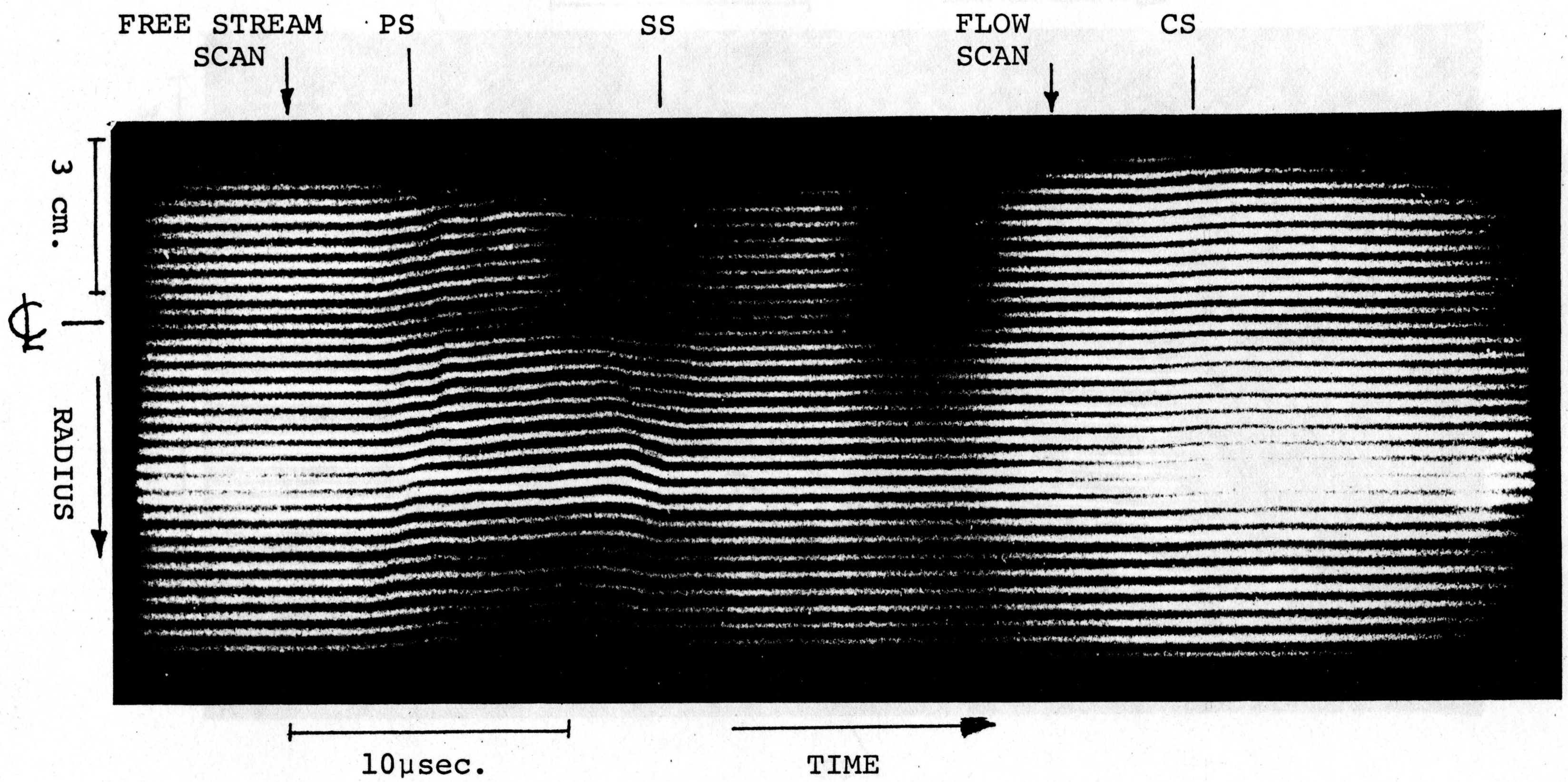

Fig. 5.7. A vertical slit interferogramme. Initial shock tube pressure = 1/2"Hg. air Shock speed = 0.72 cm/μsec. Shot is with prior steady flow. Primary shock (PS), secondary shock (SS), the contact surface disturbance (CS) (unusually apparent on this interferogramme) and the positions of the free stream and flow scans for the fringe shift pattern shown in Fig. 5.14. are marked.

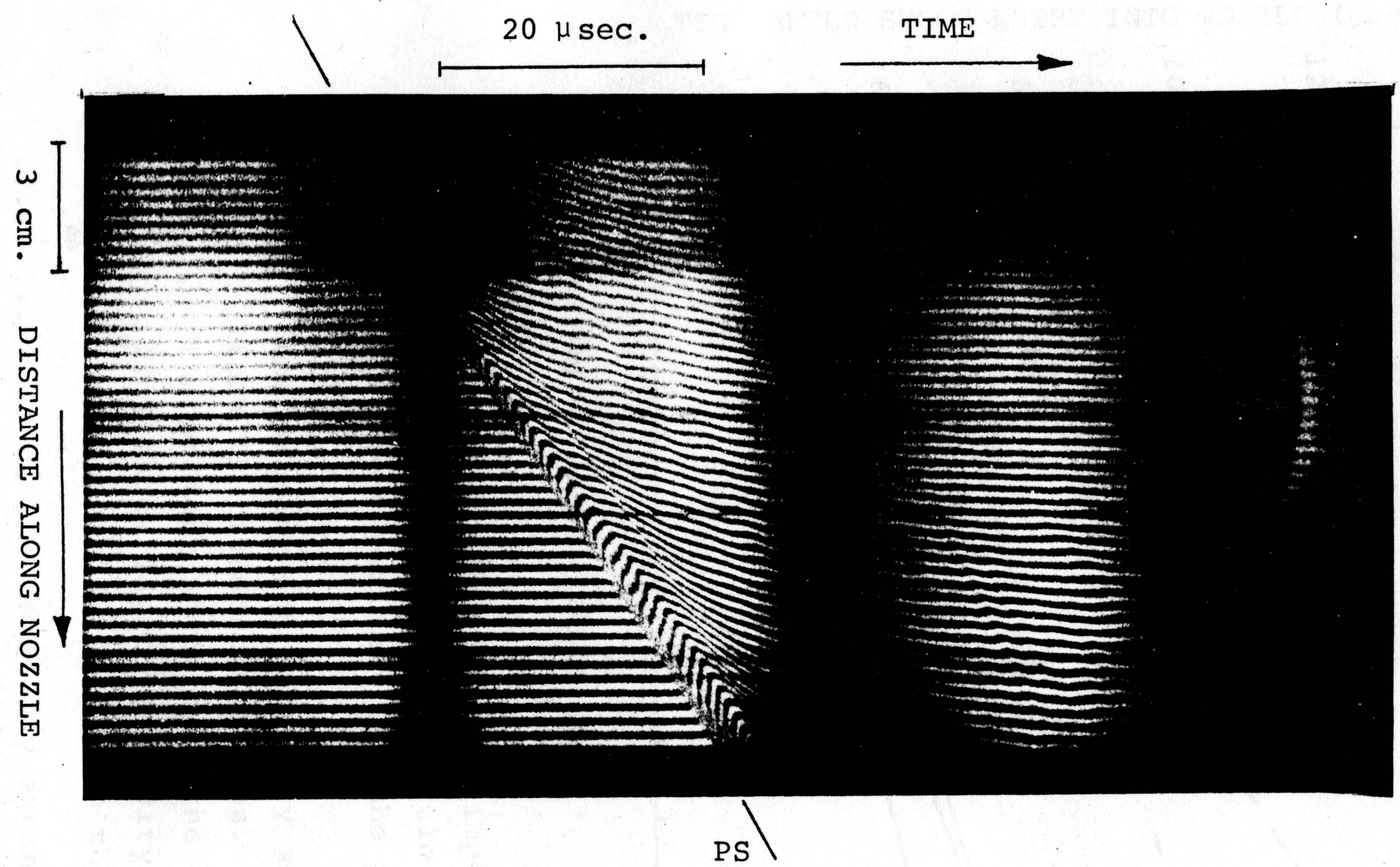

Fig. 5.7. A horizontal slit interferogramme with no prior steady flow. Shock tube initial pressure = 1/2"Hg. air. Shock speed = 0.732 cm/μsec. The primary shock (PS) is marked.

was expected, but in others there was no significant fringe shift across this region. The lack of any large disturbance in the fringe pattern around the contact surface supports the conclusion, reached in Chapter 2, that there is no strong disturbance created by the entry of the contact surface into the nozzle and the mismatch between the driver and test gases.

The other important flow feature, the head of the non-steady expansion wave could not be identified on the interferogrammes.

The region between the secondary shock and the contact surface is expected to contain the steady test flow. In a later section of this chapter (section 5.5) the steadiness and uniformity of the flow in this region will be investigated and the refractivity compared to that expected from the steady nozzle flow calculations made with NFAPC.

In the case of the flow with no PSF, the primary shock is considerably delayed in its passage through the test section. The gross disturbances to the flow caused by this delay are clearly seen in the interferogramme (Fig. 5.7). Consideration of the results of the cylinder flow experiments show that these disturbances have moved upstream of the contact surface. Therefore, no steady test gas flow exists for the case where no PSF exists. Other notable features of the flows with no PSF are the large fringe shift across the primary shock and the absence of a clearly defined secondary shock. The large shift across the primary shock is to be expected because of the large density ahead of the shock.The multiple, upstream facing disturbances which do appear may result from the interaction of the secondary shock and the contact surface region.

The trajectories of the primary and secondary shocks, measured from the interferogrammes, and the primary shock and contact surface arrival times at one nozzle station, measured from the cylinder flow experiments, are shown for the range of shock conditions, in Fig. 5.8. Also shown in this figure are the results from the analytic model for the trajectory of the instantaneous centre of mass of the system of the primary and secondary shock (see Chapter 2). Good agreement can be seen to exist between the two experimental methods and the theoretical predictions. The model for the starting processes in the nozzle, presented in Chapter 2, is

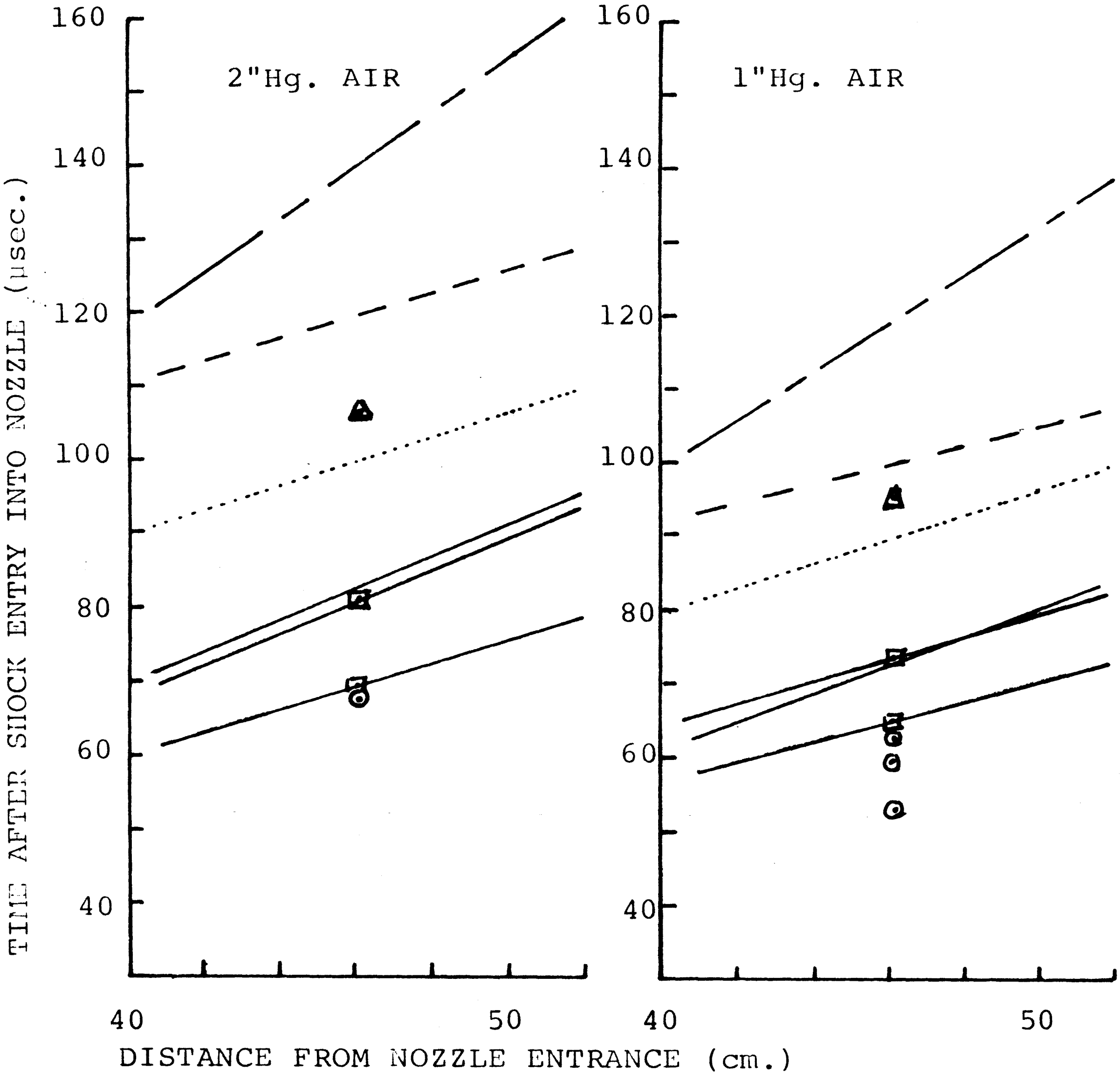

Fig. 5.8. The trajectories of the important nonsteady flow features in the nozzle - a comparison of the experiment and the predictions of the analytic model.

the primary and secondary shocks from the interferogrammes.

the primary shock from the cylinder flow shock layer luminosity.

the contact surface from the cylinder flow

.... head of the nonsteady expansion (predicted)

———— analytic model - shock system centre of mass with prior steady flow.

_ _ _ _ _ predicted contact surface.

— – — – analytic model shock system c of m no prior steady flow.

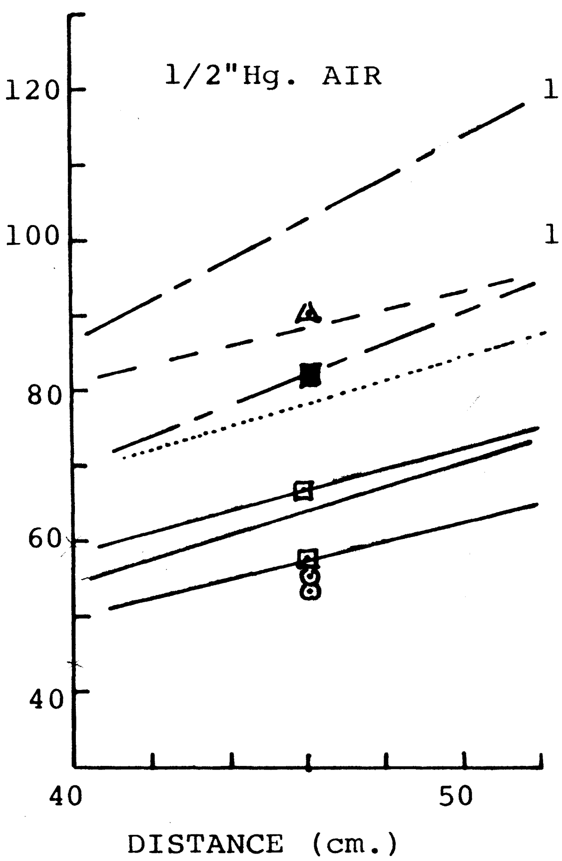

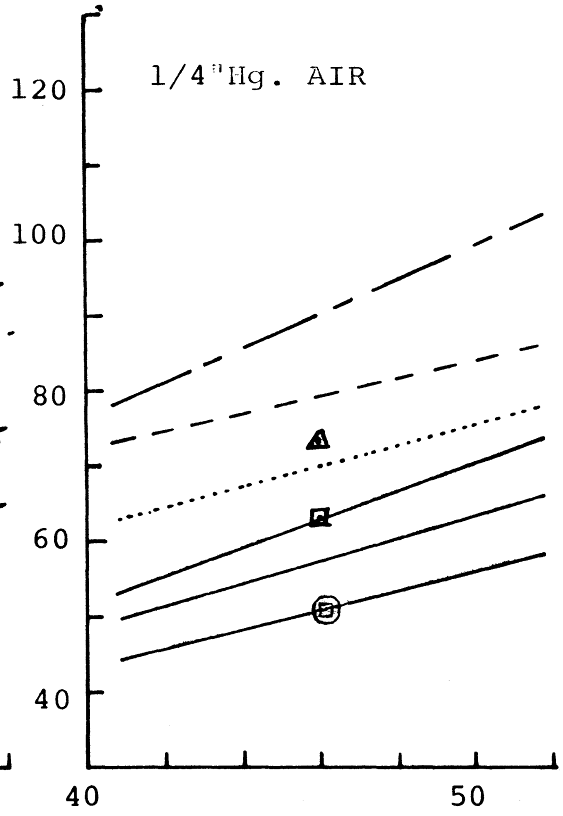

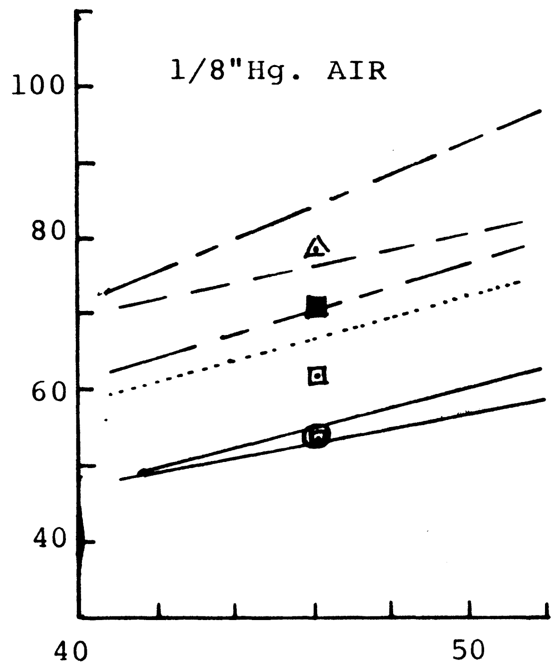

Fig. 5.8. (Cont.)
(see previous page for details)

primary shock no prior steady flow - from the interferogrammes.

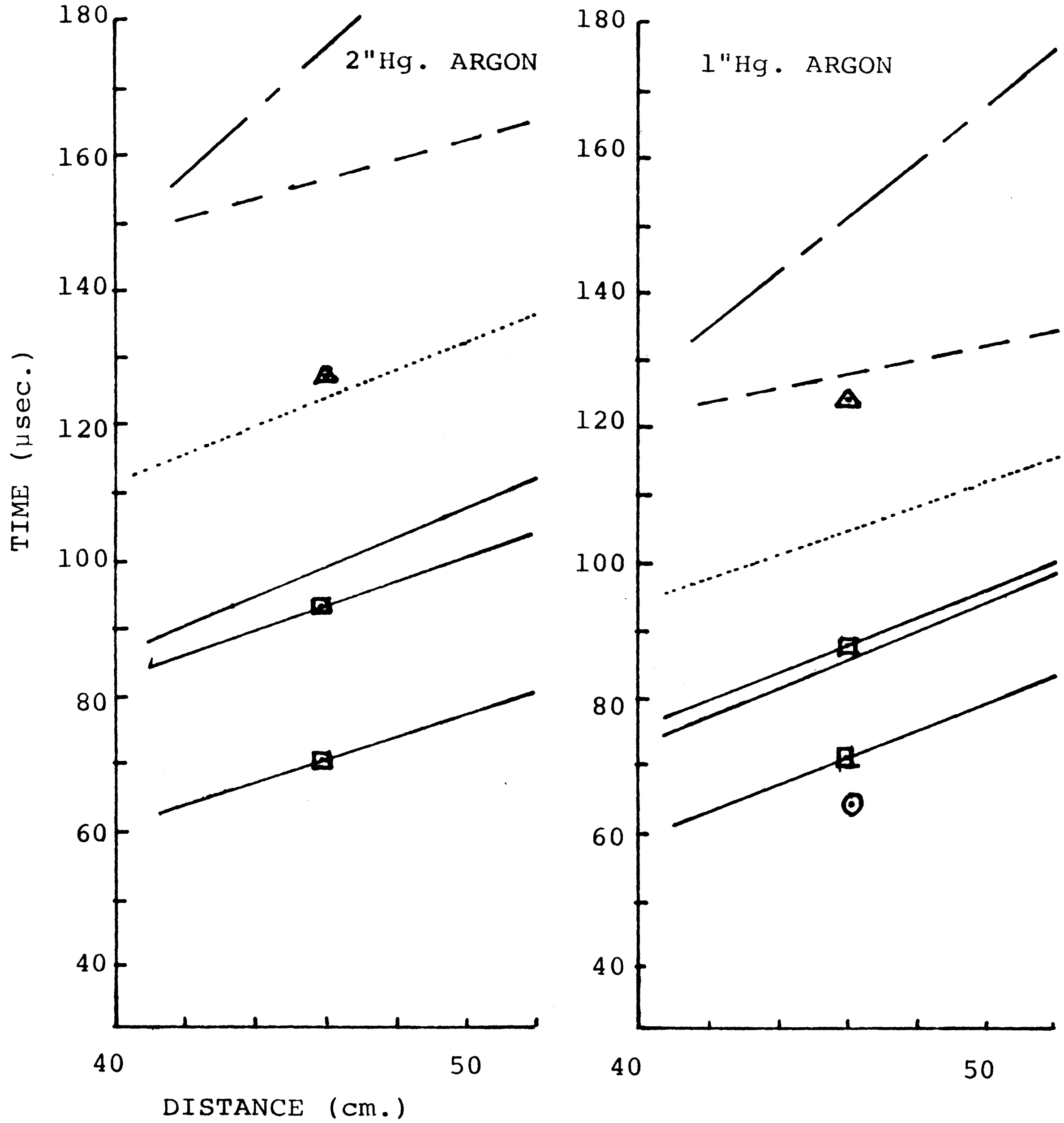

Fig. 5.8. Trajectories of the important features of the nonsteady flow (Cont.)
(see previous pages for details)
Argon plasmas are undecayed.

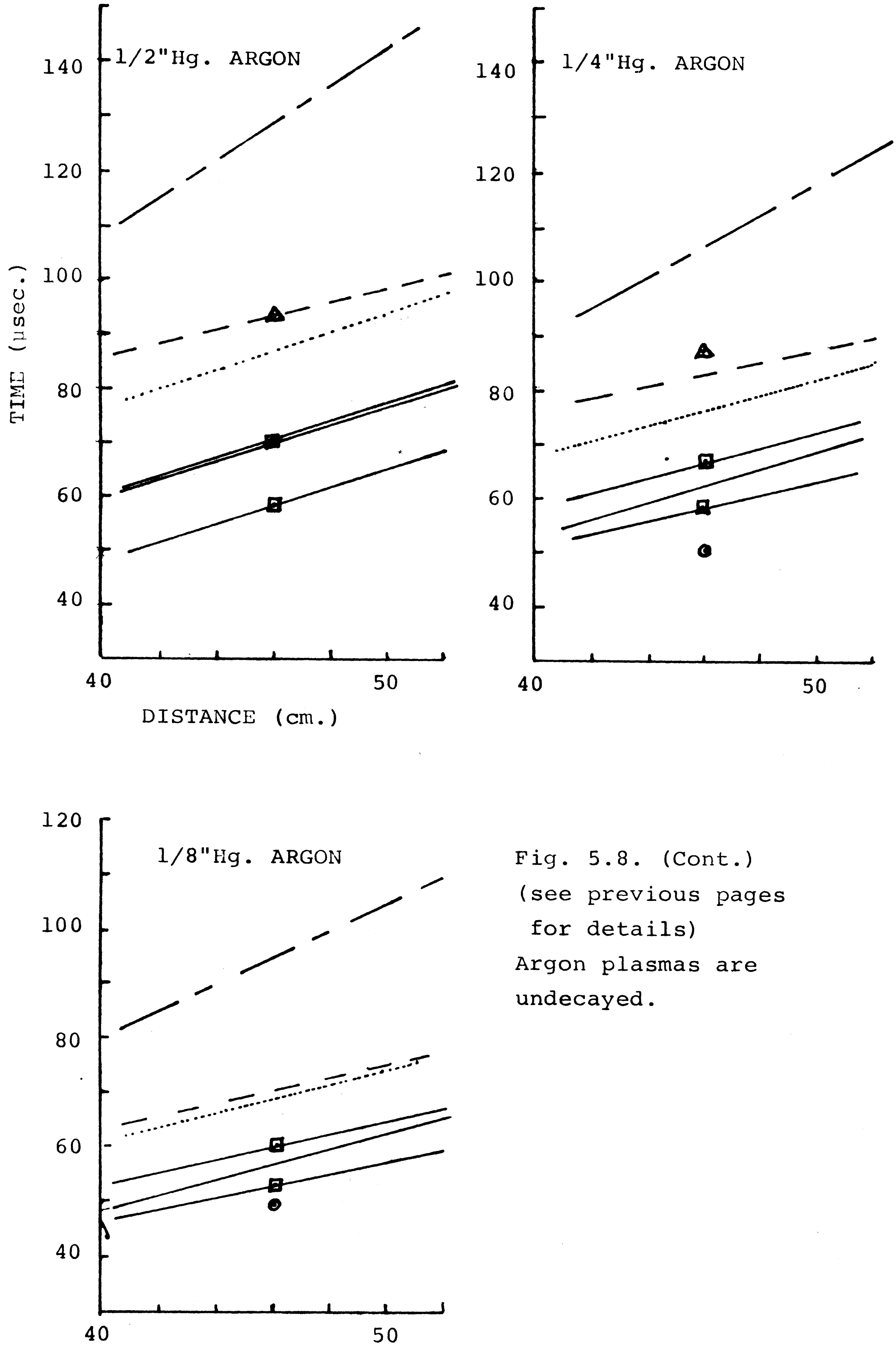

Fig. 5.8. (Cont.)
(see previous pages for details)
Argon plasmas are undecayed.

therefore confirmed both qualitatively and quantitatively.

The final point to be noted in this section is that the vertical slit interferogrammes show that the test section flow disturbances are approximately one dimensional (see the example of a vertical slit interferogramme in Fig. 5.7).

5.4 EXISTENCE OF A PRIOR, STEADY, SUPERSONIC FLOW.

Up to this point it has been assumed that the prior steady flow (PSF) is supersonic throughout the nozzle and test section. Calculations presented in Appendix A show that there is ample time for the establishment of an entirely supersonic PSF. The experimental evidence for its existence will be examined in this section.

The assumption has important implications for the measurements of the refractivity of the steady test gas flow. The fringe shift at a point in the test gas flow is measured relative to the fringe pattern in the PSF. A normal, upstream facing recovery shock in the PSF, standing at the nozzle exit, would decrease the fringe shift for a 2"Hg shot by approximately half a fringe. The assumption has weaker implications for the calculations of the trajectory of the starting shock system. The same normal recovery shock would delay the arrival of the shock system by the amount of the order of the uncertainty in the experimental results for the shock arrival times.

The low densities and stagnation pressures in the PSF make direct observation of the flow too difficult. The fringe shift across the primary shock in the test section was chosen as an indirect measure of the test section density. Neglecting changes in specific refractivity across the shock, this fringe shift is, approximately, directly proportional to the density ahead of the shock. The existence of an entirely supersonic PSF will be taken to be shown if the density ahead of the primary shock is that for an entirely supersonic PSF.

From the air shots, the computer programme NSHOCK (Garr, et al 1966) was employed to calculate the fringe shift across a normal shock in the test section. NSHOCK computes the physical and chemical properties of a reacting gas in chemical nonequilibrium behind the normal shock. Shock calculations were carried out assuming that the PSF was entirely supersonic. Later, other calculations were performed assuming that the normal recovery shock, mentioned above, existed. The primary shock speed, necessary input to NSHOCK, was measured from the horizontal slit interferogrammes.

To calculate the fringe shift, the primary shock was assumed to be normal and 6" in diameter (the design exit dimater of the nozzle before truncation). The vertical interferogrammes show that the shock is slightly convex, looking upstream towards the shock, and has a diameter of more than 6" (see Fig. 5.7). However, the normal shock approximation should model the primary shock sufficiently well to enable an estimation of the density ahead of the shock and thus test the supersonic prior steady flow assumption. In Fig. 5.9, the results of the fringe shift calculations, made assuming a supersonic PSF, are compared with the measured fringe shifts across the primary shock, over the range of gas conditions for air. The fringe shifts for a PSF with a normal recovery shock, as described above, are not shown but are much higher than the experimental fringe shifts. For example, for the 2"Hg initial pressure shots, the frozen fringe shift is 3.5 and the equilibrium fringe shift, reached 1m/m. behind the shock, is 7.4. It can be seen from Fig. 5.9 that the magnitude of the experimental fringe shift, and therefore the density ahead of the primary shock is consistent with the assumption of an entirely supersonic prior steady flow for all conditions.

The treatment of the argon shots was,of necessity, different to that for the air shots. NSHOCK could not model the ionisation reactions occuring behind the shocks in argon. H. Wong and D. Bershader (1966) show that the onset of ionisation behind a normal shock in argon is considerably delayed by the slow rate of energy transfer from the heavy particles to the electrons, via elastic collisions, coupled with the rapid loss of energy by the electrons acting as third bodies in the collisional ionisation of argon. Wong and Bershader's calculations and experiments show, for their shock conditions, that ionisation remains frozen ($\leq$10% of the equilibrium ionisation fraction) for a distance behind the shock approximately 10 times that predicted by NSHOCK, which assumes a rapid energy transfer from the heavy particles to the electrons. For the primary shocks in the test section, NSHOCK predicts that the chemistry will be frozen for at least 1 m/m behind the shock. It may therefore be expected, from Wong and Bershader's work, that the ionisation will

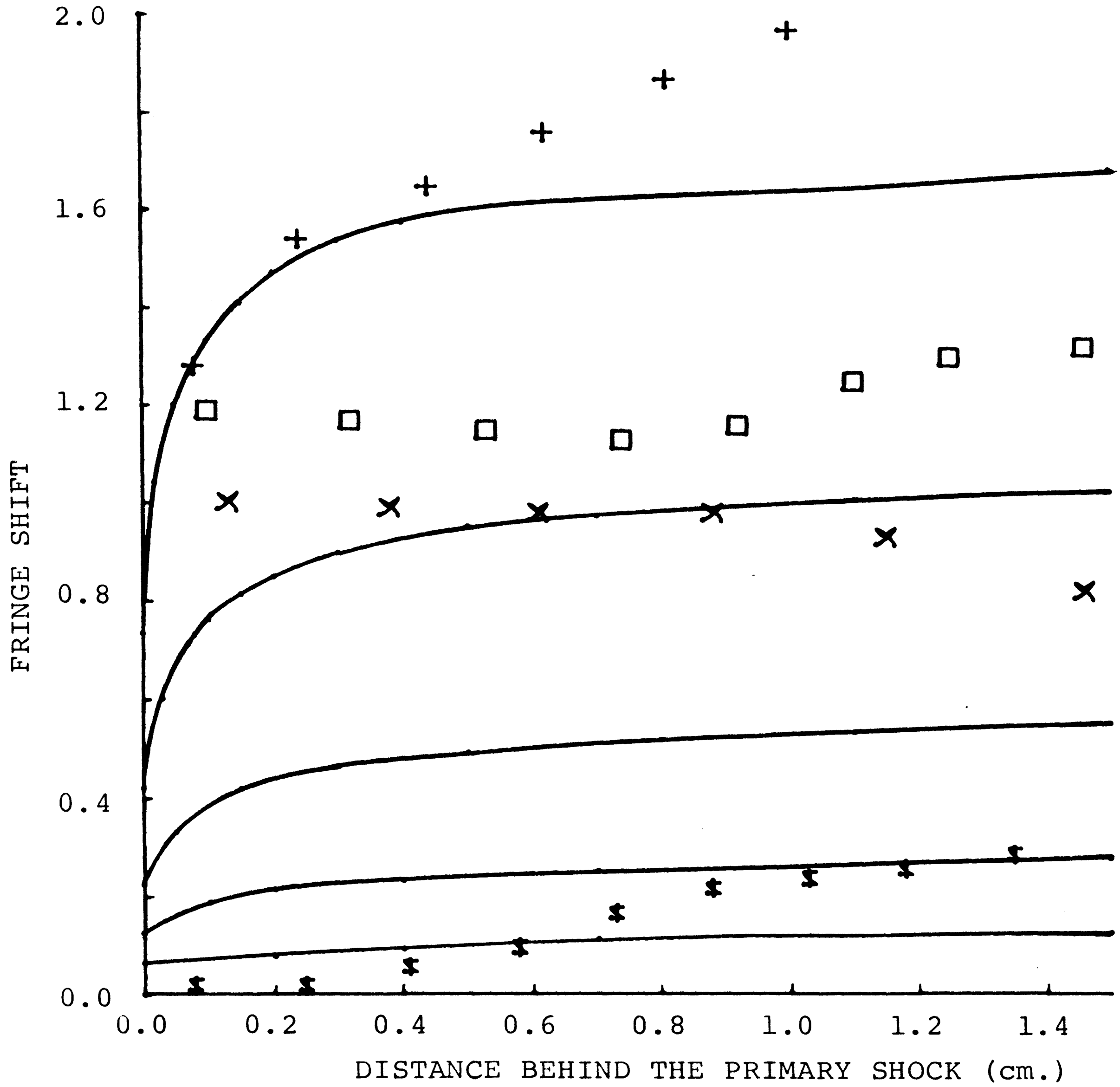

Fig. 5.9. Fringe shift behind the primary shock in the test section - AIR SHOTS. Lines are theory for an entirely supersonic prior steady flow. Experimental points are:

+ 2"Hg., □ 1"Hg., × 1/2"Hg., ⌶ 1/8"Hg.,

remain frozen for up to 1 cm. behind the shock. This distance is easily resolved on the interferogrammes, as will have been noted from the air results above. The results of the calculations of the fringe shift across a 6" diameter, normal shock in argon with chemistry frozen, and density ahead of the shock that for an entirely supersonic PSF, are shown is Fig. 5.10. Also shown in this figure are the experimental fringe shifts measured across the primary shocks. Again, the experimental fringe shifts are consistent with an entirely supersonic PSF ahead of the primary shock.

It is interesting to note that, for all conditions, the experimental fringe shift behind the normal shocks in argon is positive indicating that no significant amount of ionisation has taken place within 1 or 2 cm. of the shock. This observation verifies that the chemistry is frozen behind the primary shock for the shock conditions found in the test section. For all shocks considered, the equilibrium ionisation fraction was sufficient to produce a negative fringe shift of between -0.5 and -1.0 fringes behind the shock when an entirely supersonic PSF was assumed.

5.5. STEADY FLOW PROPERTIES.

5.5.1. INTRODUCTION.

In this section, the results of the investigations into the nature and properties of the flow between the secondary shock and the contact surface will be presented. The steady flow, if it exists will lie in this region of the flow. For convenience, the whole of the region will be referred to as the steady flow, keeping in mind that the steadiness of the flow is one of the subjects of the experimental investigation.

The horizontal and vertical slit interferogrammes produced the most usable results, of the experiments performed, in relation to the steady flow. The bar gauges, which should have provided information on the stagnation pressures of the flows, could not be calibrated and the data from these experiments had to be discarded.

The aim of the investigation of the steady flow region was to discover the extent to which the flow was steady and uniform and whether the observed absolute values of the flow properties agreed with those predicted by the steady flow calculations. The horizontal slit interferogrammes provided

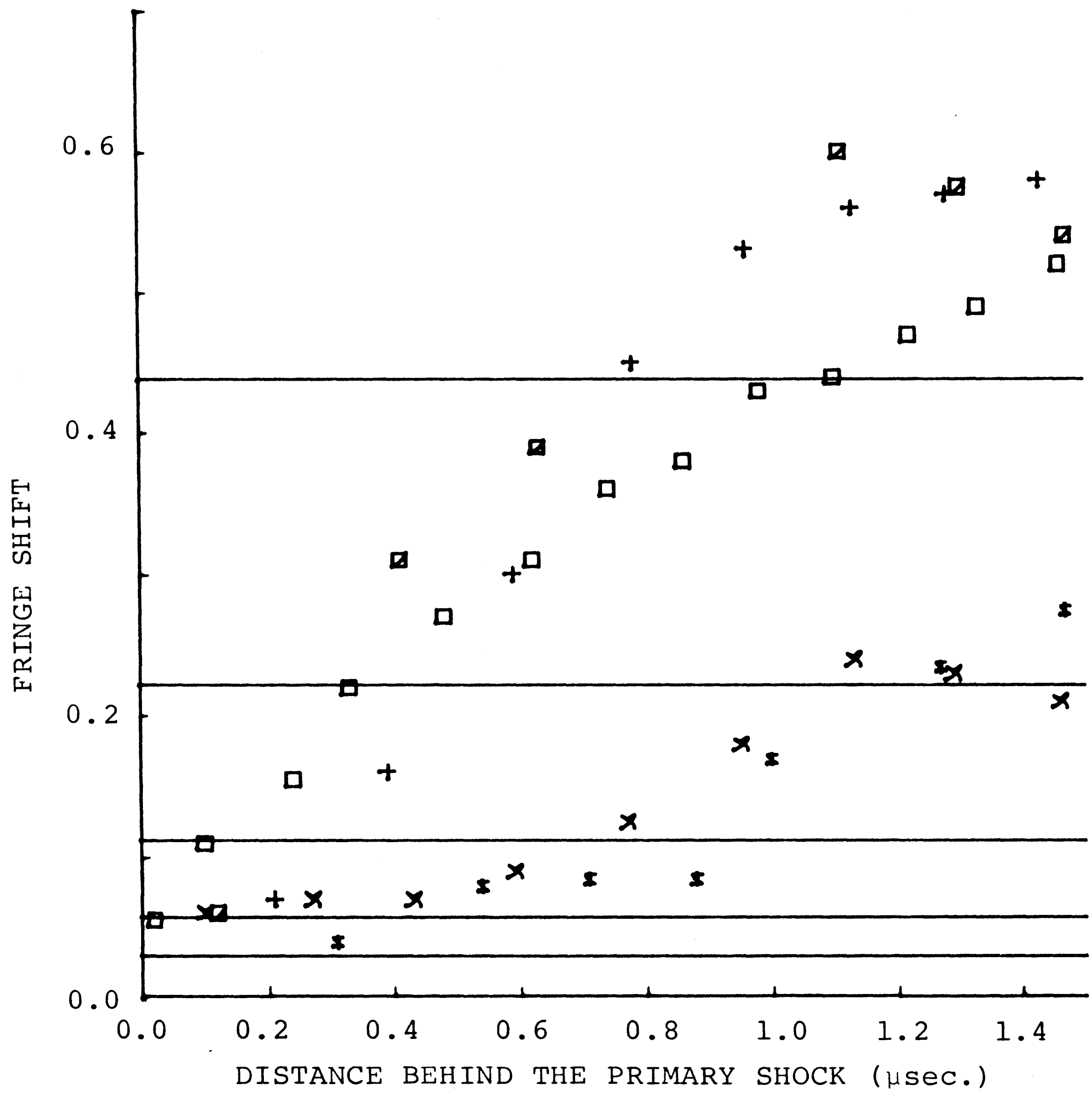

Fig. 5.10. Fringe shift behind the primary shock in the test section - ARGON SHOTS. Lines are theory for an entirely supersonic prior steady flow. Experimental points are:

+ 2"Hg., □ 1"Hg., × 1/2"Hg., ⊠ 1/4"Hg., ⌶ 1/8"Hg.

information on the steadiness of the flow at a nozzle station, the uniformity of the flow properties in the axial direction and the direction and the divergence or convergencee (if any) of the flow. The vertical slit interferogrammes were used to find the distribution of refractivity in a plane perpendicular to the nozzle axis.

The results of the investigation of the steady flow will be considered in six parts:

(i) The method of treatment of the interferogrammes to obtain the test flow fringe shift relative to the prior steady flow.

(ii) The horizontal slit interferogrammes.

(iii) The vertical slit interferogrammes.

(iv) The physical and chemical properties of the steady air flows.

(v) The physical and chemical properties of the steady argon flows.

(vi) Body flows.

5.5.2. TREATMENT OF THE INTERFEROGRAMMES.

The analysis of the swept slit image interferogrammes takes the form of a comparison of the fringe pattems produced by the presence of the test gas in the field of view with the fringe pattern ahead of the primary shock. The measurement of the fringe positions in these patterns could not be done successfully by hand because the maximum fringe shift observed between two patterns is only two fringes and is generally much less than this. A micro-densitometer, developed in the Physics Department at A.N.U. by Dr. J. Sandeman and Mr. G. Spackman, in collaboration with Torrens Industries, was used to digitise the fringe patterns on the interferogrammes. A schematic diagram of the micro-densitometer is shown in Fig. 5.11. The section containing the light emitting diodes, the focusing lens, the aperture, the photodiode and the preamplifier were mounted on the movable carriage of an HP 9862A plotter. The interferogramme, in the form of a photograph, was fixed to the plotting surface beneath the micro-densitometer. The micro-densitometer measured the intensity of the light from the L.E.D.'s which was reflected off the photograph. The diameter of the section of photograph observed, at one time, by the micro-densitometer was 0.018". The apparatus on the plotter carriage was traversed across

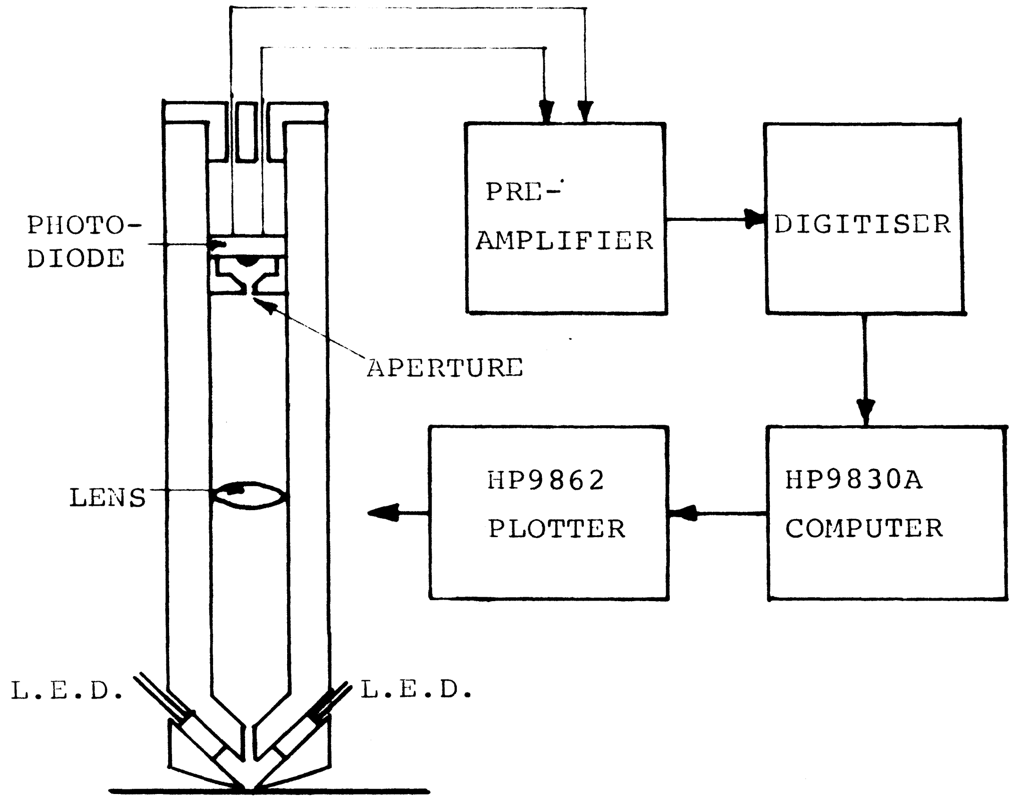

Fig. 5.11. The design of the densitometer used for scanning the interferogrammes, with the preamplifier, digitiser, computer and plotter relations.

the photograph along lines of constant time after the beginning of the Image Converter Camera (ICC) sweep. At 265 equally spaced points on this traversing scan, the signal from the preamplifier was digitised and fed directly into an HP9830A computer, which stored the results on magnetic tape. The computer also controlled the traversing of the photograph by the plotter carriage and the attached apparatus. The digitised signal produced by the system consisted of a three digit integer which was directly proportional to the intensity of the light reflected from the photograph. The reflected intensity pattern produced by the scanning of the interferogramme in Fig. 5.7a is shown in Fig. 5.12a.

After the raw signal from the digitiser has been fed to the computer, the signal is smoothed with the aid of a fast fourier transform programme, developed in the Physics Department A.N.U. by Drs. J. Sandeman and M. Andrews. The fourier transform programme transforms the signal into a series of 129 component frequencies. The high frequencies in this spectrum arise from the graininess of the film and print, electrical noise, random errors in the placement of the micro-densitometer, etc. The low frequencies are a result of one of the interferometer beams being more intense than the other, coherence effects between two beams, etc. The pattern of the interference fringes is contained in some intermediate range of frequencies. Therefore, before re-transforming the original digital signal, the high and low frequency contributions are deleted. The smoothed intensity, distribution derived in this way from the raw signal shown in Fig. 5.12a, is presented in Fig. 5.12b. Tests showed that the re-transformed signal was insensitive to the range of frequencies deleted. During the analysis of the interferogrammes, care was taken to allow a large range of frequencies to remain incorporated in the signals so that no information about the flows was lost.

The fringe positions are the positions of the zeros of the smoothed densitometer signal. To find the positions of these zeros, an operation was performed on the transform of the smoothed signal. Retransformation then produced the first derivative of the smoothed signal which was scanned by the computer for the positions of the zeros. These were then recorded on magnetic tape, after editing by the computer

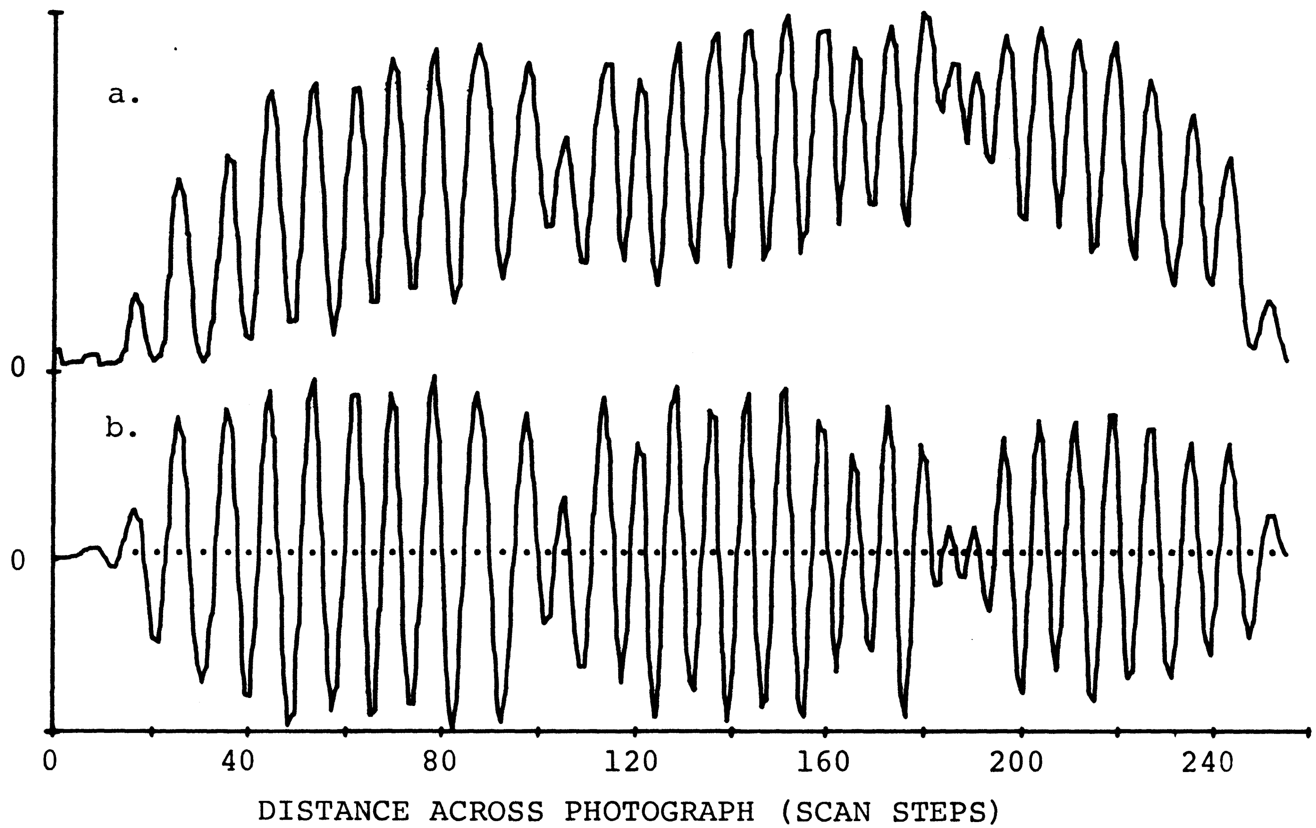

Fig. 5.12. Intensity vs. distance across scan for scan of the horizontal slit interferogramme shown in Fig. 5.7.

a. Raw scan   b. Smoothed scan (points are fringe positions).

operator , to delete any zeros not corresponding to the fringes on the interferogramme. The numbering of the fringes was also performed by the computer, under the supervision of the operator, with constant reference to the original photograph. The fringe positions are marked with the smoothed signal on Fig. 5.12b.

The fringe shift distribution in the test flow was found by taking the difference between the fringe pattern of interest and the fringe pattern ahead of the primary shock, the latter being, in most cases, in the prior steady flow. The random error present in the final fringe shift was, in general, ±0.05 fringes. The systematic error, due to misalignment of the photograph on the plotter, and distortion of the interference pattern, by the ICC and the printing process was estimated to be another 0.1 fringes. Manual measurements of the fringe shift patterns agreed with the machine measurements, although the random error for the hand measurements was ±0.15 fringes.

5.5.3. THE HORIZONTAL SLIT INTERFEROGRAMMES.

Scans on the horizontal slit interferogrammes were taken along (straight line) curves of constant time after the beginning of the ICC sweep. The resulting patterns were, therefore, the fringe distributions along a direction parallel to the flow at a particular laboratory time.

The fringe shift will be constant along steady flow gas particle trajectories if the following conditions are met:

(i) The flow is parallel.

(ii) The gas particles in the flow follow steady flow trajectories.

(iii) Chemical reactions occuring in the flow in the test section do not significantly affect the refractivity of the gas.

(iv) The integrated refractivity across the flow is not significantly affected by the growth, with distance along the flow direction, of the expansion from the nozzle end.

Condition (iii) is shown to hold by computer calculations of the nozzle flows. These will be presented later in this chapter, in sections 5.5.5. and 5.5.6.

Condition (iv) is shown to hold in the next section in this chapter where the vertical slit interferogrammes are discussed.

The constancy of the fringe shift along the theoretical steady flow gas particle trajectories will therefore be taken as a test of the deviation of the flow from the ideal parallel flow and as a test of the assumption that the particles follow the theoretical steady flow trajectories.

It was shown in Chapter 2 that there are probably no strong pressure disturbances originating from the driver gas/ test gas mismatch in the nozzle flow. Support for this claim came from inspection of the interferogrammes reported in section 5.3 of this chapter. The contact surface can therefore be expected to follow, approximately, a steady flow particle trajectory in passing through the nozzle and test section. One point on this trajectory is known from the experiments, reported in section 5.3. of this chapter, in which the bow shock on a cylinder was monitored and the primary shock and contact surface arrival times at the cylinder were measured. The rest of the trajectory can then be deduced using the theoretical steady flow speeds, in the nozzle and the test section, provided by NFAPC. In fact, because the steady flow speed as given by NFAPC, is constant throughout the test section, the contact surface trajectory in the test section will be a straight line on the x-t plane. In Fig. 5.13 the fringe shifts, measured on the horizontal slit interferogrammes, are plotted against time before the arrival of the contact surface at the station where each fringe shift was measured. This is, of course, equivalent to plotting the fringe shifts against the number of the steady flow trajectory on which they lie.

It can be seen from Fig. 5.13 that the fringe shift is indeed constant along the steady flow trajectories within the uncertainty in the fringe shift. A necessary condition for the flow to be parallel and follow steady flow trajectories is thus satisfied.

Fig. 5.13 shows that the variation of integrated refractivity between the secondary starting shock and the contact surface is ±25% from the mean. The deviations from the mean may be due either to the presence of the nonsteady expansion wave or to gradients of the flow properties in the test gas slug in the shock tube. The uncertainty of the trajectory of the nonsteady expansion wave in the nozzle has already been discussed in Chapter 2. The deviations are, however, not serious and the flow between the secondary shock and the contact surface is quite usable.

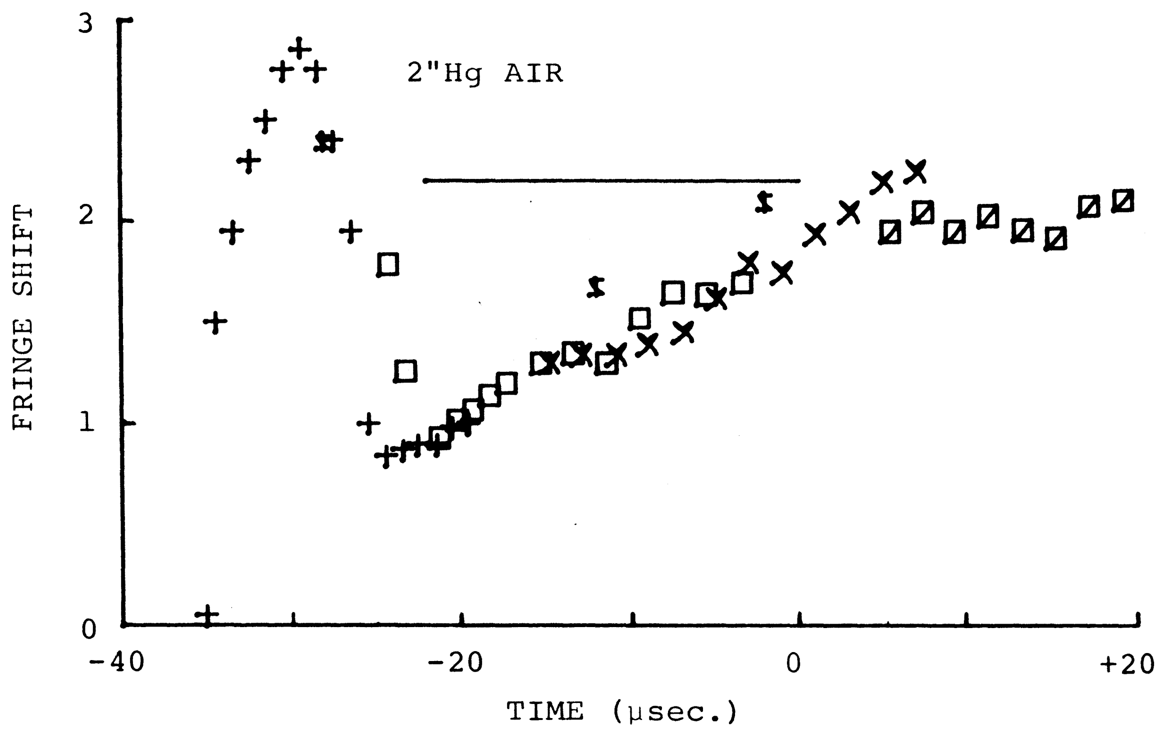

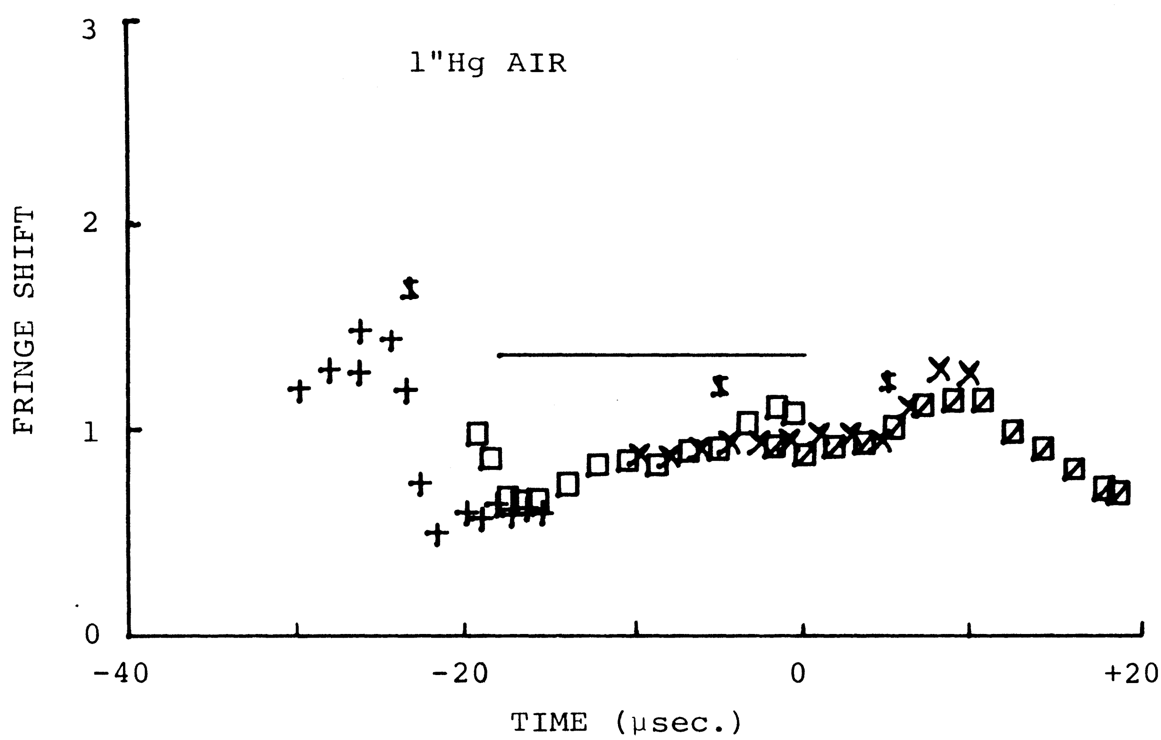

Fig. 5.13. Fringe shift on slit interferogrammes vs. time before contact surface arrival at the vertical slit station.

+ Scan 2., □ Scan 3., × Scan 4., ⊠ Scan 5.

——— Theory - steady flow fringe shift

Central shift of several different scans of the vertical slit interferogrammes.

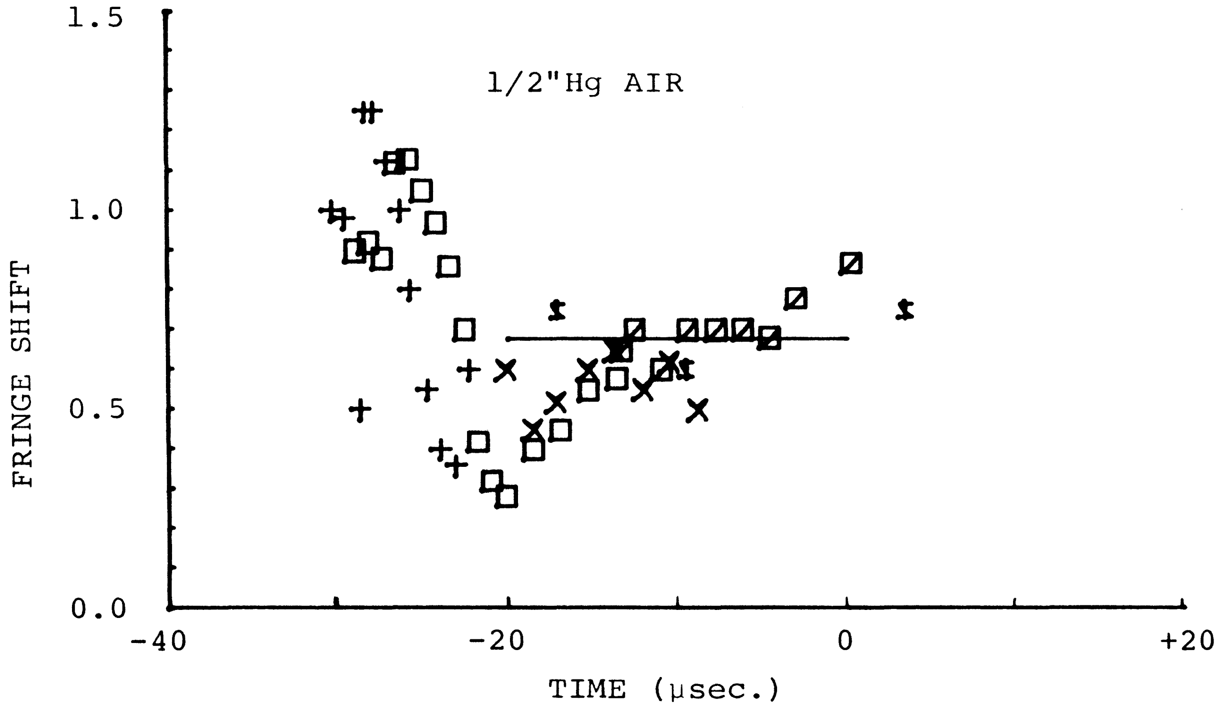

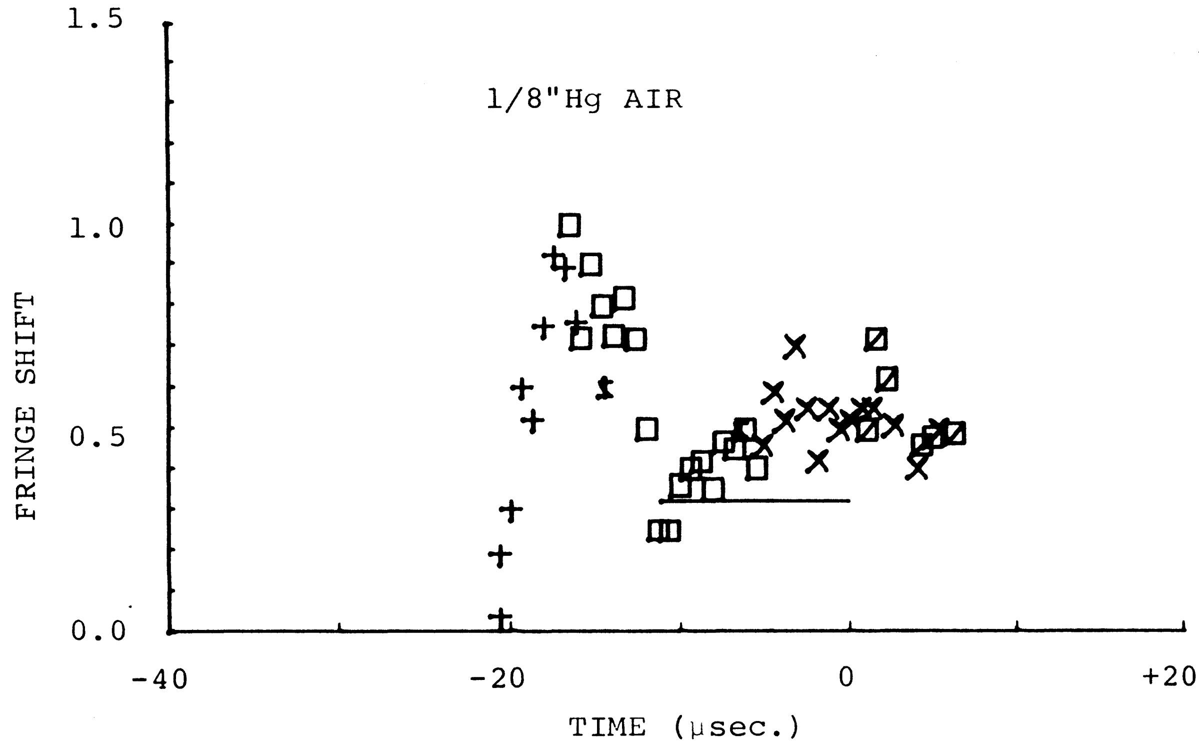

Fig. 5.13.(Cont.) Fringe shift on the slit interferogrammes vs. time (see previous page for details).

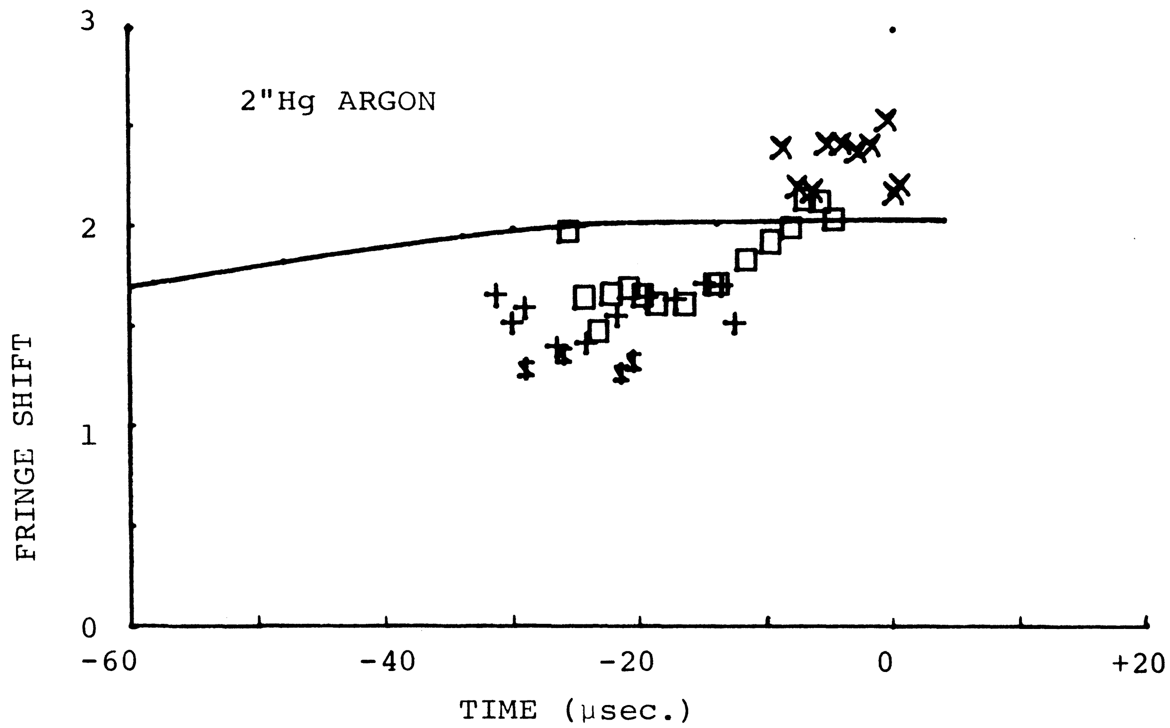

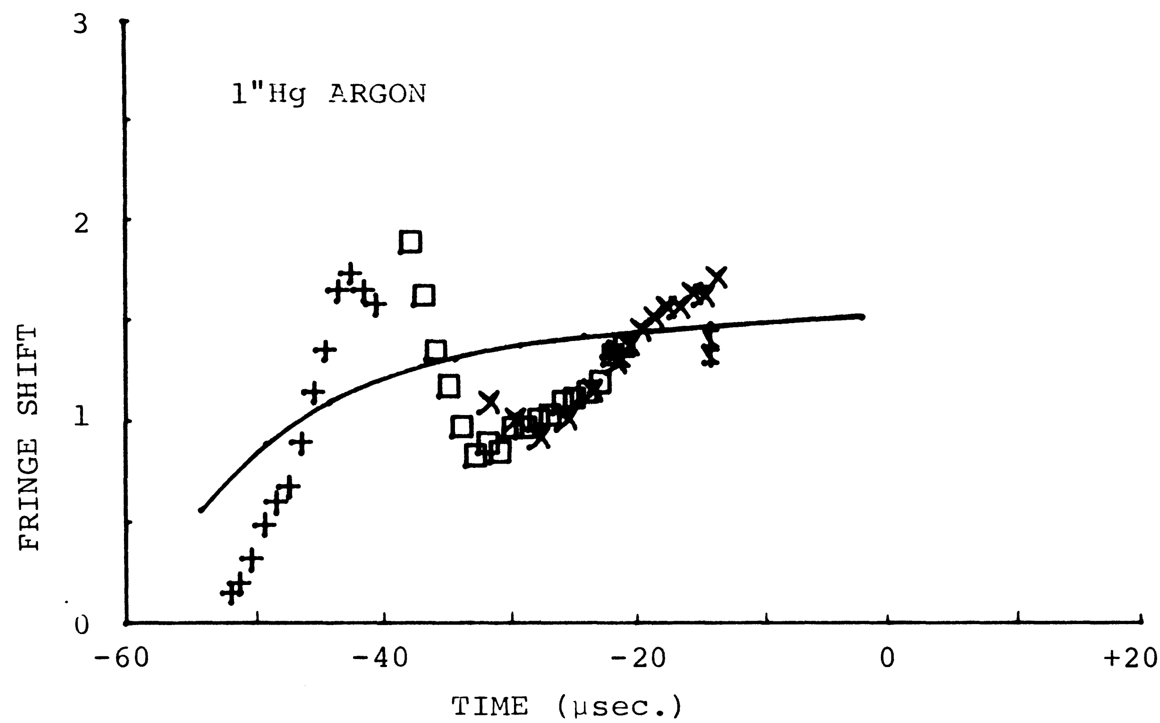

Fig. 5.13.(Cont.) Fringe shift on slit interferogrammes vs. time (see previous pages for details).

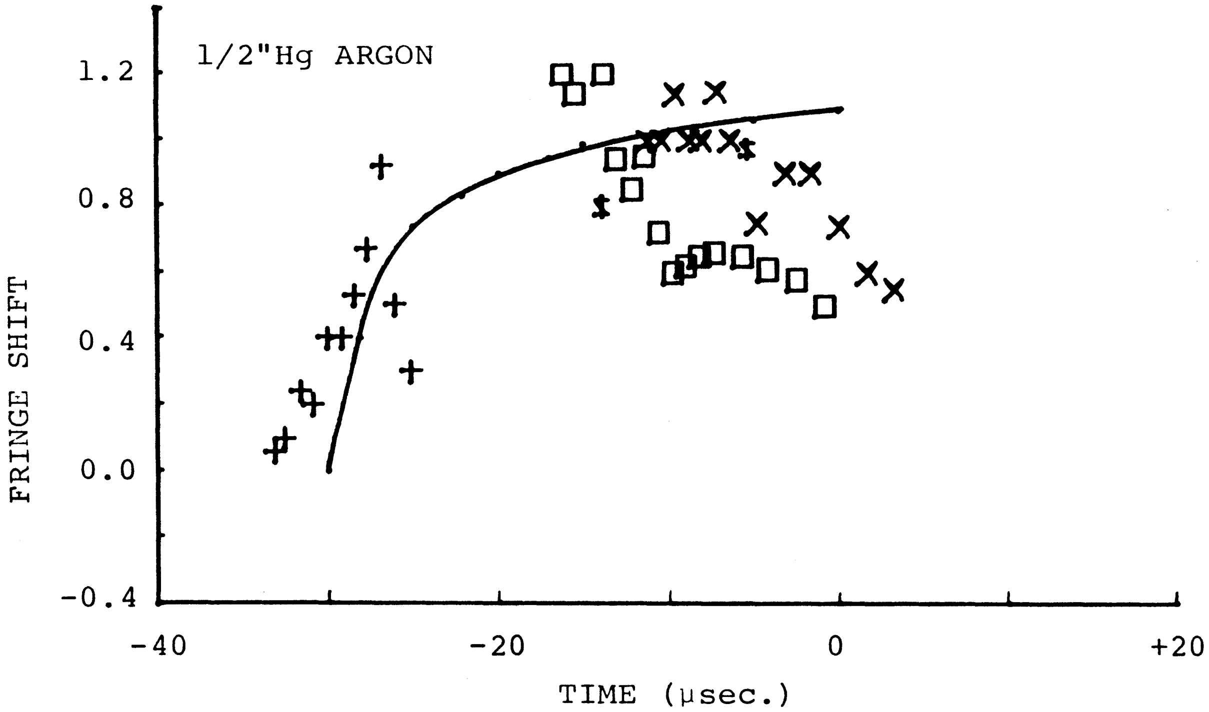

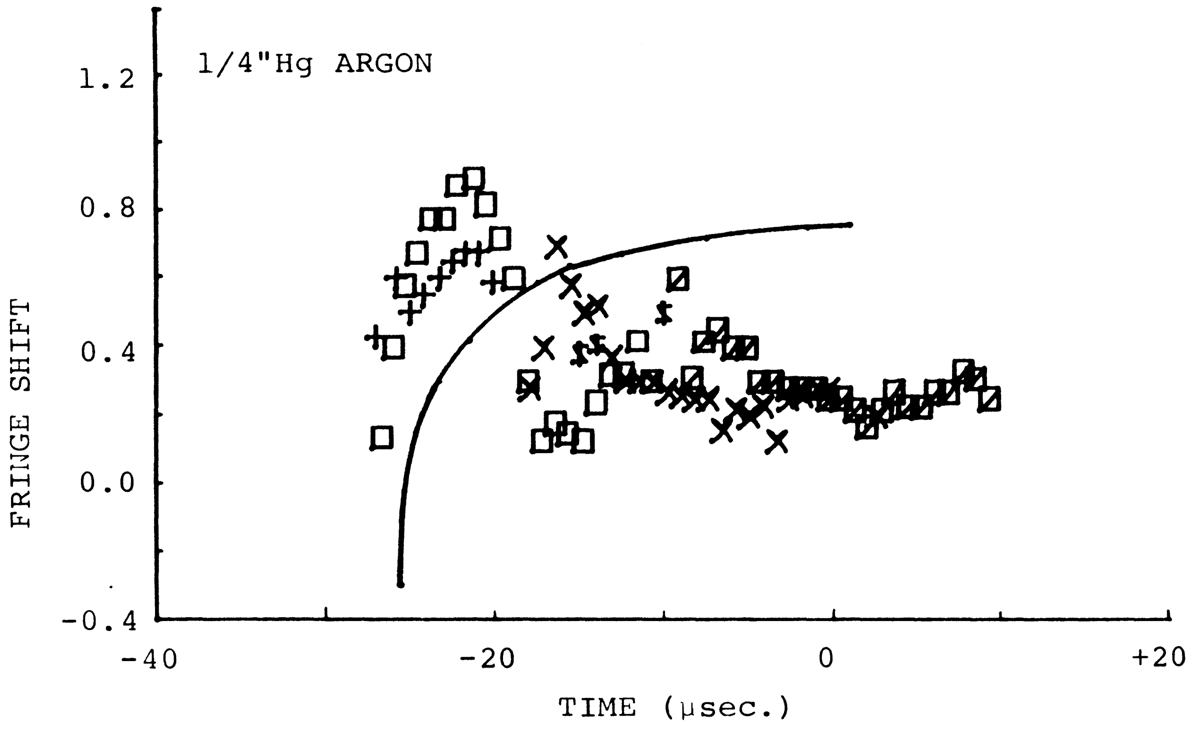

Fig. 5.13.(Cont.) Fringe shift on the slit interferogrammes vs. time (see previous pages for details).

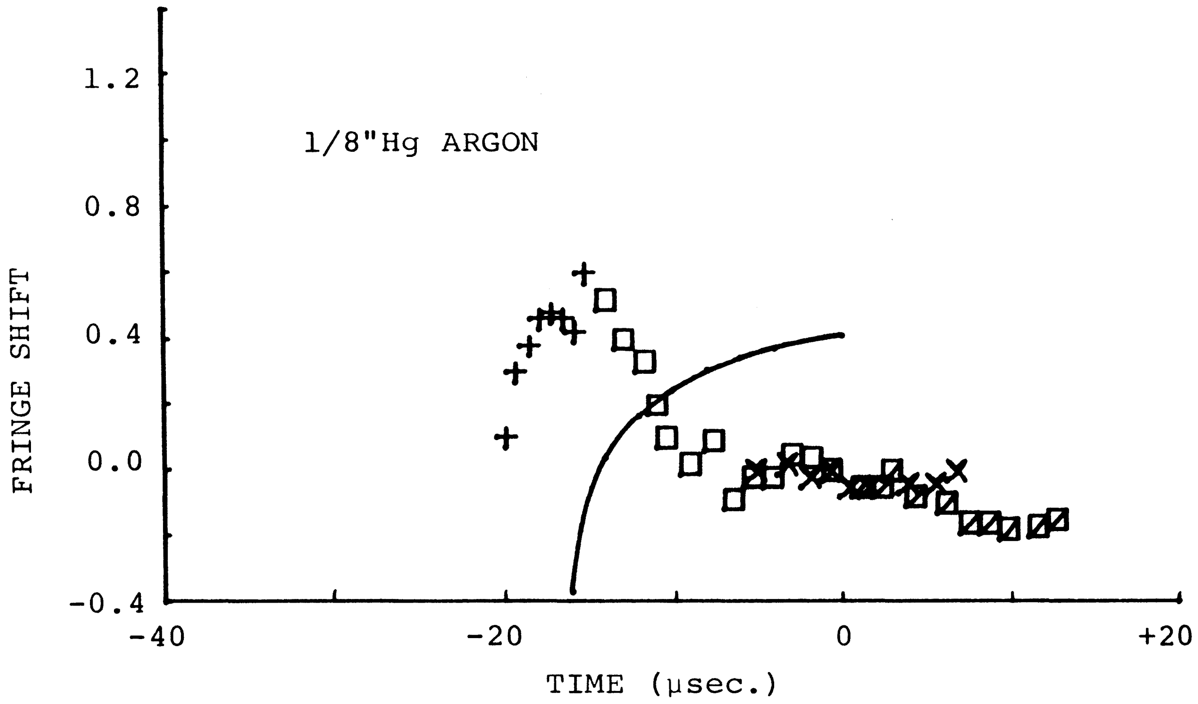

Fig. 5.13. (Cont.) Fringe shift on the slit interferogrammes vs. time (see previous pages for details).

5.5.4. VERTICAL SLIT INTERFEROGRAMMES.

As in the case of the horizontal slit interferogrammes, the densitometer scans were made along (straight line) curves of constant time after the Image Converter Camera (ICC) sweep beginning. In section 5.3 of this chapter, it was pointed out that the vertical slit interferogramme showed that the test section flow closely approximated a one-dimensional flow. Curves of constant time after the ICC sweeps start are also, therefore, curves of constant time before the arrival of the contact surface.

Shown in Fig. 5.14 is the fringe shift pattern resulting from a scan of the vertical slit interferogrammes which appears in Fig. 5.7b. Superimposed on this fringe shift distribultion is the curve of fringe shift vs. radius from the slug centre, which would occur if the slug was uniform. The curve results from taking a weighted mean of the central fringe shifts predicted by the experimental fringe shift at each radius. It can be seen from the figure, that the measured fringe shift distribution is lower at the edges of the slug and slightly higher in the centre of the slug, than expected for a uniform slug. This is characteristice of all the measured fringe shift distributions and is due to the presence of the expansion wave originating around the lip of the nozzle exit.

The fringe pattern on the vertical slit interferogramme is determined by the distribution of refractivity in a plane perpendicular to the flow. In order to deduce a unique refractivity distribution from the fringe shift distribution, it was necessary to make an assumption regarding the symmetry of the refractivity distribution. It was assumed that the refractivity distribution was axisymmetric about the nozzle axis of symmetry. The continuous axisymmetric refractivity distribution was then approximated by a series of concentric annuli each with a constant refractivity. An illustration of this approximation is shown in Fig. 5.15. It is clear from the figure, that the magnitude of the fringe shift at point f_1 on the interferogramme depends only on the refractivity of the gas in annulus 0_1. The fringe shift at f_2 depends only on the refractivity of the gas in annuli 0_1 and 0_2, and so on. The refractivities in the annuli can thus be determined, one at a time, beginning with the outermost annulus and ending with the centremost annulus. Such a

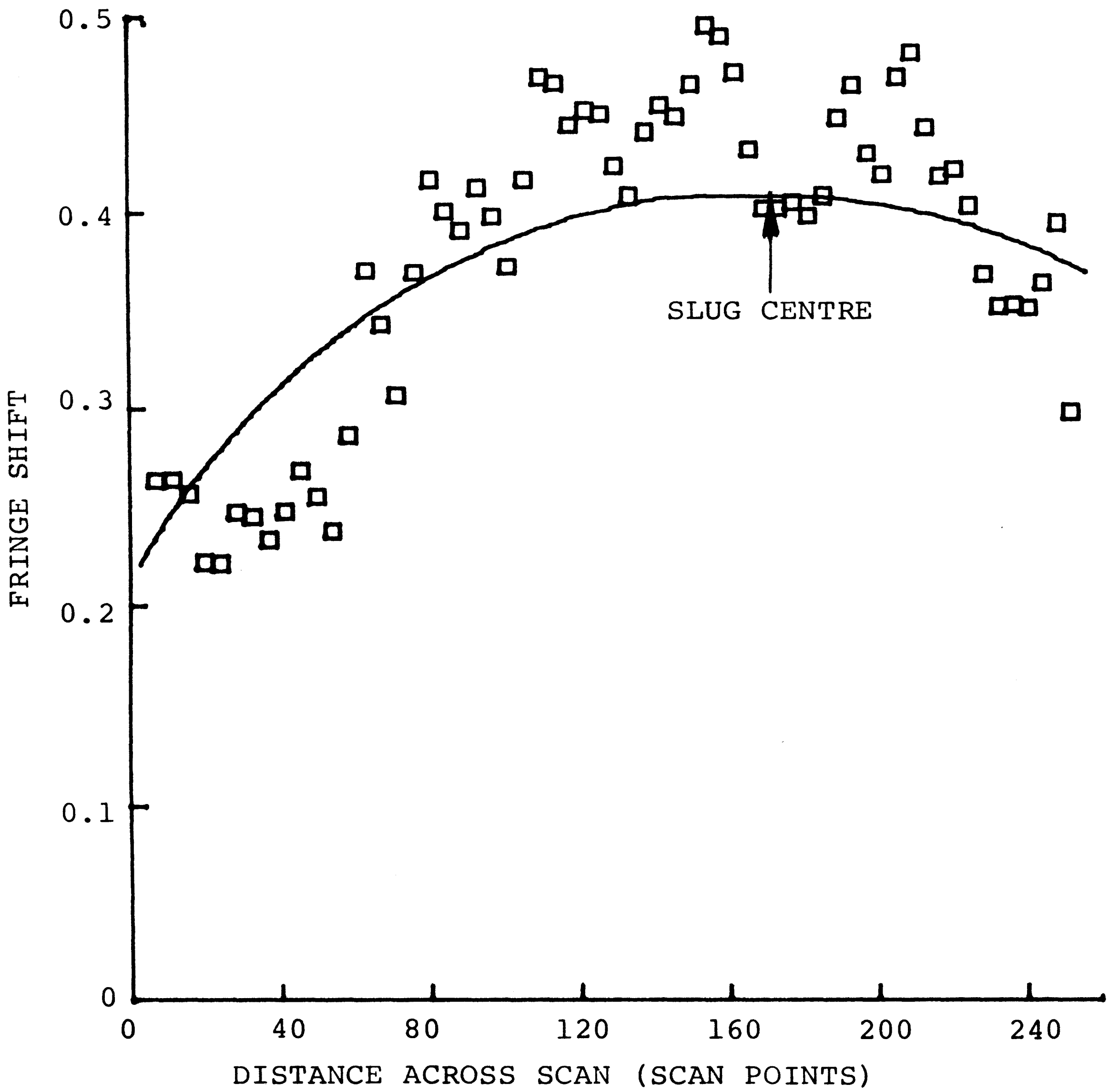

Fig. 5.14. Fringe shift pattern for scans of vertical slit interferogramme shown in Fig. 5.7.

□ measured fringe shift

——— fringe shift for a uniform slug 6" diameter.

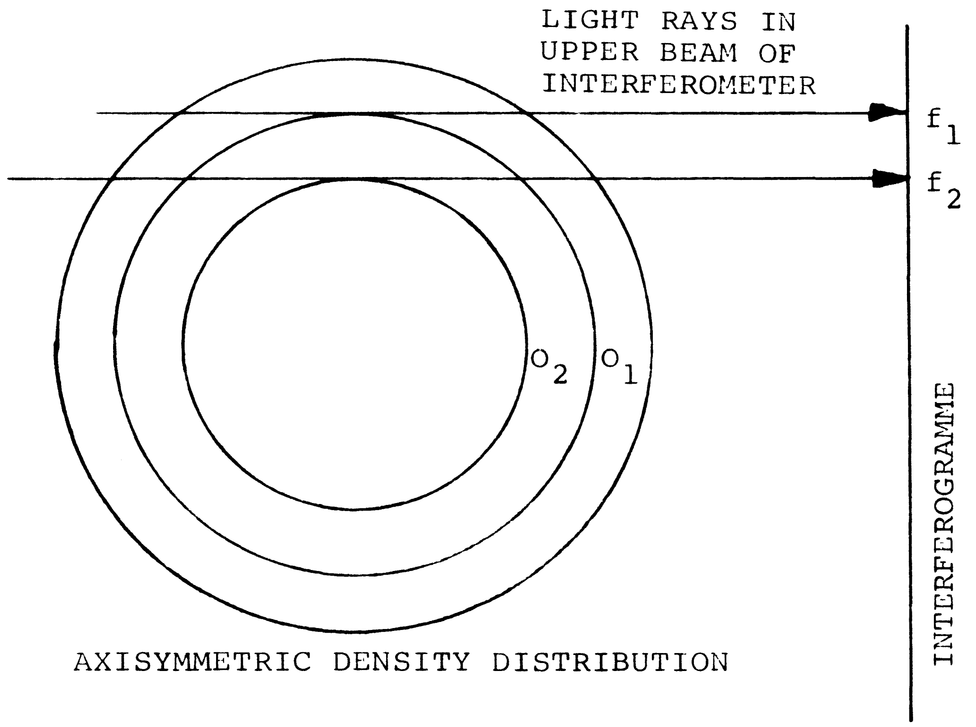

Fig. 5.15. Schematic diagram of the approximation to the refractivity distribution in a plane perpendicular to the flow direction in the nozzle. The approximation takes the form of annuli of constant density centred on the nozzle axis.

stepwise determination has been carried out for the high initial pressure shots and the results are shown in Fig. 5.16. The reference refractivity (density) used to normalise the distribution shown in the figure is the refractivity required, over a path length of 2 x 7.62 cm., to produce the observed fringe shift across the flow centre. From the figure it can be seen that the refractivity distribution is uniform to within ± 20% for a radius of less than 3 cm., at the vertical nozzle station 16.8 cm. downstream of the nozzle exit.

A calculation of the expansion fan originating from the lip of the nozzle exit was undertaken to discover whether the lowered refractivity at the flow edges could be explained by the presence of this expansion. The following assumptions were made for this calculation:

(i) The expansion fan from the nozzle end is a steady expansion fan. Support for this assumption lies in the fact that the vertical slit interferogrammes show the reduction in refractivity at the flow edges to be steady for the time between the passage of the secondary shock and the contact surface.

(ii) Perfect gas equations can be used for this calculation. It will be shown, in a later section in this chapter(sections 5.5.5 and 5.5.6) that the test section air flows are expected to be frozen and that the ionisation fraction in the test section argon flows is very small. Test section flows of both gases may therefore be approximated by perfect gas flow. An important result of the fact that no significant reactions can take place in the expansion is that the specific refractivity is constant throughout the test section.

(iii) The expansion can be approximated by a Prandtl-Meyer expansion. A perfect gas Method of Characteristics calculation of an axisymmetric expansion shows that the density (refractivity) distribution in the expansion differed only slightly from the corresponding Prandtl-Meyer expansion at the vertical slit nozzle station.

(iv) The physical properties of the gas entering the Prandtl-Meyer expansion are those for the gas at a nozzle area ratio of 12(i.e. the area ratio of the nozzle exit). Also, the gas is assumed to be flowing parallel to the nozzle axis along the whole of the upstream edge of the expansion

Fig. 5.16. Refractivity distribution in a plane perpendicular to the flow direction - AIR SHOTS. The points are derived from two different scans of the vertical slit interferogrammes. The times at which the scans are taken, measured after the arrival of the primary shock at the vertical slit station, are:

2"Hg Air : □ 25 sec., × 35 sec.

1"Hg Air : □ 25 sec. × 36 sec.

Radius is measured from the nozzle symmetry axis.

——— Theory of uniform core of test gas terminated by a Prandtl-Meyer expansion. The rise at 9cm. is due to the shock on the window.

– – – The oblique shock on the valve sleeve.

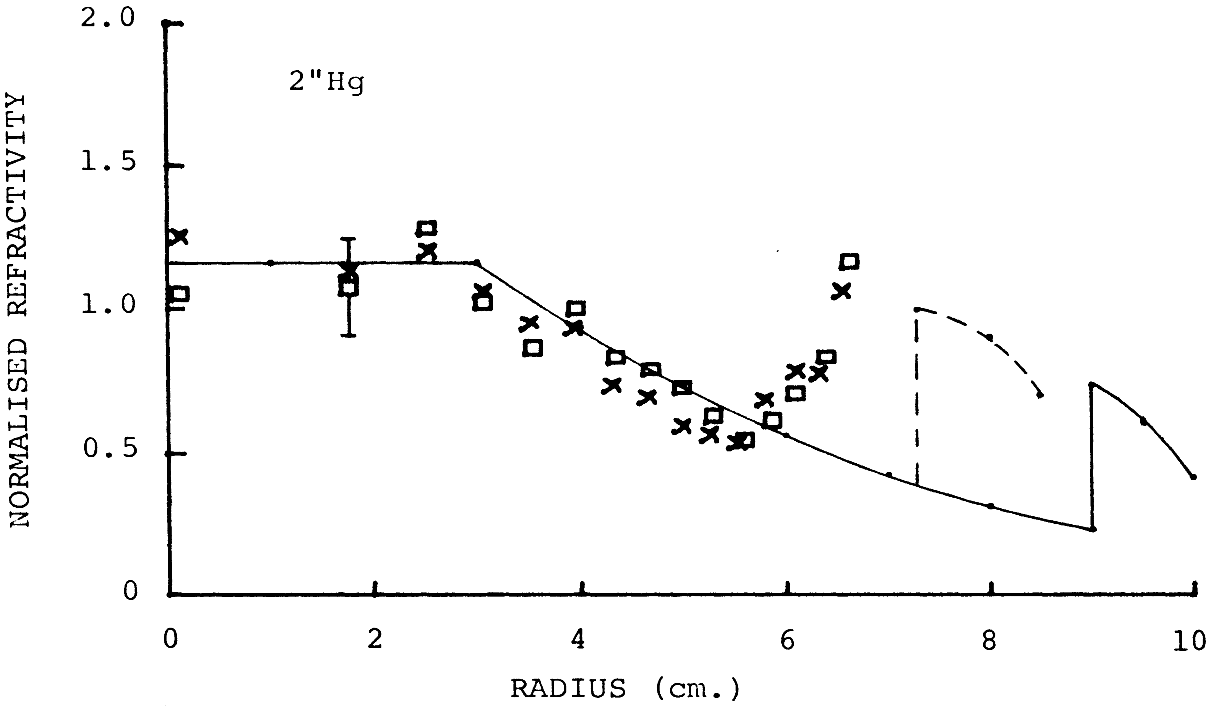

2.0
1.5
1.0
0.5
0
2"Hg
NORMALISED REFRACTIVITY
0
2
4
6
8
10
RADIUS (cm.)

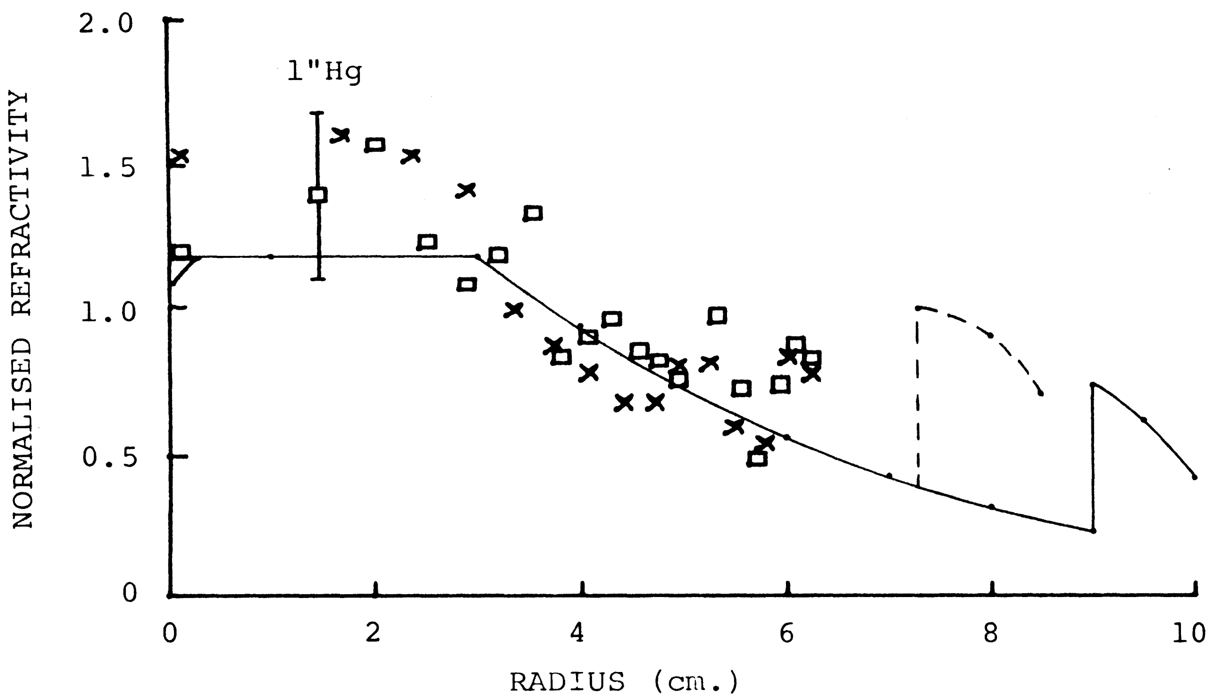

2.0
1.5
1.0
0.5
0
1"Hg
NORMALISED REFRACTIVITY
0
2
4
6
8
10
RADIUS (cm.)

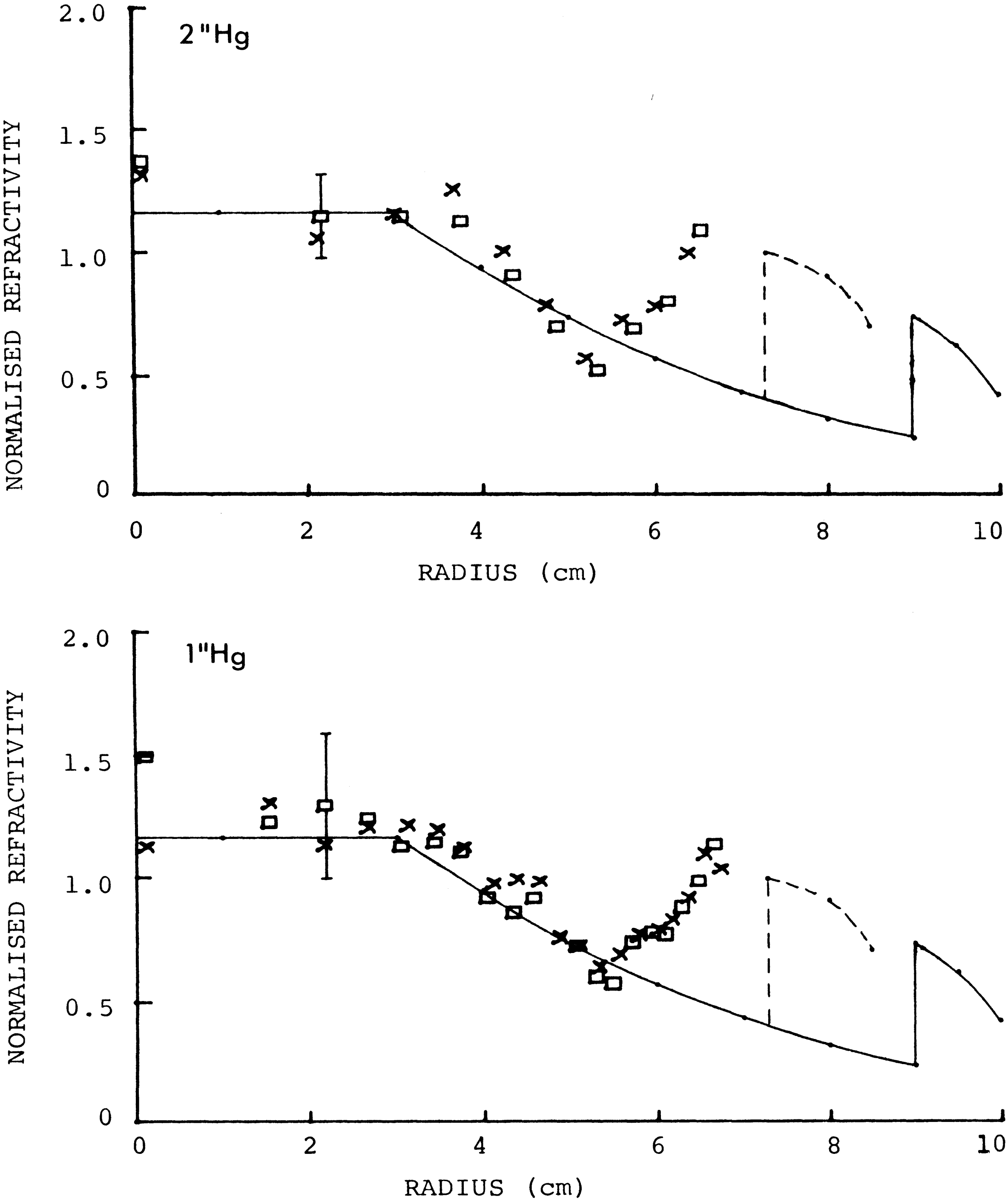

Fig. 5.16. (Cont.) Refractivity distribution in plane perpendicular to the flow direction - ARGON SHOTS. (see previous page for details).

Scan times:

2"Hg Argon: □ 27 μsec., × 33 μsec.

1"Hg Argon: □ 30 μsec., × 38 μsec.

fan. This approximation should be reasonable, although it may lead to an underestimation of the width of the undisturbed region of flow and to an overestimation of the ratio of the core density to the densities on the expansion fan. In fact, between the lip of the nozzle exit and the uniform flow region in the test section, it is expected that the Mach Number will increase by 10%, the flow angle will change from 5° to 0° to the axis and the density will drop by 25%.

The ambient pressure outside the test gas flow in the test section was taken to be 20 times the prior steady flow static pressure. This may still underestimate the ambient pressure, considering the fact that the starting shock system is travelling ahead of the steady test flow and may have boosted the ambient pressure. In any event, at the station of interest, the density distribution in the expansion is very insensitive to the ambient pressure outside the test flow. The divergence of the expansion fan is large even when the ambient pressure is high. The result is that the expanding flow runs into the windows and the valve sleeve. To estimate how far the resulting oblique shock waves extend into the flow and how the density is affected by these shocks, a perfect gas method of characteristics calculation was made of the shocks.

The distribution of density (refractivity), $\rho/\rho_{ref}(r)$, across the flow at the vertical slit nozzle station, predicted by the Prandtl-Meyer expansion and oblique window shock calculations, is shown in Fig. 5.16 together with the refractivity (density) distribution derived from the vertical slit interferogrammes. The reference density for the predicted curve is given by

$$\rho_{ref} \equiv \frac{1}{2\text{x}7.62}\int_{-10}^{+10} \rho dr \qquad \ldots(5.5\text{-}1)$$

ρ_{ref} is the density required, over a path length of 2 x 7.62 cm., to produce the same fringe shift as that produced by the predicted density distribution, $\rho(r)$, over a full path length between the test section windows (2 x 10 cm.). ρ_{ref} is therefore the theoretical equivalent of the reference density used to normalise the density distribution derived from the vertical slit interferogrammes.

Fig. 5.16 shows that to within experimental error, (±20%), the theory and experiment agree, for radii less than 5.5 cm. There are two possible reasons for the rise of the experimentally derived refractivity at radii greater than 5.5. cm. The first and most likely explanation is that, at large radii, the assumption of axisymmetry, used in the derivation of the experimental refractivity, breaks down. Perpendicular to the flow direction the flow is restricted by the non-axisymmetric configuration of the valve sleeve and windows (see diagram in Fig. 4.2). The second possible explanation is that the intrusion into the flow of the oblique shock in the valve sleeve has been underestimated by the flow calculation and that this intrusion has raised the fringe shift at the larger radii.

In conclusion, the vertical slit interferogrammes show that the test section flow consists of a uniform flow terminated by an expansion from the truncated nozzle end.

5.5.5. THE PHYSICAL AND CHEMICAL PROPERTIES OF THE STEADY AIR FLOWS.

The physical and chemical properties of the test section flows in air were calculated with the aid of two computer programmes - ESTC and NFAPC (see appendices B and C). ESTC calculated the equilibrium post shock conditions in the tube. NFAPC, using the results of the ESTC calculation as input, calculated a one-dimensional non-equilibrium expansion of the gas through the nozzle. The reaction rates used by NFAPC are those quoted by Lordi et. al. (1966).

The results of the nozzle flow calculations are summarised in a series of graphs in Figs. 5.17 to 5.19. The first graph shows the equilibrium and non-equilibrium nitrogen dissociation fraction as a function of nozzle area ratio. The recombination of nitrogen is seen to freeze at an area ratio of between 2 and 6 over the whole range of conditions. Oxygen is completely dissociated over the whole range of conditions. The electron and (NO^+) number density is always less than 0.01 times the oxygen atom number density. From the 2"Hg to the 1/8"Hg condition the nitrous oxide number density decreased from 0.1 to 0.01 times the oxygen atom number density.

The second graph shows the flow Mach Number vs. the nozzle area ratio. The Mach Number is that based on the NFAPC speed of sound defined in equation (3.2-9). (See the

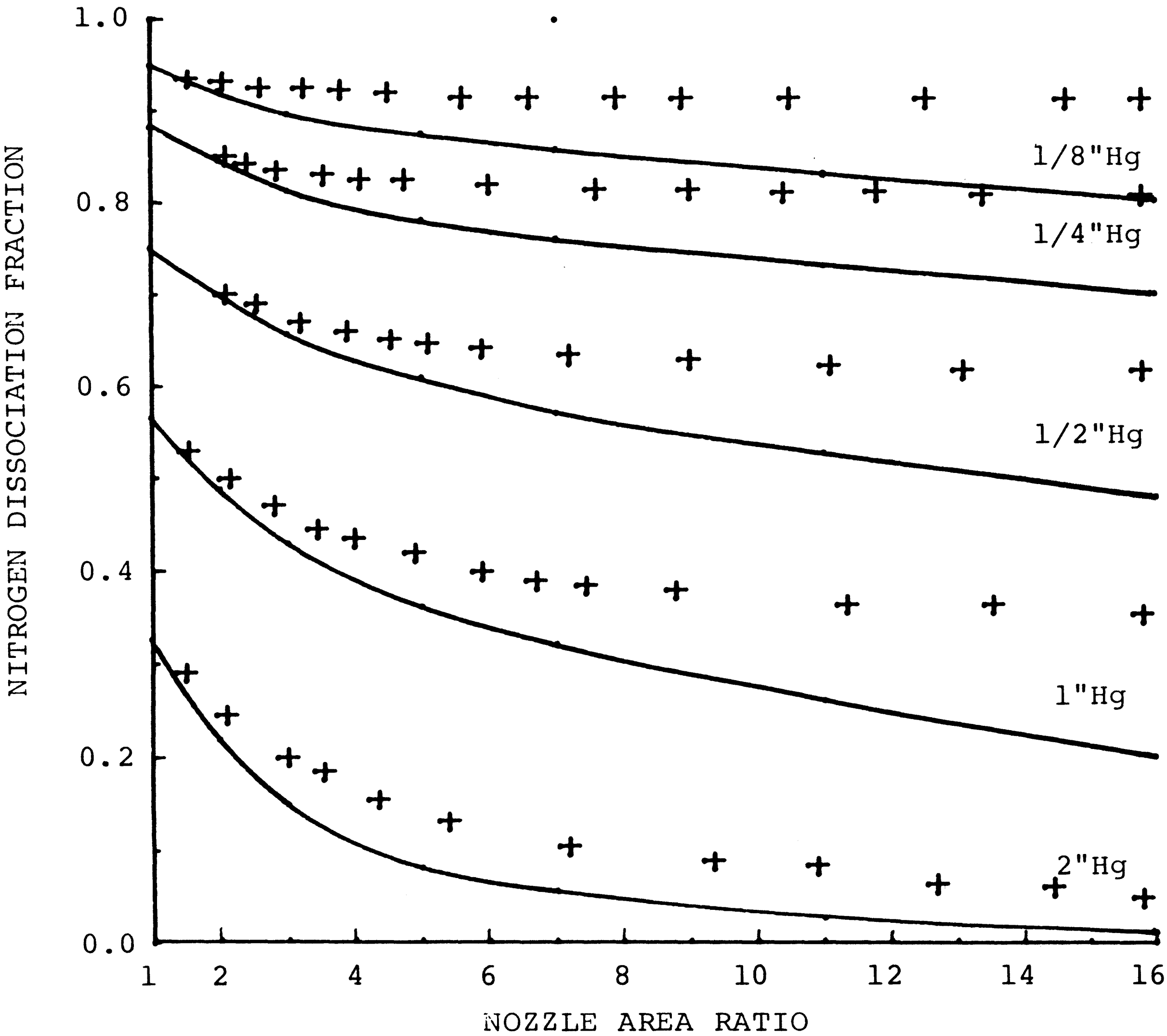

Fig. 5.17. Nitrogen dissociation fraction vs. nozzle area ratio.

+ nonequilibrium chemistry

——— equilibrium chemistry

The shock tube initial pressures are shown with the relevant equilibrium curves.

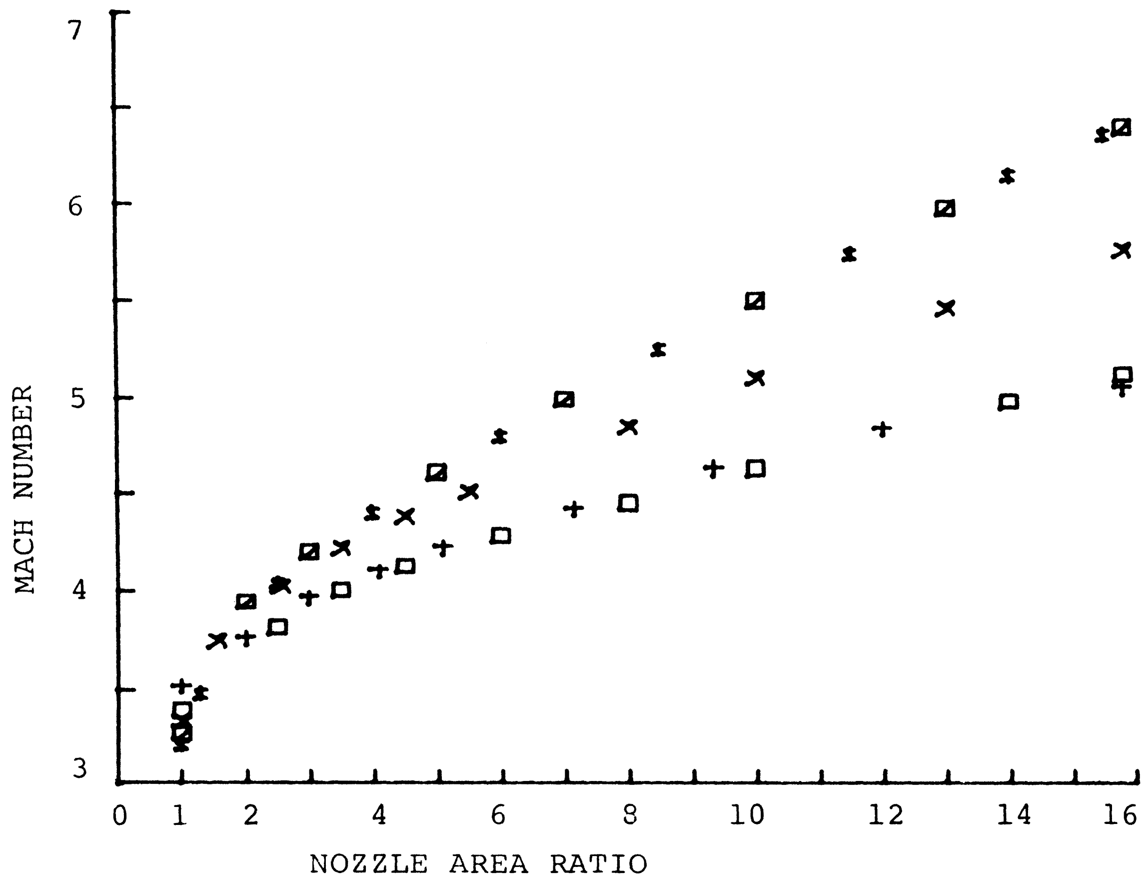

Fig. 5.18. Mach Number (from NFAPC computer programme) vs. nozzle area ratio. - AIR SHOTS. Initial shock tube pressures:

+ 2"Hg., □ 1"Hg., ✕ 1/2"Hg

⊠ 1/4"Hg., ✱ 1/8"Hg.

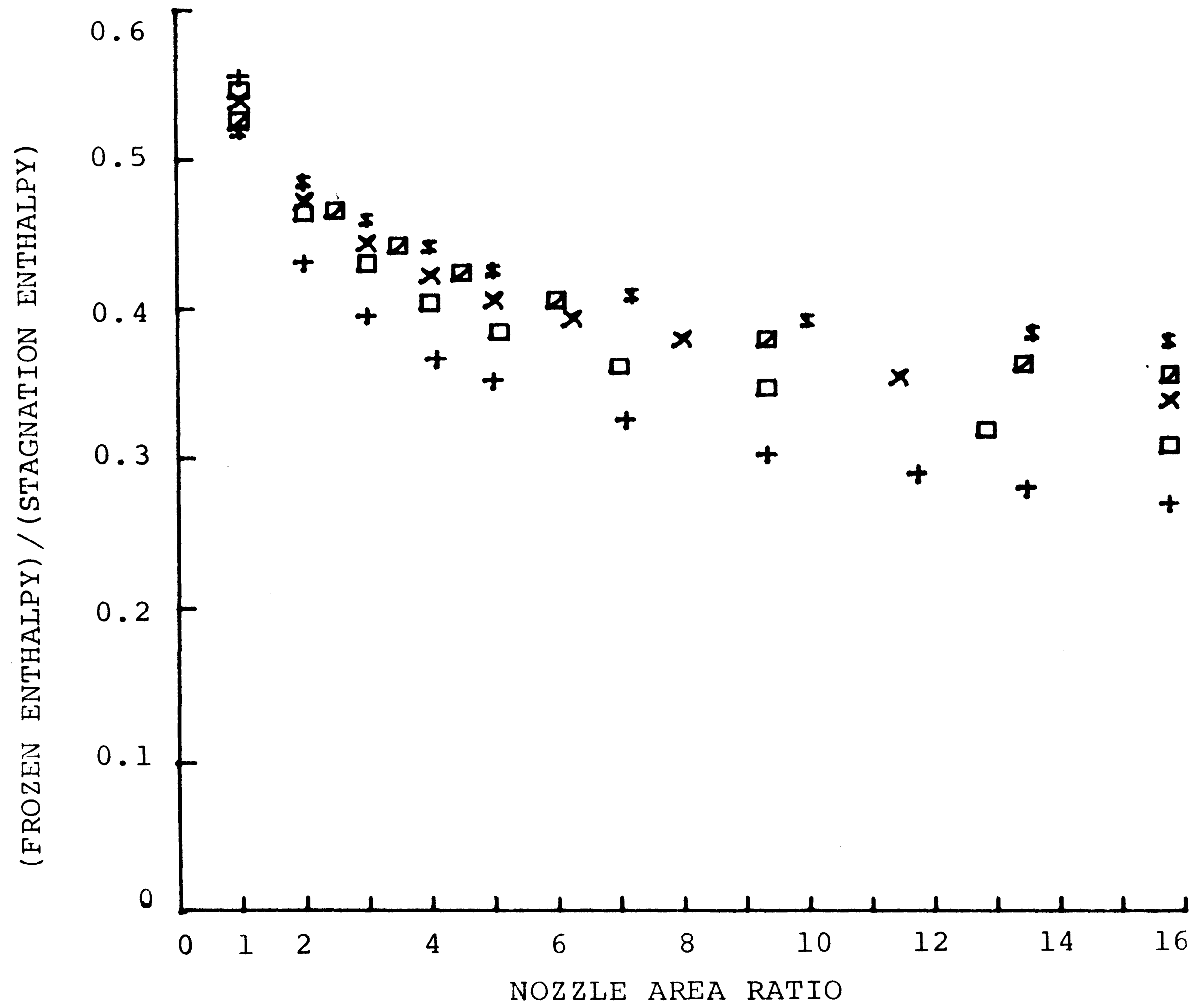

Fig. 5.19. (Frozen enthalpy)/(stagnation enthalpy) vs. nozzle area ratio - AIR SHOTS. Initial shock tube pressures:

+ 2"Hg., □ 1"Hg., ✕ 1/2"Hg.,

⊠ 1/4"Hg. $ 1/8"Hg.

chapter on nozzle design for a discussion of sound speeds). A nozzle area ratio of 16 appears to be sufficient to generate flows of Mach Number $\geqslant 5$ in the test section.

The third graph shows the variation of frozen enthalpy in the flow as a function of nozzle area ratio over the range of conditions. The stagnation enthalpies for the five conditions between 2"Hg and 1/8"Hg are 27, 36, 47, 60, and 68 MJ/kg. In the test section, between 60% (for the 1/8"Hg case) and 75% (for the 2"Hg case) of this enthalpy is in the form of kinetic energy, compared with 45% behind the primary shock in the tube.

Once the physical and chemical properties of the steady test section flow have been calculated, a comparison of predicted refractivity can be made with experiment. To calculate the integrated refractivity across the centre of the flow, the theoretical density and specific refractivity at a nozzle area ratio of 16 was used with the normalised density distribution calculated in the last section and shown in Fig. 5.16.

The expression used for the fringe shift over a path length l (cm), between a vacuum and the test section air flow, density ρ (gm/cm^3)

$$\Delta F_v = \rho l \left[\frac{1\mathrm{x}10^8}{\lambda} \sum_j \gamma_j M_j K_j - 2.70\mathrm{x}10^2 \gamma_e \lambda \right] \qquad \ldots(5.5\text{-}2)$$

j ranges over the following species in the flow: N_2, O_2, Ar, N, O, NO, NO+.

γ_j = (moles of j)/(gm. of gas mixture)

M_J = Molecular weight of species j

λ = wavelength of light in the ~~initial~~ interferometer experiments (5100 Å here)

K_j = specific polarisability of species j

A table of the specific polarisabilities, K_j, is shown for the constituents of the air flows in Fig. 5.20. The expression for the refractivity of the electrons is taken from Meier (1973).

The results of the calculation of the fringe shifts across the flow centre line are shown with the results of the fringe shift measurements in Fig. 5.13. The comparison shows a fair agreement between the calculated and measured fringe shifts for shots with initial pressures of 1/2"Hg and less.

SPECIES	SPECIFIC POLARISABILITY K_j $(cm^3 gm_j^{-1})$	WAVELENGTH AT WHICH K_j WAS MEASURED
N_2	0.237	5893
O_2	0.193	5893
N	0.31	5446
O	0.18	5446
Ar	0.141	5893
NO	0.21	—
NO^+	0.21	—

Fig. 5.20. Table of the specific polarisabilities of the constituents of the air flows, taken from Gaydon and Hurle (1963). The specific polarisabilities of NO and NO^+ have been taken to be the mean of those for N_2 and O_2.

For the 1"Hg and 2"hg shots, however, the theory overestimated the fringe shift. This discrepancy may be due to the presence of the nonsteady expansion wave.

5.5.6. THE PHYSICAL AND CHEMICAL PROPERTIES OF THE STEADY ARGON FLOWS.

The proceedure, used for the air shots, of calculating an equilibrium normal shock followed by a non-equilibrium nozzle flow, lead to predictions of fringe shifts in the argon shots which are far too low. Indeed, for initial shock tube pressures of 1/2"Hg and less, the predicted fringe shift is negative, although the observed fringe shift is positive. This suggests that the electron concentration in the flow is overpredicted by the theory.

Shock tube studies at the ANU (Meier (1973), Horn, Wong and Bershader (1967) and Oettinger and Bershader (1967)), have shown that, for high shock Mach Numbers, considerable energy loss occurs from the post shock gas through radiation. In his model, Meier assumes that the post shock flow is one-dimensional, reaches chemical equilibrium before it begins to radiate, stays in chemical equilibrium as the plasma decays and that the radiation is the only form of energy loss from the system. The conservation of mass, momentum and species is then employed, along with the equation of state and the Saha Equation to produce a unique set of states through which the gas passes as it loses its energy. Meier then shows that his model successfully predicts the decay path of his argon plasmas in the electron number density - atom number density plane. The rate of decay is not discussed in Meier's thesis although some experimental results are given for the time at which the plasmas reach certain states.

To calculate the rate at which the energy is lost from the shock tube slug through radiation, a simplified version of the radiation loss rate models of Horn et al (1967) and Oettinger and Bershader (1967) was employed. The simplified model treats the plasma as optically thin at all frequencies although some allowance is made for the reduction of loss rate due to the optical thickness of plasmas in the region of the spectral line frequencies. The number of spectral lines considered in the simplified model is much less than the number considered by Horn et al, and Oettinger and Bershader. Horn et al considered that Bremsstrahlung and radiative recombination are the main processes giving rise to continuum radiation from an argon plasma at moderated temperatures ($11000^{\circ}K$). The expression they give for the energy loss rate from an optically thin plasma is

$$Q_c = A\, Z_{eff}^2\, N_e^2\, T^{-1/2}(\nu_g + \frac{kT}{h}) \qquad \ldots(5.5\text{-}3).$$

where $A = \dfrac{64\, e^6 \pi^{3/2}}{3\, (6)^{1/2} m_e^{3/2}\, k^{1/2}\, c^3}$

e = electronic charge,
m_e = electron rest mass,
k = Boltzmann's Constant,
h = Planck's Constant,
N_e = electron number density,
T = temperature,
ν_g = I_g/h

where I_g = ionisation potential of electronic level to which electron falls in a free-bound transition.

Horn et al found, for their shock conditions, ($M = 16.3$ and p_1 = 3m/mHg, 5m/mHg), that I_g = 2.85eV (4p level) and $Z_{eff}^2 = 1.5$ gave good agreement with experiment. Another of Horn et al's results was that continuum radiation and line radiation contributed roughly equally to the energy loss. They also concluded that the 3d4p and 4p4s transitions accounted for between 60% and 75% of the losses due to line radiation.

Oettinger and Bershader give the following expression for the energy loss rate from a small element of gas due to the bound-bound transitions

$$Q_b = \frac{(\alpha\rho)^2 \; h^3 \; \exp(I/kT)}{2\; m_a^2 \; (2\pi m_e kT)^{3/2} \; Q_i(T)} \sum_{q,p} M_{q,p} \exp(-E_{p,0}/kT) \qquad \ldots(5.5\text{-}4)$$

where α = ionisation fraction = $N_e/ (N_e+N_a)$,

ρ = mass density,

I = ionisation potential of atom in the ground state,

m_a = mass of atom,

$Q_i(T)$ = electronic partition function for the ion $\simeq 4 + 2 \exp(-2060/T)$,

$E_{p,q}$ = potential energy difference between the p and q electronic levels in the atom (q=0 denotes the ground state of the atom),

$M_{q,p}$ = a constant for the q,p transition.

N.B. Consistent with the assumption of thermodynamic and chemical equilibrium in the gas during the time in which radiation occurs, the electrons are assumed to have the same temperature (T) as the heavy particles. This assumption has been implemented in the above equations where T has replaced the electron temperature.

On the basis of the results of Horn et al, only the 3d4p and the 4p4s bound-bound transitions were considered in the simple model. The $M_{q,p}$ for these two transitions were determined by a process of trial and error in which the simplified model was forced to fit the experimental results of Horn et al, Oettinger and Bershader and Meier. Values of M'_{3d4p} =

1.44×10^{-3} and $M'_{4p,4s} = 2.57 \times 10^{-3}$ erg/sec were found to provide a good fit to the experimental results. The dash superscript ($'$) here denotes, firstly, that the losses due to other spectral lines have been included in the constants for the two lines considered, Secondly, Horn et al and Oettinger and Bershader consider the plasma to be optically thick in the spectral lines and carry out an invloved calculation to take account of this. In the simple model used here, the losses through the spectral lines have been treated as if the plasma was optically thin at the relevant frequencies. However, because the $M^{1}_{q,p}$ were obtained from a fit to the experimental results, the reductions in the energy loss rates due to the optical thickness are partly included in these constants.

The variation of ionisation fraction at a point fixed in the laboratory, with time after the passage of the primary shock, according to the simplified energy loss model, is shown in Fig. 5.21. Shown in Fig. 5.22 is the time variation of the stagnation enthalpy flow as a percentage of the original (i.e. pre-radiation) stagnation enthalpy. This last graph illustrates one of the advantages of the non-reflected shock tunnel - no matter how severe the radiation energy loss from the test gas, at least 45% of the stagnation enthalpy is in the form of kinetic energy and therefore cannot be lost from the flow. The original stagnation enthalpies were 15, 20, 26, 33, and 38 MJ/kg for the five shock conditions with initial shock tube pressures between 2'Hg and 1/8"Hg.

The post primary shock gas property variation model just described was applied to the shock tunnel problem in the following way. Firstly, ESTC was used to find the equilibrium gas conditions behind the primary shock assuming no radiation loss. Meier (1973) and Wong and Bershader (1966) show experimentally that no loss chemical equilibrium conditions are attained behind shocks in argon. Secondly, the energy loss rate model was used to give the variation of gas properties with distance behind the primary shock. In doing this, it was assumed that chemical equilibrium was reached immediately behind the shock. Wong and Bershader show that there may in fact be a non-equilibrium region of significant proprtions. The approximation will therefore lead to an overestimation of the extent of the plasma decay at any point behind the shock. Finally, the test section flows resulting

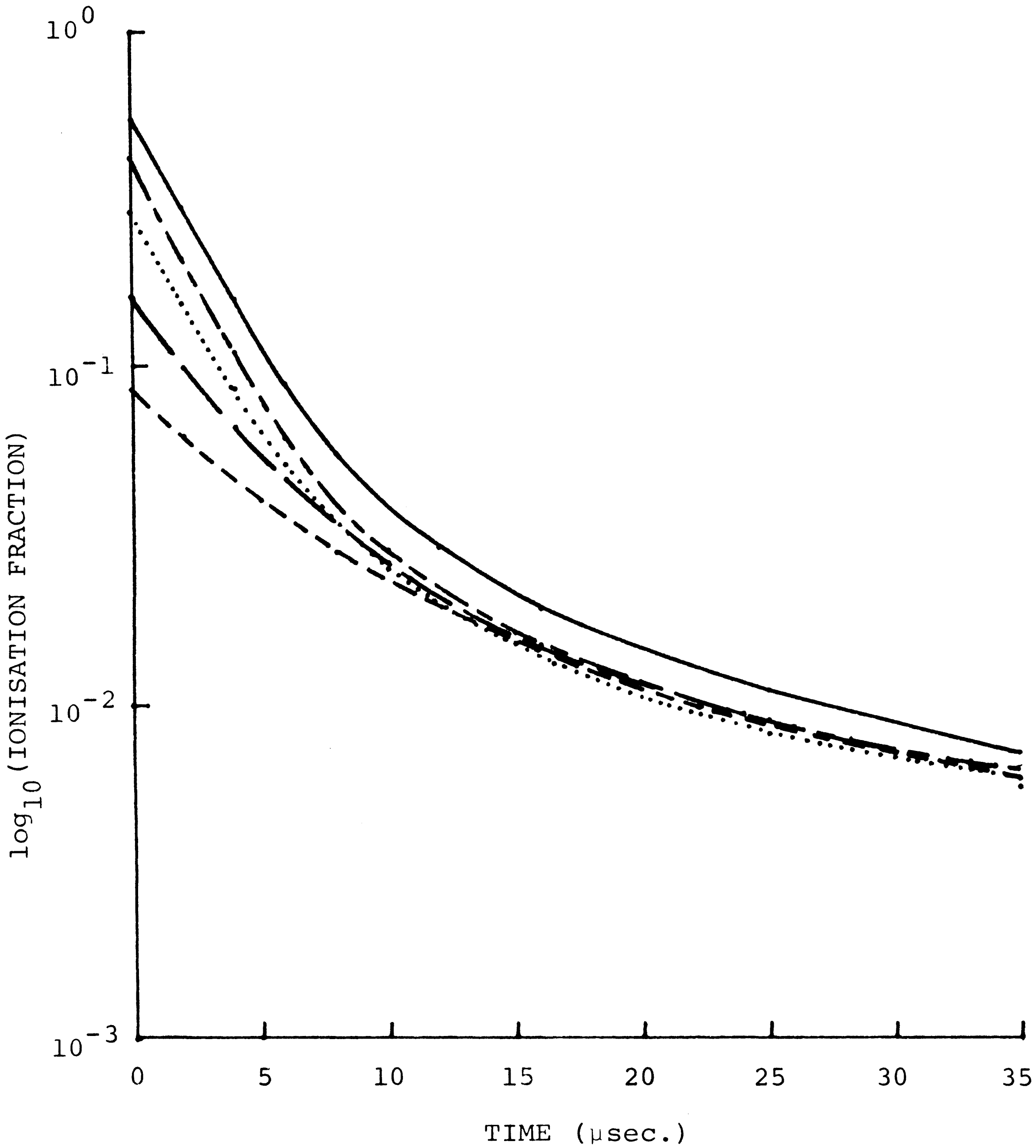

Fig. 5.21. Argon ionisation fraction at a shock tube station vs. laboratory time after the arrival of the primary shock at that station.

——— 1/8"Hg., — – — – 1/4"Hg., ... 1/2"Hg.,

— — — 1"Hg., – – – – 2"Hg.

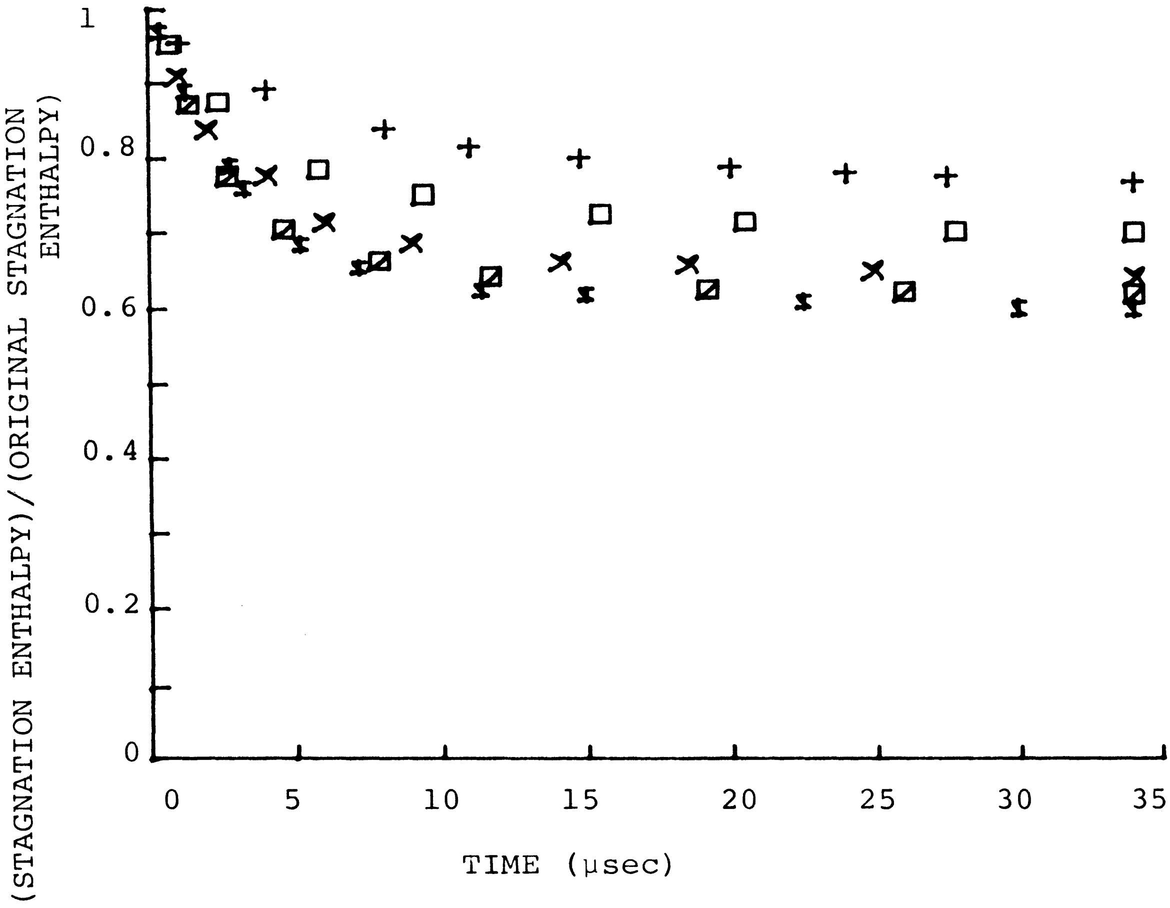

Fig. 5.22. Variation of stagnation enthalpy of ARGON at a shock tube station with laboratory time after passage of primary shock in the tube.

Initial shock tube pressures:

+ 2"Hg., □ 1"Hg., × 1/2"Hg., ⊠ 1/4"Hg., ⁑ 1/8"Hg.

from the various post shock conditions were calculated with NFAPC. No radiation loss was assumed to occur in the nozzle flow. Upon entering the nozzle, the gas cools rapidly and the electron concentration drops sharply in response. Also for the important second half of the tube slug, the time spent in the nozzle is short compared with the time spent behind the primary shock. The reaction rates from Wong and Bershader (1966) for the argon nozzle flows are shown in the table in Fig. 5.23 in an Arhennius form.

Plots of the resulting changes of ionisation fraction with nozzle area ratio are shown in Fig. 5.24 for the 2"Hg, 1/2"Hg and the 1/8"Hg argon shots. The curves for both equilibrium and non-equilibrium flows are shown in this figure. For each of the three shock conditions, the curves for two nozzle entrance gas conditions are shown. The curves with the higher initial ionisation fraction are those which result from the steady expansion of the equilibrium post shock gas before any energy losses occur from the gas. The curves with the lower ionisation fraction arise from the expansion of post shock gas which has been allowed to decay. The time at which these decayed gas conditions arrive at the nozzle entrance, after the arrival of the primary shock, is shown for each curve. In each case, the gas which expands to produce the steady flow in the test section arrives at the nozzle entrance after any of the gas conditions for which curves are given. It will be noted from Fig. 5.24 that the test section ionisation, for the decayed flows, is very small in all cases. The steady test section flows can therefore be expected to contain few free electrons. Fig. 5.24 shows also that the ionisation fraction curves for the non-equilibrium flows differ only slightly from those for the equilibrium flows. For this reason, the less time consuming equilibrium flow calculations were used for the predictions of the test section fringe shift.

The change in (frozen enthalpy)/(stagnation enthalpy) with nozzle area ratio is shown in Fig. 5.26 for the 2"Hg, 1/2"Hg and 1/8"Hg shocks for several degrees of decay of the post shock plasma. The laboratory times at which these gas conditions occur after the passage of the primary shock are marked on the curves. Reference should be made to Fig. 5.22 which can be used to calculate the stagnation enthalpy for

REACTION	THIRD BODY M	REACTION RATE CONSTANT (cm^3 $mole^{-1}$ sec^{-1})
$Ar+M \rightleftarrows Ar^+ + e^- + M$	Ar, Ar^+	$1.61 \times 10^2 T^2 \exp\left(\frac{-3.629 \times 10^5}{R_c T}\right)$
$Ar+e^- \rightleftarrows Ar^+ + e^- + e^-$	—	$1.26 \times 10^{17} T^{-1} \exp\left(\frac{-3.629 \times 10^5}{R_c T}\right)$
$Ar+e^- \rightleftarrows Ar^+ + e^- + e^-$	—	$8.9 \times 10^{12} T^{0.65} \exp\left(\frac{-2.66 \times 10^5}{R_c T}\right)$

Fig. 5.23. The reaction scheme and rates for the argon nozzle flows. The rates were taken from Wong and Bershader (1967) and were converted into an Arrhenius form for input to the nozzle flow programme NFAPC. $R_c = 1.98$ cal $mole^{-1}$ $^oK^{-1}$.

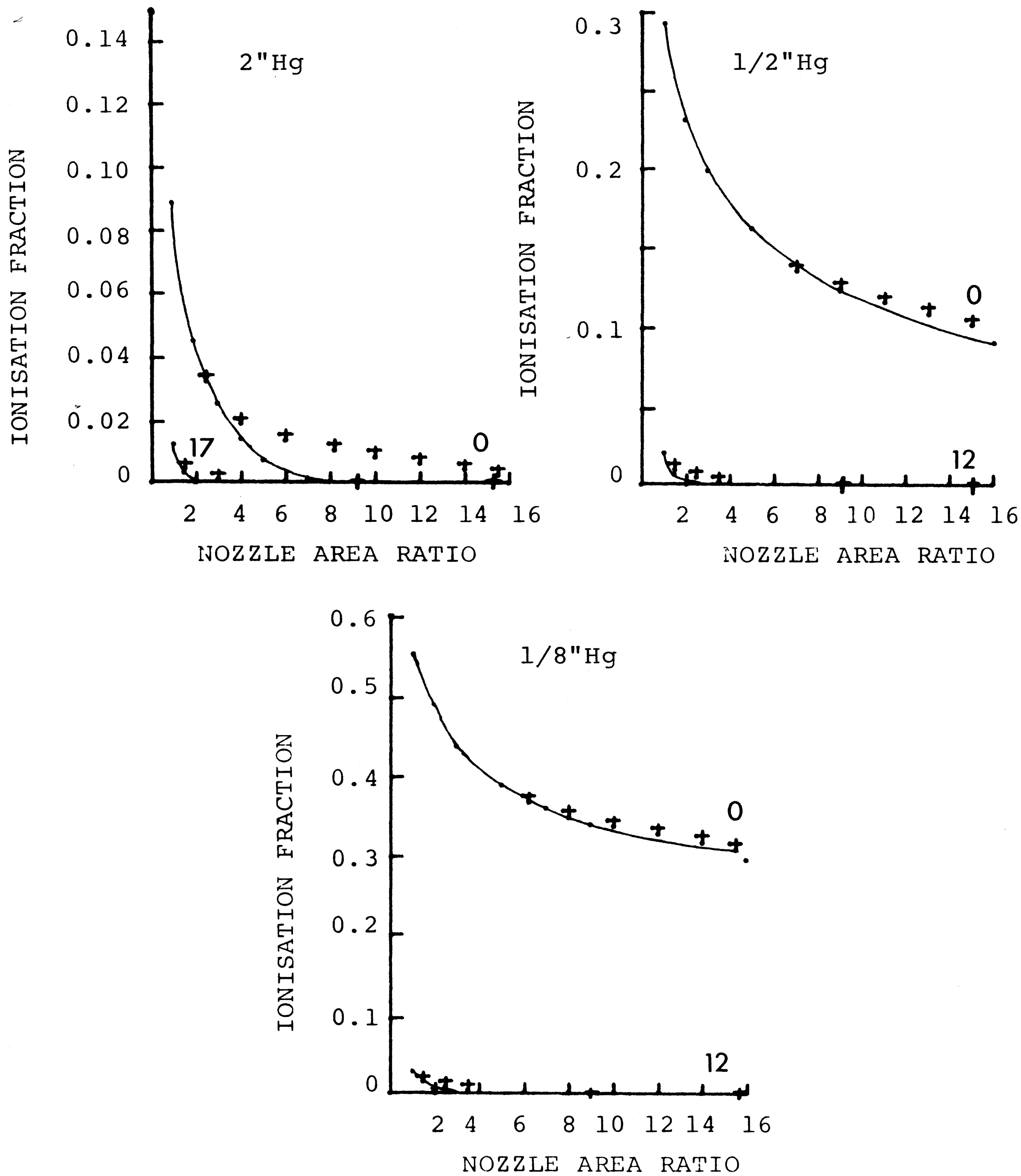

Fig. 5.**24.** ARGON ionisation fraction vs. nozzle area ratio. Laboratory time at which the initial gas conditions, for each curve, appear at the nozzle entrance, after the arrival of the primary shock at entrance, is shown with the curve in μsec.

______ equilibrium chemistry in nozzle.

\+ nonequilibrium chemistry in nozzle.

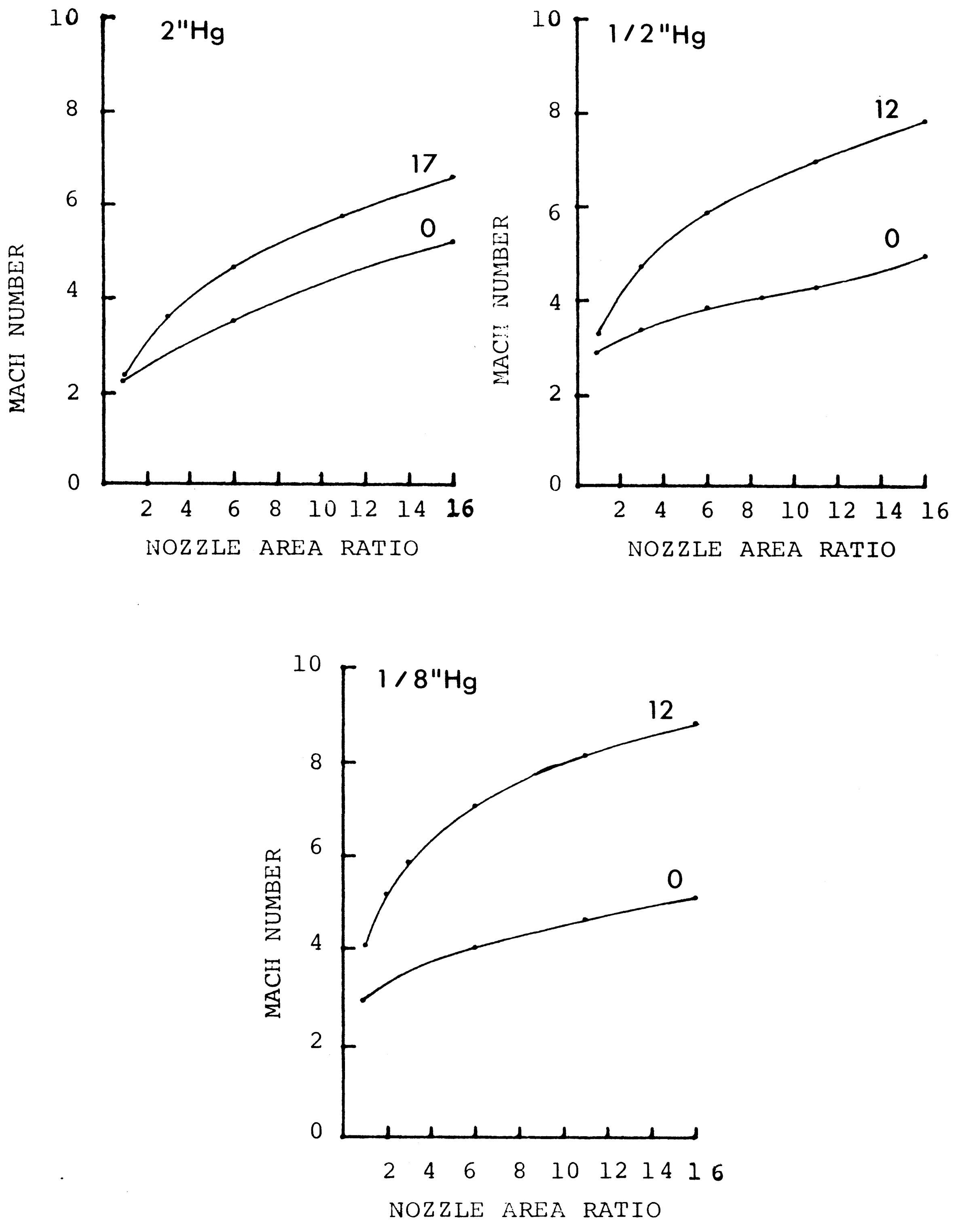

Fig. 5.25. Mach Number vs. nozzle area ratio - ARGON SHOTS. Laboratory time at which the initial gas conditions, for each curve, appear at the nozzle entrance, after the arrival of the primary shock at the entrance, is shown with each curve in μsec.

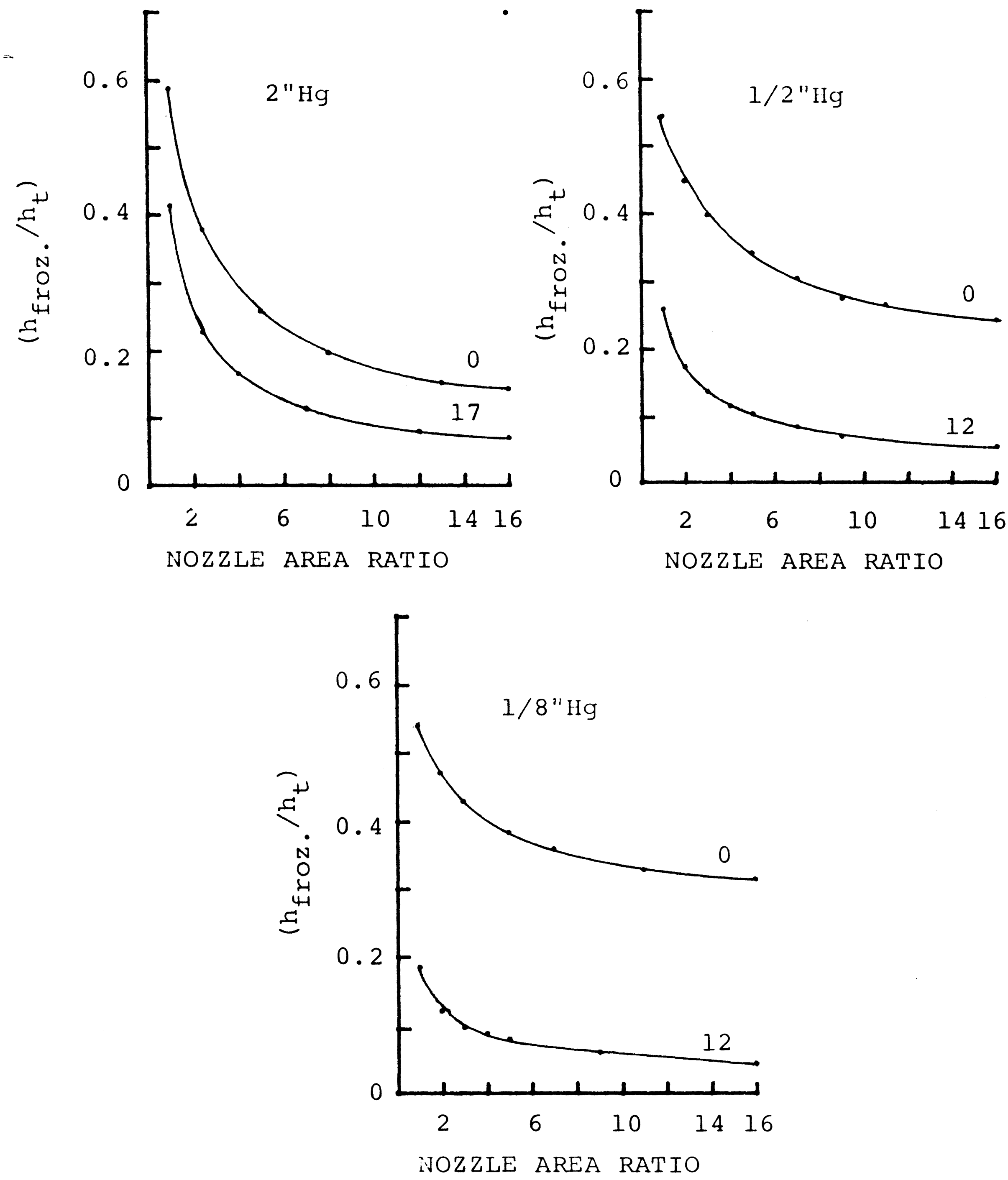

Fig. 5. 26. (Frozen enthalpy)/(stagnation enthalpy) vs. nozzle area ratio for ARGON. Shock tube initial pressures are shown on the graphs. Also shown are the decay times for each curve in μsec.

each of these decayed conditions. Fig. 5.25 shows the variation of Mach Number with nozzle area ratio for the gas conditions of Fig. 5.24.

The predicted fringe shifts across the flow centre are shown with the experimental fringe shifts in Fig. 5.13 for the range of shock conditions. The expression for fringe shift over a path length l(cm.) from a vacuum to an argon flow of density ρ (gm/cm^3) is the one given by P. Meier:

$$\Delta F_V = \rho l(5.61\times10^7(\gamma_A \times 11.08 + \gamma_{A^+} \times 7.4)/\lambda - 2.70\times10^2 \gamma_e \lambda)$$

Only the argon atom (A), the singly charged argon ion (A^+) and the electron (e^-) have been considered as the constituents of the argon flows. The expansion fan from the end of the nozzle was calculated in the same way as for the air shots (see section 5.5.4 in this chapter).

The predicted fringe shifts, shown in Fig. 5.13, agree well with experiment for the 2"hg and 1"Hg shots but are too high for the lower pressure shots. This is in contrast to the air shots where agreement is good for the lower initial pressure shots and the fringe shift for the higher initial pressure shocks is overestimated. For the argon shots, it may be that energy losses in the shock tube are overestimated. For all conditions the experimental steady flow fringe shift lies between the values predicted using the simplified energy loss rate model and the values predicted assuming no radiation energy losses occur.

5.5.7. BODY FLOWS.

The experiments in which the luminosity of the shock layer on a cylinder was monitored with the ICC have been used earlier in this chapter (section 5.3) to obtain a measure of the primary shock and contact surface arrival times. They may also be used to give an indication of the time required for the establishment of a steady flow on the cylinder and therefore whether a steady cylinder flow can be established before the arrival of the contact surface. A constant standoff distance is a necessary condition for a steady flow on a cylinder. A survey of the records of the shock layers shows that, for all shock conditions, the cylinder flow has not become steady before the arrival of the of the contact surface. Two examples of the shock layer records are shown in Fig. 5.5.

In order to observe body flows on a double wedge and a flat plate, a number of interferogrammes were taken with the ICC in the framing mode (see Chapter 4, section 4.4.9). Unfortunately, due to the large distance betwen the shock tube photodiode station, used to trigger the equipment, and the cylinder and to the scatter in the shock speeds (see section5.1 in this chapter) it was not possible to say with certainty whether the interferogrammes were taken during the time of steady test gas flow in the free stream for the bodies. Many of the interferogrammes did show a steady flow on the wedge and flat plate, but this flow may have been the driver gas flow.

It seems likely that a steady test flow could be established on the wedge and flat plate. Whether the steady flow seen on the interferogrammes was the test or the driver gas flow, it became established in a time of the order of the steady test section nozzle flow time.

5.6.EMISSION AND ABSORPTION SPECTRA.

5.6.1. EMISSION SPECTRA.

A large number of spectral lines were resolved by the spectrograph in the emission monitoring experiments. In Fig. 5.27 plots of the distribution of the stronger spectral lines, across the frequency range observed, is shown for an air and an argon shot. The strength of the lines, relative to the other lines on the same spectra, is indicated by the relative heights of the lines.

The first thing to note about the spectra is that, except for **three** lines in the argon shot spectra the two experimental spectra are identical. This fact suggests that the spectral lines are due to the presence of contaminants in the flow and not to the argon or the air. Shown in Fig. 5.26, with the experimental spectra, are the spectral lines for neutral Fe and neutral Cd (from Moore,(1959)) It can be seen that for each line in the experimental spectra a corresponding line appears in the Fe or Cd spectra. The spectra of Ar, Ar^+, O, O^+, N, N^+, Al, C, Ca, Ca^+, Cr (all from Moore (1959)) and O_2 (Gaydon and Hurle(1963)) were also considered but none of these bore any resemblance to the experimental spectra. The spectrum from neutral Ar is shown in Fig. 5.27 to show to what extent it differs from the

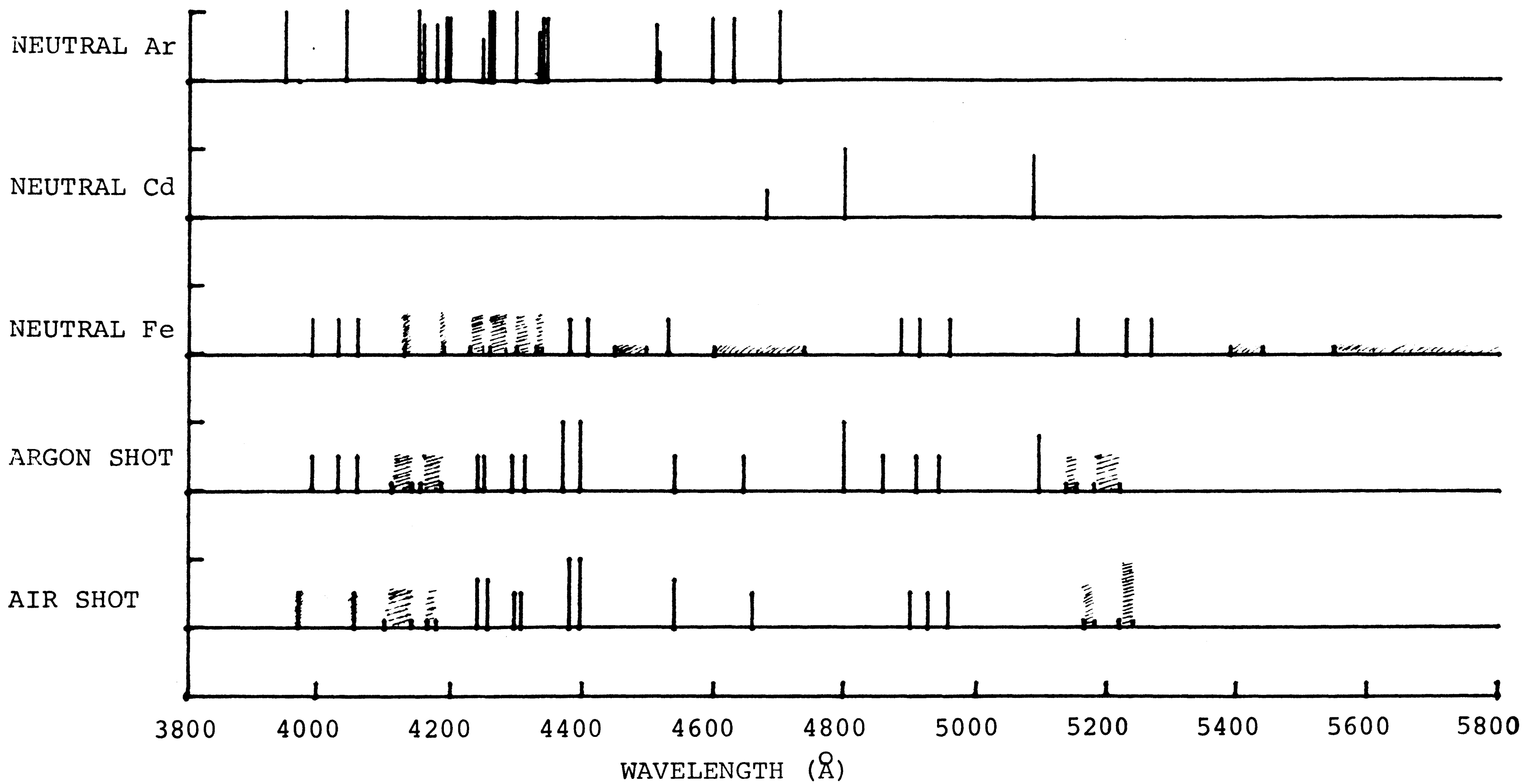

Fig. 5.27. Distribution of the stronger spectral emission lines from the shock layer on a cylinder for an air and an argon shot. Also shown are the spectra for neutral Fe, neutral Cd and neutral Ar. The line height indicates, approximately, the strength of the line relative to the other lines in the same spectrum. Shaded regions indicate a large number of closely spaced lines.

experimental spectra. It must therefore be concluded that the source of the strongspectral lines seen in the flows are neutral Fe neutral Cd. The Cd is thought to come from the case hardening on the conical guard at the nozzle entrance.

It was thought that the absence of shock reflection in the non-reflected shock tunnel would allow the production of a spectrally "clean" flow. Contamination of the flows by species such as Fe in the reflected shock tunnel was thought to come from the shock reflection process where the turbulence, high temperatures and densities combine to remove material from the shock tube walls.

In searching for the mechanism whereby the Fe and Cd are introduced into the flow, the fact that the spectral lines from these species are evident in the flow directly behind the primary shock must be taken into account. The theory that the contaminants originate at the diaphragm and are introduced into the hot test gas through contact surface mixing must therefore be discounted. The prior steady flow cannot be held responsible for the contamination because the spectral line pattern was the same for shots with no prior steady flow as it was for shots with a prior steady flow. The most likely theory is that the process of filling the shock tube with the test gas stirs up fine dust particles from the shock tube walls and leaves them suspended in the test gas. The primary shock then processes the dust particles along with the test gas. It seems reasonable to suppose that if the shock tube flow is spectrally clean then the shock tunnel flow will be spectrally clean in a non-reflected shock tunnel.

5.6.2. ABSORPTION SPECTRA.

The attempted identification of species in the flow from their absorption spectra met with no success. The presence of any absorption lines in the test gas was masked by the large number of spectral lines in the light from the exploding wire light source.

CHAPTER 6. CONCLUSION.

The development of a non-reflected shock tunnel as a derivative of a high enthalpy shock tube has lead to the achievement of higher stagnation enthalpies and densities than possible in a reflected shock tunnel derived from the same shock tube.

The disadvantage of the non-reflected shock tunnel is that the available test flow time is very short at the high stagnation enthalpies. In order to minimise the test time losses due to the non-steady starting processes, a steady, supersonic flow was established in the nozzle and test section prior to the arrival of the primary shock. The reduction in the initial nozzle and test section density, due to the presence of the PSF, ensures that the starting shock system passes rapidly through the nozzle and the test section. The experiments have shown that the secondary shock is always downstream of the steady (u-a) bicharacteristic originating at the nozzle throat. This confirms the predictions of the analytic and MOC calculations of the non-steady flowfield. The time for which usable test flow exists in the test section is ~~45%~~ about half of the test flow time in the shock tube.

Interferogrammes taken of the test section flow showed that the flow was approximately uniform and parallel at the lowest stagnation enthalpies. The absolute refractivities of the test section flows were, in general, less than or equal to those predicted by the steady flow calculations. The fact that, for some shots, the refractivity was below the predicted value may be due to the presence of the nonsteady expansion or, in the case of the argon shots, to an overestimation of the radiative energy losses in the gas behind the primary shock in the tube.

The body flow experiments have indicated that a steady flow could probably be established on a sharp nosed wedge of reasonable dimensions inclined at moderate incidence to the flow. The establishment of steady flow on a blunt body, where a portion of the flow is subsonic, does not seem possible in the short steady flow time.

A spectrally clean shock tube flow should produce a spectrally clean flow in a non-reflected shock tunnel.

The contamination of the flows examined here, by species such as Fe and Cd, is thought to arise from the shock tube filling processes and the presence of fine dust particles on the walls of the apparatus. The cylinder flow shock layer luminosity experiments showed a sharp division between the driver and test gases. Contamination of the test gas by the driver gas does not, therefore, appear to be a problem in the non-reflected shock tunnel.

Shock speeds of up to 8.2 km/sec. were obtained in the test gases, air and argon. For air shots where chemical reactions predominate, flows were produced with stagnation enthalpies of between 29 MJ/kg. and 60 MJ/kg. The stagnation enthalpies in argon, the representative ionising gas, were between 21 MJ/kg. and 60 MJ/kg. immediately behind the primary shock in the tube. However, radiation reduced this to the range from 15 MJ/kg, to 35 MJ/kg. For comparison, Hornung and Sandeman (1974) note an approximate upper limit of 20 MJ/kg. for their flows in argon in a reflected shock tunnel.

Collisional dissociation and ionisation proceed in the forward direction in a gas by binary collisions. The parameter $\rho_\infty d$, where ρ_∞ is the free stream density and d is a typical dimension (e.g. the test section diameter), therefore serves as an indicator of the likelihood of significant changes in the gas properties in a body flow over a distance, d, due to chemical reactions. At the 29 MJ/kg. condition in air, the value of $\rho_\infty d$ was 6.5×10^{-3} kg m^{-2}. This compares with a value of 6.8×10^{-4} kg m^{-2} reported by Stalker and Stollery (1975) for flows with the same stagnation enthalpy in a reflected shock tunnel.

APPENDIX A. PRIOR STEADY FLOW ESTABLISHMENT.

In the model for the prior steady flow establishment, the flow is sonic at the nozzle entrance and at the exit at the valve end of the test section. There is a recovery shock in the nozzle which moves downstream as the density in the test section falls (see Fig. A.1). The time taken for the recovery shock to move downstream of the test section can be calculated in the following way.

First, a number of assumptions are made in order to simplify the calculations:

ASSUMPTION 1. Sonic conditions exist at the two throats at all times.

The pressure in the dump tank is extremely small and the conditions for sonic flow at the downstream throat are met as soon as the valve opens. A pressure in the test section of less than 0.99* (the initial density in the shock tube apparatus) is sufficient to support a sonic flow at the nozzle entrance . This pressure should be quickly attained after the arrival of the expansion wave from the opening of the valve. Later in the calculations the flow will be assumed to begin after the valve has opened to approximately 35% of maximum. Sonic flow should be well established at both throats by this time.

ASSUMPTION 2. The temperature in the test section is approximately equal to the initial shock tube temperature.

The temperature of the flow which enters the nozzle and passes through the recovery shock is close to the initial shock tube temperature as the flow speed is then small. The temperature of the gas initially resident in the nozzle will fall below the initial temperature due to the expansion of the gas. However, the parameter of interest in the flow, the sound speed in the gas, has only a weak dependance on the density ($a \sim \rho^{(\gamma-1)/2}$) .

ASSUMPTION 3. The gas downstream of the recovery shock is stagnant.

The gas flow speed will be low after passage through the normal recovery shock and subsonic compression to the test section diameter.

ASSUMPTION 4. The time for the recovery shock to travel along the parallel section of the channel is small compared with the time for the shock to reach the parallel section.

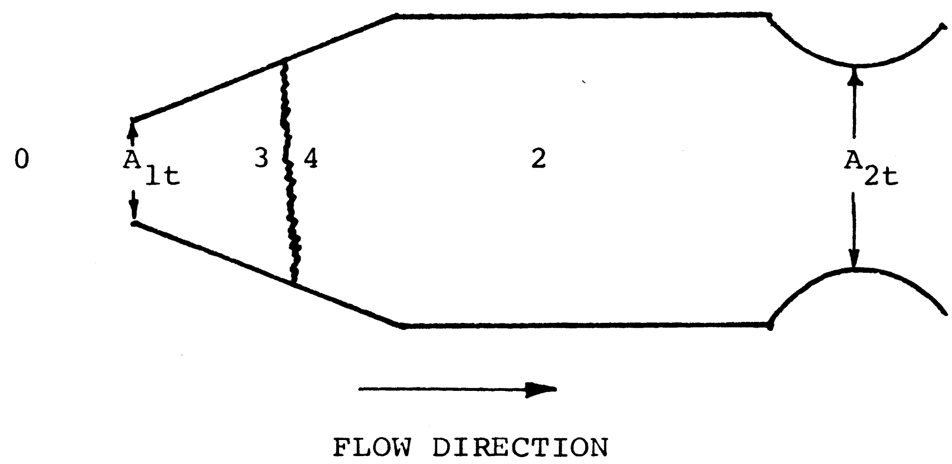

Fig. A-1 The flow regions in the establishment of the prior steady flow.

0 shock tube and nozzle feed tank

3,4 upstream and downstream of the recovery shock

2 test section

A_{1t}, A_{2t} the throat areas upstream and downstream of the test section

Once the recovery shock reaches the parallel channel, only a small drop in the post shock density is required to remove it to the downstream end of the channel. The necessary density reductions will take place at a time which is small compared with the time elapsed since the flow beginning.

The rate of change of mass $(\rho_2 V_2)$ in region 2 in Fig. A.1 can then be written

$$V_2 \frac{d\rho_2}{dt} = \rho_{1t} u_{1t} A_{1t} - \rho_{2t} u_{2t} A_{2t}$$

$$= k(\gamma)\ a_0\ (\rho_0 A_{1t} - \rho_2 A_{2t}) \qquad \text{...(A-1)}$$

$$\text{where } k(\gamma) \equiv \left(\frac{2}{\gamma+1}\right)^{\left(\frac{\gamma+1}{2(\gamma-1)}\right)}$$

where the single subscripts refer to the regions in the diagram in Fig. A.1. and subscripts 1t and 2t refer to the nozzle entrance and test section exit respectively.

Solving equations (A-1) for time as a function of density ρ_2 we have

$$t = -\frac{V_2}{k(\gamma)\ a_0\ A_{2t}} \ln\left(\frac{\dfrac{\rho_2}{\rho_0} - \dfrac{A_{1t}}{A_{2t}}}{1 - \dfrac{A_{1t}}{A_{2t}}}\right) \qquad \text{...(A-2)}$$

At this stage a further assumption is made:
ASSUMPTION 5. The appropriate test section cross-sectional area to consider is that of the inside of the valve actuating sleeve.

The nozzle will produce a flow which is nearly parallel and which is contained within the sleeve. The region of the test section outside the sleeve will therefore play little part in the establishment of the prior steady flow. The density behind the recovery shock, ρ_2 required to produce a supersonic flow at the area ratio of the sleeve is given in parametric form as

INSERT AFTER FIRST SECTION IN APPENDIX A.p.A3.

In a steady, one-dimensional channel flow sonic conditions can only exist at a channel station where there is a local minimum in the cross-sectional area. It is therefore not strictly correct to allow the cross-sectional area at the valve station, A_{2t}, to equal the cross-sectional area of the valve sleeve while retaining the assumption that the flow is sonic and quasi-steady at that station.

One way to circumvent this difficulty is to reduce A_{2t}. From equation (A-2) it can be seen that the prior steady flow establishment time, $t_e \to \infty$ as $A_{2t}/A_{1t} \to (\rho_2/\rho_0)^{-1} = 15.48$ for air and 17.33 for argon when the recovery shock reaches the value sleeve. However, for an air flow, $t_e = 28.7$ msec for $A_{2t}/A_{1t} = 15.5$ and $t_e = 11.9$ msec for $A_{2t}/A_{1t} = 17.5$. Acceptable values of t_e are therefore obtained with a moderate constriction of the channel at the valve under the quasi-steady model as formulated above.

In order to check the results of the simple, quasi-steady model above, two one-dimensional nonsteady Method of Characteristics (MOC) calculations were performed on the problem. The equations used in these calculations are given on page 9 of this thesis. The initial state of the system consisted of the nozzle feed tank, the nozzle and test section filled to the initial shock tube pressure, p_s and the dump tank filled to a pressure of 0.03 or less of p_s. A diaphragm initially at the valve station is removed instantaneously at time $t = 0$.

For both calculations, the cross-sectional area of the channel was that of the valve sleeve between the nozzle exit and the valve, in accordance with assumption (5) of the quasi-steady model. In the first MOC calculation the cross-sectional area remained constant at this value downstream of the valve, while in the second MOC calculation there was an increase in the cross-sectional area downstream of the valve. The rate of increase of the cross-sectional area with distance, x, was small compared with that expected from consideration of the real valve geometry.

Several interesting results arose out of these calculations. Firstly, the time taken for the recovery shock to reach the valve sleeve was 13.3 msec for the first calculation and 9.8 msec for the second calculation. The indication therefore is that a rapid increase in cross-sectional area downstream of the valve would reduce this time still further. The quasi-steady and MOC models therefore seem to be in good agreement as to the time t_e.

Secondly, the time taken for the recovery shock to move from the nozzle exit to the valve was 5 msec for the second calculation. This result qualifies and quantifies assumption (4) of the quasi-steady model.

Thirdly, the flow upstream of the recovery shock in the two MOC calculations closely approaches a steady flow with sonic conditions at the nozzle throat 4.5 msec after the valve opening which is 2.5 msec after the arrival at the nozzle throat of the head of the expansion from the valve opening.

The fourth result is that the flow at the valve is more nearly sonic in the second calculation than the first. A rapid increase in the cross-sectional area downstream of the valve would probably force the flow to be sonic very close to the valve in a nonsteady flow.

The last two results show that the assumption (1) for the quasi-steady flow may be held without the necessity for a minimum in the cross-sectional at the valve station. Further comparisons between the quasi-steady and MOC calculations must be made in relation to assumption (1). The assumption is used to calculate the mass flow rate at the valve in the quasi-steady model. Comparison of the mass flow rates at the valve predicted by the two models shows that the quasi-steady model provides a reasonable approximation to the non-steady mass flow rate. It must be realised, however, that the existence of a particular mass flow rate at a channel station at a particular time has different implications for the two models. In the quasi-steady model information on mass flow rate changes is transmitted instantaneously to the rest of the system. In the MOC model the transmission speed is finite.

In conclusion, the apparent contradiction in the quasi-steady model outlined at the beginning of this amendment can be resolved in two ways. The channel cross-sectional area at the valve can be reduced in the original model and a reasonable value of t_e obtained. Alternatively, the results of the MOC calculation can be used to justify the use of the quasi-steady model with A_{2t} equal to the valve sleeve cross-sectional area.

$$\frac{\rho_2}{\rho_s}\frac{\rho_s}{\rho_0} = \frac{(\gamma+1)M_s^2}{((\gamma-1)M_s^2+2)\left[1+\left(\frac{\gamma-1}{2}\right)M_s^2\right]^{1/(\gamma-1)}} \qquad \text{...(A-3a)}$$

$$\left(\frac{A_s}{A_{1t}}\right)^2 = \frac{1}{M_s^2}\left(\frac{2}{(\gamma+1)}\left(1+\frac{(\gamma-1)}{2}M_s^2\right)\right)^{\left(\frac{\gamma+1}{\gamma-1}\right)} \qquad \text{...(A-3b)}$$

(from Liepmann (1957)).

Where subscript s denotes the supersonic flow in the sleeve ahead of the recovery shock. The ratio $A_s/A_{1t} = 21.8$. From equations (A-3a) and (A-3b) the values of ρ_2/ρ_0 are then 0.065 for air and 0.058 for argon. For recoil distances of greater than 0.9 cm., the limiting ~~corss~~ cross-sectional area downstream of the test section is that of the valve sleeve itself. Therefore $A_{1t}/A_{2t} = (21.8)^{-1}$ and $A_{2t} = 248\ \text{cm}^2$. The values of the other parameters are

$$V_2 = 1.1\text{x}10^4\ \text{cm}^3$$

$$a_o = 3.43\text{x}10^4\ \text{cm/sec for air}$$

$$3.19\text{x}10^4\ \text{cm/sec for argon}$$

$$k(\gamma) = 0.579 \text{ for air}$$

$$0.563 \text{ for argon}$$

These figures produce prior steady flow establishment times of 8.8 msec. for air and 11 msec. for argon. The time for the free piston to travel from the launcher to the main diaphragm is between 50 and 100 msec. The maximum recoil distance is approximately 3.8 cm. The recoil distance is therefore greater than 0.9 cm. for between 25 and 50 msec. assuming constant acceleration of the piston over most of its travel. The calculation therefore shows that the prior steady flow should become entirely supersonic in a time much shorter than that available. It should be noted that the pumping time before the recoil distance reaches 0.9 cm. has not been included in the calculation.

A.2. REDUCTION OF SHOCK TUBE PRESSURE DUE TO PSF.

The reduction of the shock tube pressure due to the presence of the prior steady flow is given by

$$\frac{\Delta p}{p_0} = \frac{\Delta \rho}{\rho_0} = \frac{\rho_{1t} u_{1t} A_{1t}}{\rho_0 V_{st}} t_p = \frac{\left(\frac{2}{\gamma+1}\right)^{\left(\frac{\gamma+1}{2(\gamma-1)}\right)} a_0 A_{1t}}{V_{st}} t_p$$

where t_p equals time for the piston to travel to the main diaphragm and then V_{st} equals the volume of the shock tube and nozzle feed tank. Taking t_p = 100 msec., $V_{st} = 3.02 \times 10^5$ cm^3 we have $\Delta p/p_0 = 0.08$ for air and 0.07 for argon. This represents an acceptable pressure reduction in the shock tube.

APPENDIX B. THE ESTC COMPUTER PROGRAMME.

ESTC has been used extensively for the flow field calculations in this thesis. The details of this programme are given by M.K. McIntosh (1968).

The programme was used here to calculate the equilibrium post primary shock conditions in the shock tube. The programme assumes that the shock and the region of chemical nonequilibrium which follows it to be a mathematical discontinuity. The usual equations for mass momentum and energy conservation in an inviscid flow are then solved by minimising the function

$$f = \left(1 - \frac{LHS_1}{RHS_1}\right)^2 + \left(1 - \frac{LHS_2}{RHS_2}\right)^2$$

where LHS_1 and RHS_1 are the left and right hand sides of the mass conservation equation. LHS_1 and RHS_2 are the right and left hand sides of the momentum conservation equation.

Inputs to the programme are the initial temperature, pressure and composition of the gas and thermodynamic information about the constituents of the gas. A simple harmonic oscillator model is used for the gas molecules up to a temperature of $5000^{\circ}K$. A polynomial fit to more accurate data is used for temperatures above this.

APPENDIX C. THE NFAPC COMPUTER PROGRAMME.

A full description of this programme can be found in J. A. Lordi et al (1966). The programme solves the problem of a steady expansion of gas in a specified nozzle area ratio distribution. The gas flow accepted by the programme is supersonic and in chemical equilibrium. The programme takes a small step along the flow direction, calculates the nozzle area ratio at the new station and then numerically integrates the appropriate set of simultaneous partial differential equations using a modified Runge-Kutta technique. The programme is capable of calculating flows with nonequilibrium, equilibrium and frozen chemistry. All the species including the electrons are assumed to have the same temperature.

ADDITION TO APPENDIX C

The equations used by NFAPC is solving the nozzle flow problem are the following:

$$\rho u A = \text{constant} \qquad \text{continuity (c-1)}$$

$$u\,du + \frac{1}{\rho}\,dp = 0 \qquad \text{momentum conservation (c-2)}$$

$$H + \frac{u^2}{2} = H_o \qquad \text{Energy Conservation (c-3)}$$

$$p = \frac{\rho R_o T}{M} \qquad \text{Thermal Equation of State (c-4)}$$

$$H = \sum_{j=1}^{s} X_j h_j \qquad \text{Caloric Equation of State (c-5)}$$

where M = mean molecular weight (gm/mole)

s = number of species present in mixture

X_j = mole fraction of species j

h_j = specific enthalpy of species j

The other quantities have their usual meanings p, ρ T are normalised to their reservoir values. Enthalpy and u are normalised to $R_o T_o'$ and $(R_o T_o'/M_o)^{\frac{1}{2}}$ where dash(') indicates a dimensional quantity and subscript o indicates the reservoir value. Nozzle cross sectional area A is normalised to the nozzle throat value.

EQUILIBRIUM FLOWS

The equilibrium flow of an inviscid , perfect gas is isentropic. To calculate such a flow NFAPC takes a step (down) in temperature then calculates a new pressure and set of species concentrations by a Newton-Rhapson method at the specified temperature and entropy. The equations to which the iteration scheme is applied are the equations expressing chemical equilibration among the constituents coupled with the equation for the conservation of mass in the species formation reactions. In addition, the constancy of the mixture entropy is included to complete the necessary set of equations.

Once the pressure and species concentrations have been calculated, the local mean molecular weight is calculated from the definition of this quantity. Equation (C-4) is then used to calculate the density. The static enthalpy is calculated from equation (C-5) and the flow velocity from equation (C-3). The value of the Mach number is calculated as

$$M = \frac{u}{[(p-p_s)/(\rho-\rho_s)]^{\frac{1}{2}}} \qquad \text{(C-6)}$$

where subscript s refers to the previous computational step.

FROZEN FLOWS

The calculation of a flow whose species concentrations are frozen at the reservoir values proceeds in the same way as the equilibrium calculation except that because the species concentrations are fixed the pressure can be calculated explicitly at a given temperature and (constant) entropy.

NONEQUILIBRIUM FLOWS

The nonequilibrium flows, like the frozen and equilibrium flows, are governed by equations (C-1) to (C-5). In this case, however, the nonequilibrium rates of species production appear in the species conservation equations.

The set of s+2 linear, simultaneous equations for the unknown slopes $\frac{d\gamma_j}{dx}$ $j = 1, 2, \ldots, s$, $\frac{dT}{dx}$ and $\frac{d\ln\rho}{dx}$ at a point in the numerical integration are

$$\sum_{j=1}^{s} \alpha_{jk} \frac{d\gamma_j}{dx} = 0 \quad k = 1,2,\ldots,c \qquad \text{(C-6)}$$

$$\frac{d\gamma_j}{dx} = \sum_{j=1}^{s} \beta_{ij}\, P_i\, X_i \quad j = c+1, c+2, \ldots, s \qquad \text{(C-7)}$$

$$\sum_{=1}^{s} h_j \frac{d\gamma_j}{dx} + \sum_{j=1}^{s} \gamma_j C_{pj} \frac{dT}{dx} - \frac{u^2}{M_o} \frac{d\ln\rho}{dx} - \frac{u^2}{M_o} \frac{d\ln A}{dx} = 0 \tag{C-8}$$

$$\sum_{=1}^{s} \frac{d\gamma_j}{dx} + \frac{1}{T} \sum_{j=1}^{s} \gamma_j \frac{dT}{dx} + \left(\frac{1}{M} - \frac{u^2}{M_o T}\right) \frac{d\ln\rho}{dx} - \frac{u^2}{M_o T} \frac{d\ln A}{dx} = 0 \tag{C-9}$$

here the species are divided into c independent and (s-c) independent pecies. The dependent species can be formed from the set of independent pecies by linear combination.

α_{jk} = number of independent species k in species j.

γ_j = (moles of species j)/(gm of mixture).

$\sum_{=1}^{r} \beta_{ij} P_i X_i$ = (rate of production of species j by the r chemical reactions)/u'

u' = dimensional flow velocity.

$C_{pj} = \left(\frac{dh_j}{dT}\right)_p$ = specific heat at constant pressure for species j.

umerical integration of the above equations between two nozzle tations yields values for γ_j , j=1, 2, ..., s, ρ and T. The other low variables of interest are obtained from the conservation equations n a manner similar to that used for the frozen and equilibrium flows.

REFERENCES

Bauer E. (1951) "Dissociation of hydrogen molecules by vibrational excitation and three body recombination coefficient" Physical Review (A) 84(2) pp.315-321.

Courant R. and Hilbert D. (1962) "Methods of Mathematical Physics" Vol II (Wiley Interscience, N.Y.)

Davies L. and Lippiatt J. (1964) "Evaluation of a modified 3/8" diameter pressure-bar gauge for shock tube studies" National Physical Laboratory Aero, Note 1029 A.R.C. 26 360 Hyp. 456.

Davies L. and Wilson J.L. (1969) "Influences of reflected shock and boundary layer on shock tube flows" Physics of Fluids 12 p.I-37 to I-43.

Ebrahim N.A. and Hornung H.G. (1975) "High-enthalpy non-equilibrium carbon dioxide nozzle and wedge flows: experiment and calculations" Synoptic, AIAA J 13 pp.845-846.

Fite W.L. and Brackman R.T. (1958a) "Collision of electrons with hydrogen atoms I. Ionisation" Phys. Rev. 112 1141-1151.

Fite W.L. and Brackman R.T. (1958b) "Collision of electrons with hydrogen atoms II Excitation of Lyman-Alpha radiation" Phys. Rev. 112 1151-1156.

Garr L.J. and Marrone P.V. (1963) "Inviscid, nonequilibrium flow behind bow and normal shock waves, Parts I and II" CAL Report No. QM -- 1626 - A 12(I,II).

Garr L.J. and Marrone P.V. Joss W.J. and Williams M.J. (1966) "Inviscid, nonequilibrium flow behind bow and normal shock waves, Part III" CAL Report No. QM-1626-A-12(III).

Gaydon A.G. and Hurle I.R. (1963) "The shock tube in high temperature chemical physics" (Chapman and Hall, London).

Goodyear C.C. and Von Engel A. (1962) "Dissociation and ionisation of hydrogen in high frequency discharges" Proc. Physical Society, London, 79 pp.732-740.

Hertzberg, A., Wittcliff, C.E. and Hall, J.G. (1961) "Development of the shock tunnel and its application to hypersonic flight", "Hypersonic Flow Research", ed. F.R. Riddell, Astronautics and Rocketry, 7, pp. 701-758. Academic Press, N.Y. and London.

Holder, D.W. and Schultz, D.L. (1961) "The duration and properties of the flow in a hypersonic wind tunnel". "Hypersonic Flow Research", ed. F.R. Riddell, Astronautics and Rocketry 7, pp. 513-546 Academic Press, N.Y. and London.

Horn K.P., Wong H. and Bershader D. (1967) "Radiative behaviour of a shock heated argon plasma flow" J. Plasma Physics 1 p157-170.

Hornung H.G. (1972) "Nonequilibrium dissociating nitrogen flows over spheres and circular cylinders" J. Fluid Mech. 53(1) pp.149-176.

Hornung H.G. and Sandeman R.J. (1972) "Interferometric measurements of radiating ionising argon flow over blunt bodies", J? Phys. D: Appl. Phys., 7pp. 940-944.

Jacobs T.A., Geidt R.R. and Cohen N. (1967) "Kinetics of hydrogen halides on shock waves II A new measurement of the hydrogen dissociation rate" J. Chem. Phys. 47(1) pp.54-57.

Kewley D.J. and Hornung H.G. (1974) "Nonequilibrium dissociating nitrogen flow over a wedge" J. Fluid Mech., 64 pp. 725-736.

Lewis C.H. and Burgess E.G. (1964) "Charts of normal shock wave properties in imperfect air" Technical Documentary Report AEDC-TDR-64-43.

Liebowitz L.P. (1973) "Measurements of structure in an ionising shock wave" Phys. Fluids. 16(I) p59-68.

Liepmann H.W. and Roshko A. (1957) "Elements of gasdynamics" John Wiley and Sons.

Logan P.F. (1972) PhD. Thesis, Australian National University Canberra, Australia.

Lordi, J.A. Mates R.E. and Moselle J.R. (1966) "Computer programme for the numerical solution of nonequilibrium expansions of reacting gas mixtures" NASA CR-472 (Clearinghouse No. N66-26856).

McClure, G.W. (1964) "Ionisation and dissociation of fast H_2 molecules incident on hydrogen gas" Phys. Rev. (A) 134 pp.1226-1234.

McIntosh M.K. (1968) "Computer programmes for the numerical calculation of frozen and equilibrium conditions in shock tunnels" Internal Report Dept., Physics S.G.S. Australian National University, Canberra, Australia.

Meier P. (1973) PhD. Thesis, Australian National University, Canberra, Australia.

Mirels H. (1963) "Test time in low pressure shock tubes" Phys. Fluids, 6(9) pp.1201-1214.

Mirels H. (1964) "Shock tube test time limitation due to turbulent wall boundary layer" AIAA J. 2(1) pp.84-93.

Moore C.E. (1959) "A multiplet table of astrophysical interest 1945 edition" U.S. Dept. of Commerce/National Bureau of Standards/Institute for Applied Technology. Clearinghouse No. PB151 395.

Oertel H. (1969) "Non-reflected shock tunnel test times" Proc. of 7th Internationsl Shock Tube Symposium ed. I.I. Glass pp. 80-108.

Oettinger P.E. and Bershader D. (1967) "A unified treatment of the relaxation phenomena in radiating argon plasma flows" AIAA J. 5(9) 1625-1632.

Patch R.W. (1962) "Shock tube measurement of dissociation rates of hydrogen" J. Chem. Phys. 36(7) pp.1919-1924.

Rudinger G. (1955) "Wave diagrams for nonsteady flow in ducts" Van Nostrand.

Sedney R. (1970) "The method of characteristics" in "Gas-dynamics Vol. 1." _ "Nonequilibrium flows" Part II ed. P. Wegener. Marcel Decker Inc. N.Y.

Shapiro A.H. (1953) "The dynamics and thermodynamics of compressible fluid flow" Vol. I and ~~00~~ II. The Ronald Press Co. N.Y.

Stalker R.J. (1966) "The free piston shock tube" Aeronaut. Quart. 17 pp.351-370.

Stalker R.J. (1967) "A study of the free piston shock tunnel" AIAA J. 5(12) pp. 2160-2165.

Stalker R.J. and Hornung H.G. (1969) "Two developments with free piston drivers" Proc. of 7th International Shock Tube Symposium ed. I.I. Glass. pp.242-256.

Stalker R.J. and Mudford N.R. (1973) "Starting process in the nozzle of a non-reflected shock tunnel" Synoptic AIAA J. 11(3) pp. 265-266.

Stalker R.J. and Stollery J.L. (1975) "The use of a Stalker-tube for studying high enthalpy, nonequilibrium air-flow over delta wings" Modern Developments in Shock Tube Research Proc. 10th International Shock Tube Symposium, Kyoto, 1975. ed. G. Kamimoto. Distributed by the Shock Tube Research Society, Japan, pp.55-66.

Stalker R.J. (1976) Private communication.

Stier P.M. and Barnett C.F. (1956) "Charge exchange cross-sections of hydrogen ions in gases" Phys. Rev. (A) 103 pp.896-907.

Smith C.E. (1966) "The starting process in a hypersonic nozzle" J. Fluid Mech. 24 pp. 625-630.

Tate J.T. and Smith P.T. (1932) "The efficiencies of ionisation and ionisation potentials of various gases under electron impact" Phys. Rev. 39 270-277.

Wong H. and Bershader D. (1966) "Thermal ~~equilibtion~~ equilibration behind an ionising shock" J. Fluid Mech. 26(3) pp.459-479.

LIST OF FIGURES.

CHAPTER 1.

CHAPTER 2.

CHAPTER 3.